Chair of Materials Physics

Doctoral Thesis

Electro-Mechanical Behavior of Flexible Thin Film Systems

Dipl.-Ing. Patrice Kreiml

June 2020

MONTANUNIVERSITÄT LEOBEN
www.unileoben.ac.at

EIDESSTATTLICHE ERKLÄRUNG

Ich erkläre an Eides statt, dass ich diese Arbeit selbständig verfasst, andere als die angegebenen Quellen und Hilfsmittel nicht benutzt, und mich auch sonst keiner unerlaubten Hilfsmittel bedient habe.

Ich erkläre, dass ich die Richtlinien des Senats der Montanuniversität Leoben zu "Gute wissenschaftliche Praxis" gelesen, verstanden und befolgt habe.

Weiters erkläre ich, dass die elektronische und gedruckte Version der eingereichten wissenschaftlichen Abschlussarbeit formal und inhaltlich identisch sind.

Datum 09.06.2020

Unterschrift Verfasser/in
Patrice, Kreiml

This thesis was supported by the Austrian Research Promotion Agency (FFG, Project No. 857043) and done in cooperation with Plansee SE at the Department of Materials Science at the University of Leoben, Austria.

In der Ruhe liegt die Kraft." *unbekannt*

"If we tried to think of a good idea, we wouldn't have been able to think of a good idea. You just have to find the solution for a problem in your own life."
Brian Chesky, Co-founder of Airbnb

DANKSAGUNG

In den letzten dreieinhalb Jahren bin ich zahlreichen Menschen begegnet, die mir direkt oder indirekt beim Sammeln meiner Daten und der Erstellung meiner Publikationen geholfen haben. An dieser Stelle möchte ich mich bei euch allen bedanken!

Vor allem möchte ich mich bei meiner Betreuerin **Priv. Doz. Dr. Megan J. Cordill**, die mir die Chance für diese Arbeit gegeben hat, bedanken. Sie hat mir die Möglichkeit gegeben Neues auszuprobieren und zu erleben, sowie neue Leute kennenzulernen. Ihre unkomplizierte und direkte Herangehensweise war mir immer eine Hilfe bei der Lösung von Problemen. Vielen Dank für eine stets offene Tür und die entgegengebrachte Geduld und Zeit.

Bei **Prof. Dr. Christian Mitterer** möchte ich mich ebenso für die Ermöglichung dieser Arbeit bedanken. Ich möchte mich für die zahlreichen Diskussion und Einblicke, sowie das regelmäßige Feedback zu meiner Arbeit in den Projektmeetings bedanken. Seine Perspektive hat es mir erlaubt meine Arbeiten immer ein Stück weiter zu verbessern und ich konnte viel dabei lernen. Vielen Dank!

Bei **Dr. Judith Köstenbauer**, **Dr. Harald Köstenbauer** und **Dr. Jörg Winkler** von Plansee SE möchte ich mich für die Zusammenarbeit im gemeinsamen Projekt bedanken. Die Diskussionen bei den Projektmeetings, sowie die Einblicke aus der Perspektive der Industrie haben mir sehr geholfen meinen eigenen Horizont zu erweitern. Dafür Danke!

An dieser Stelle möchte ich mich bei allen Kolleginnen und Kollegen am ESI für die tolle Zeit bedanken. Besonderer Dank gilt aus der eigenen Arbeitsgruppe **Dr. Oleksandr Glushko**, **Dr. Barbara Putz**, **Dr. Andreas Kleinbichler**, die mich vor allem in meiner Anfangszeit am ESI mit Rat und Tat unterstützten. Ebenso gilt mein Dank **Dipl.-Ing. Claus Trost** vor allem für die Hilfe, wenn es um das Programmieren geht und **Dr. Alice Lassnig** für Diskussion und Austausch. **Volker Matl**, **Katharina Ruderes** und **Hemma Sandner** danke ich für die experimentelle Unterstützung. Damit haben sie mir viel Zeit erspart, die es mir ermöglicht hat mich auf andere Dinge zu konzentrieren.

Bei meinen Bürokollegen **Dr. Benjamin Schuh**, **Dr. Oliver Renk** und **Dipl.-Ing. Sabine Bodner** bedanke ich mich für die gute Atmosphäre am Arbeitsplatz und ihre Hilfsbereitschaft.
Bei **Dipl.-Ing. Stefan Hartl**, **Dr. Stanislav Zak**, **Dr. Juraj Todt**, **Dipl.-Ing. Markus Alfreider**, **Dr. Bernhard Völker**, **Dr. Anton Hohenwarter**, **Assoc. Prof. Dr. Daniel Kiener** und **Dr. Stefan Wurster** bedanke ich mich für ihre Expertise zu den Themen Widerstandsmessung, Simulation, Röntgendiffraktion, REM und FIB.

Daniela Brunner und **Sabine Wilfling** danke ich für administrative Hilfe, vor allem bei den Reiseabrechnungen. **Franz Hubner**, **Robin Neubauer**, **Thomas Mohr**, **Gerald Reiter**, **Silke Modritsch**, **Dipl.-Ing. Caroline Freitag**, **Ing. Herwig Felber** und **Gabriele Felber** danke ich für die technische Hilfe im Laufe der letzten dreieinhalb Jahre.

Ich bedanke mich bei den Kollegen vom Lehrstuhl für Funktionale Werkstoffe und Werkstoffsysteme für den regen Austausch und Diskussionen. Besonderen Dank ergeht an **Dr. Martin Rausch**, der mir im Zuge des gemeinsamen Projekts viel neues Wissen über Beschichtungstechnik vermittelt hat. Bei **Sabrina Hirn**, **Ing. Karl-Heinz Pichler** und **Dipl.-Ing. Velislava Terziyska** bedanke ich mich für ihre unermüdliche Arbeit und die zahlreichen Proben, die ich ihnen zu verdanken habe. Bei meinem guten Freund **Dipl.-Ing. Ao Xia** möchte ich mich für zahlreiche Diskussionen bedanken, sowie dafür, dass er der Anstoß für meine Entscheidung zu einer Dissertation war.

Ich möchte mich auch bei allen meinen Freunden bedanken, die die letzten dreieinhalb Jahre noch heiterer gestaltet haben. Meinem guten Freund **Anatol Drlicek** vom MCL, danke ich, dass er mir in seiner Freizeit das Plotten mit Python gezeigt hat. Danke!

Ich danke auch meiner Familie, allen voran meinen Eltern **Leopold Kreiml** und **Asuncion Kreiml** für ihre Liebe, Geduld und Unterstützung in allen Lebenslagen.

Zu guter Letzt bedanke ich mich auch für alle die Hilfe im verborgenen, die ich nicht bewusst wahrgenommen habe. Vielen Dank!

KURZFASSUNG

In den letzten Jahren wurde umfangreich an flexiblen elektrischen Geräten, seitens der Industrie and an Hochschulen, geforscht. Flexible Elektronik könnte zu potentiellen Fortschritten in den Bereichen Medizin und Logistik, aber auch im Sport, der Unterhaltung und im alltäglichen Leben führen. Unter den zahlreichen Problemen, die für die Umsetzung von zuverlässigen flexiblen elektrischen Geräten gelöst werden müssen, sind eines davon die Elektroden für Daten- und Energietransfer. Für flexible Anwendungen müssen diese die individuellen Komponenten verbinden und unter sich verändernden Beanspruchungen die Funktion erhalten (Biegen, Ziehen, Drehen).

Diese Arbeit fokussiert sich auf Mo/Al/Mo Multischichtelektroden, die üblicherweise in TFT Bildschirmen zum Einsatz kommen. Der Mo-Film agiert als Adhäsionsschicht und Diffusionsbarriere, während der Al-Film die Funktion der Elektronenleitung übernimmt. Für elektromechanische Tests wurden vereinfachte Al/Mo Doppelschichten auf Polymere abgeschieden. Die Al/Mo Doppelschichten wurden unter uniaxialem Zug und unter zyklischer Biegung getestet. Die Doppelschichten bestehen aus einer 30 nm dicken Mo Adhäsionsschicht mit verschieden dicken Al Schichten (30, 75, 150, 300 nm) darauf. Die Zugtests zeigten, dass die inhärent spröde Mo Schicht den Bruch der Doppelschicht verursacht, was auch zum Verlust der Leitfähigkeit führt. Jedoch wurde auch gezeigt, dass dickere Al-Schichten Bruchvorgänge mindern und verzögern können. Die Biegetests lieferten ein ähnliches Verhalten. Jedoch haben für zyklische Biegetests die angewandte Biegedehnung und Anzahl der Biegezyklen einen starken Einfluss auf das Ergebnis. Bei 20.000 Biegezyklen und 0,5% Biegedehnung zeigen die Al/Mo Doppelschichten keinen Bruch und kaum Änderung in der elektrischen Leitfähigkeit. Bei derselben Zyklenzahl, aber unter 1,3% und 3,1% Biegedehnung, brechen die Doppelschichten beim Erreichen der ersten Zyklen und erreichen Risssättigung bei ca. 10.000 Zyklen. Die Rissdichtensättigung und der Verlust der Leitfähigkeit sind proportional der Biegedehnung. Bei 1,3% und 3,1% Biegedehnung versagen die Al/Mo Doppelschichten bevor sie 1.000 Zyklen erreichen.

Um das spröde Verhalten des Mo-Films ohne starken Einfluss auf die industrielle Produktionskette und die Funktion des Mo-Films in den Multischichtelektroden zu verbessern, wurden binäre Mo-Legierungen untersucht. Mo-Ta Legierungen stellten sich als beste Kombination aus mechanischer Bruchdehnung (⌣1% Steigerung) und spezifischen elektrischen Filmwiderstand (höher, aber nahe an Mo) heraus. Die Mo-

Filme in den Doppelschichten wurden durch Mo-Legierungen mit 50 at.% Ta, die unter hohen Druckspannungen (-1,9 GPa) stehen, substituiert. Die neuen Al/Mo-Ta Doppelschichten zeigten eine etwa 1% höhere Bruchdehnung unter Zugbeanspruchung. Bei 1,3% Biegedehnung wiesen die Al/Mo-Ta Doppelschichten keine Risse bis zum Ende des Experiments bei 50.000 Biegezyklen auf. Lediglich der elektrische Widerstand stieg vermutlich aufgrund von Ermüdung um 25% bis zum Ende des Experiments. Bei 3,1% Biegedehnung versagen die Al/Mo-Ta Doppelschichten auf ähnliche Weise wie die Al/Mo Doppelschichten.

Die Studie hat gezeigt, dass das Legieren des spröden Mo-Films die Belastbarkeit und Verlässlichkeit der gesamten Multischichtelektrode verbessert hat, was diese geeigneter für flexible Anwendungen wie rollbare Fernsehbildschirme and faltbare Smartphones macht.

ABSTRACT

In recent years, flexible electrical devices are an extensively studied subject in industry and academia. Flexible electronics may potentially lead to advances in different areas, such as medicine and logistics, but also in sports, entertainment and everyday life. Among the many issues that need to be resolved for a reliable flexible electrical device, one of them are the electrodes for data and energy transfer. For flexible applications, they have to connect the individual components and maintain their function under changing load conditions (bending, stretching and twisting).

This work focuses on Mo/Al/Mo multilayer stack electrodes, commonly used in thin film transistor displays. The Mo film acts as an adhesion layer and diffusion barrier, while the Al film's function is charge carrying. For electro-mechanical testing simplified Al/Mo bilayers were deposited on polymer substrates. The Al/Mo bilayers were tested under uniaxial tensile loading (stretching) and under cyclic bending. The bilayers had a 30 nm thick Mo adhesion layer with varying thicknesses of Al (30, 75, 150, 300 nm) on top. The tensile tests showed that the inherently brittle Mo layer causes the bilayer to fracture, including the loss of conductivity, but that increasing thicknesses of the Al layers are able to alleviate and delay the fracture process. The bending tests yielded a similar behavior. However, for cyclic bending the applied bending strain and the number of bending cycles have a strong impact on the result. At 20,000 bending cycles and 0.5% applied bending strain the Al/Mo bilayers showed no fracture and almost no change in conductivity. At the same cycle number, but at 1.3% and 3.1% bending strains, the bilayers start to fracture within the first few cycles and reach crack saturation around 10,000 cycles. The saturation crack density and the loss of conductivity are proportional to the applied bending strain. At 1.3% and 3.1% bending strains the Al/Mo bilayers fail before reaching 1,000 bending cycles.

To improve the brittle nature of the Mo film without severe impact on industrial process chains and the function of the Mo film in the multilayer stack, alloying with another element was investigated. Mo-Ta alloys emerged as the best combination of mechanical failure strain (∽1% increase) and sheet resistivity (higher, but similar to Mo). The Mo films in the bilayers were substituted by Mo alloys with 50 at.% Ta under high compressive stresses (-1.9 GPa). The new Al/Mo-Ta bilayers showed a roughly 1% higher failure strain under tensile load (stretching). At 1.3% bending strain the Al/Mo-Ta bilayers had no cracks when the experiment ended at 50,000 bending cycles. Only, the

electrical resistance increased by 25%, probably due to fatigue, when the experiment ended. At 3.1% bending strain the Al/Mo-Ta bilayers fail, similar to the Al/Mo bilayers.

The study has proven that alloying of the brittle Mo film improves the robustness and reliability of the whole electrode stack and makes the electrode more suitable for flexible applications, such as rollable TVs and foldable smartphones.

TABLE OF CONTENTS

1 INTRODUCTION

In recent years, developments in industry and university research aim towards flexible electronic devices [1–4]. This will enable many new applications to emerge [5], such as wearable health monitoring in medicine [6–8], smart radio-frequency identification tags in logistics [9], and easy to integrate solar cells and displays [10,11] in any possible field (Fig. 1.1). At the current time, early 2020, many well-known smartphone and laptop manufacturers introduced concepts of foldable devices and demonstrate the strong driving forces behind the recent developments.

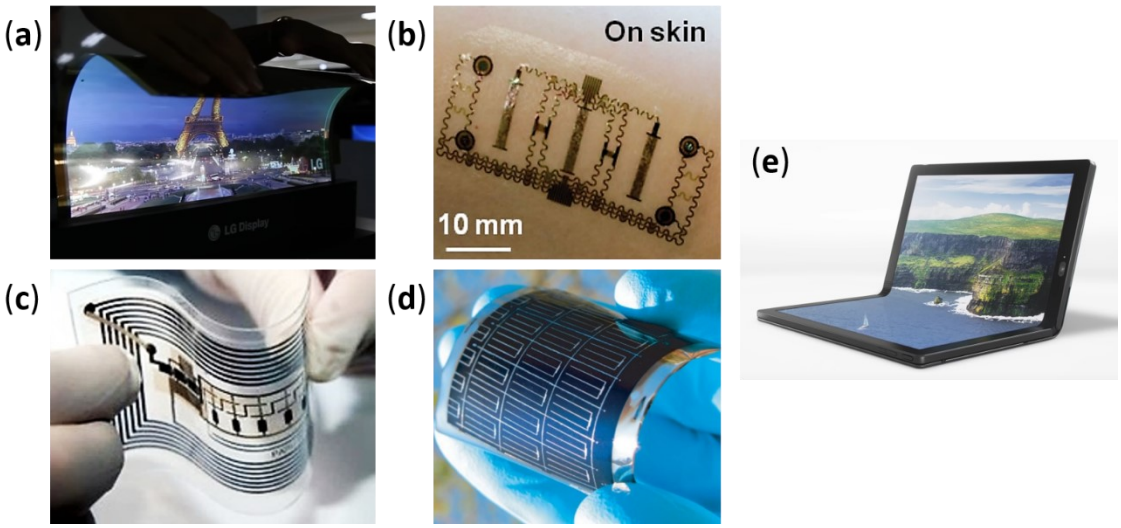

Fig. 1.1 Examples of flexible electronics: (a) a flexible display [12], (b) a sensor-actuator system for prostheses [8], (c) a flexible radio-frequency identification tag [13], (d) a flexible solar cell [10], and (e) a foldable laptop [14].

1.1 AIM OF THIS THESIS

The aim of this thesis is to investigate a commonly used material system for thin film transistor (TFT) display electrodes, Mo/Al/Mo layers, determine their aptitude for flexible applications [15–17] and develop new improved material systems. Therefore, simplified magnetron sputter deposited Al/Mo bilayers were synthesized and tested under monotonic uniaxial tensile loads in Chapter 4 and at different cyclic bending loads in Chapters 5 and 6. Furthermore, in Chapter 7 a screening process for potential adhesion layers to substitute the inherently brittle Mo layers was carried out. Finally, in Chapter 8 the results of the screening process from Chapter 7 were used to create an

improved bilayer system for flexible TFT display electrodes, which have been tested under monotonic uniaxial tensile and intermittent cyclic bending loads.

1.2 FLEXIBLE DISPLAYS

Flexible displays are TFT based light emitting diode architectures that use instead of a rigid substrate, such as glass, polymer substrates, which makes the device foldable and rollable [18]. These new concepts of flexible displays aim to optimize the utilized display area of portable devices, such as phones, tablets and laptops. Hence, it has become more challenging to maintain simultaneously the device's flexibility and functionality [19]. The classical TFT architecture in a display consists of rigid materials, such as silicon, silicon oxide and Mo-based electrodes [20–22]. Attempts for flexible organic TFT systems have shown good results [23]. However, high resolution displays require high conductivity for their electrodes to avoid noise and signal delay, which thin metallic interconnects can ensure better than organic materials [24–26]. The main challenge towards flexible displays is to make them survive repeated folding or rolling without failing. Therefore, numerous improvements were researched and proposed, most of them are improvements of design and device architecture, which are elucidated in the next section.

1.3 TFT DESIGN STRATEGIES

In order to create reliable foldable devices, changing and optimizing the TFT architecture is a relatively easy measure that does not heavily impact the processing chains. Moving the sensitive elements of a display close to the neutral plane, where the applied strains from folding are the smallest, exposes them to less strain and improves the robustness of the device against bending strains [27,28]. This can be achieved by attaching additional protective layers at both sides of the TFT structure, see Fig. 1.2a. Other research groups even established multiple neutral planes by means of soft adhesion layers, as sketched in Fig. 1.2b, allowing to move even more functional elements to the neutral planes and decrease the applied strain in the individual layers [29,30]. The soft adhesion layers are compliant under folding and shear, while the individual layers can deform on their own and have their own neutral planes. Not only the position of the TFTs is of importance, also their orientation with respect to the bending direction [31] as displayed in Fig. 1.2c. Studies on the topic showed that repeated bending cycles of TFT structures yield different behaviors, depending on the bending direction. When the

bending axis is perpendicular to the current flow (case I), the TFTs maintain their function for a certain number of cycles before they fail, but with the bending axis parallel to the current flow (case II), the gate voltage starts to shift at very early cycle numbers and the TFTs lose their functionality much earlier than in the previous case [27,31].

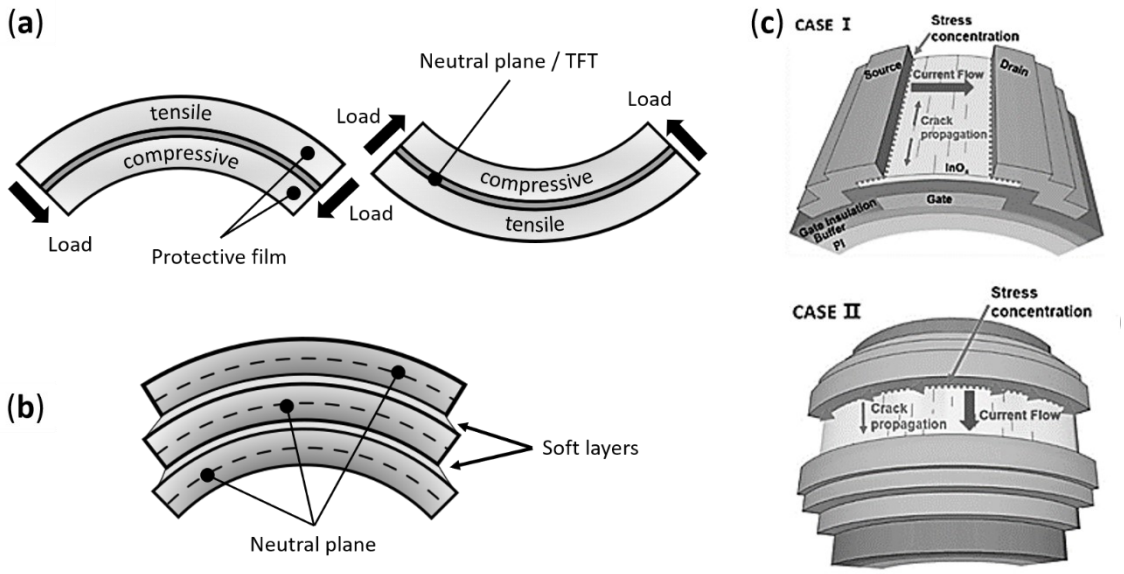

Fig. 1.2 Design strategies for flexible TFT architectures: (a) addition of protective films to move the TFTs to the neutral plane (adapted from [28]), (b) splitting of the neutral plane into multiple neutral planes with the effect of less overall stress (adapted from [29]), and (c) orientation of the TFT to optimize functionality under bending loads (from [31]).

1.4 ELECTRODES

Apart from the general design of the TFT architecture in displays, the electrodes and interconnects between individual electrical elements play an important role for the flexibility of TFT architectures. They have to maintain high conductivity during bending events without breaking. As previously mentioned, the required conductivities, especially for high resolution displays, can only be ensured by thin metal films [24–26]. Mo/Al/Mo multilayers are commonly used electrodes due to their electrical and economical properties [21,22,32]. The multilayer stacks have a good conductivity in the range of a few μΩcm, are easy to process, and the raw materials are commercially widely available [32]. The Al layer has very good conductivity and the Mo layer acts as an adhesion layer as well as a diffusion barrier to the TFT. Good electrical conductor materials such as Al and Cu may form silicides, which is accompanied with volume expansions. When in contact with the Si semiconductor of the TFTs, the formation of Cu and Al silicides may disrupt the connection to the TFTs [33–35]. Therefore, diffusion

barrier layers, which are often brittle in nature are necessary [36]. In order to improve their robustness, several measures have been proposed, (i) splitting the electrodes into multiple smaller, but more robust, islands [37,38] as shown in Fig. 1.3a, (ii) as illustrated in Fig. 1.3b, utilize electrodes in compliant forms [39–41], (iii) tune the microstructure and film stresses of the electrodes [42,43], and (iv) substitute the brittle Mo layer with better suited material systems [44,45].

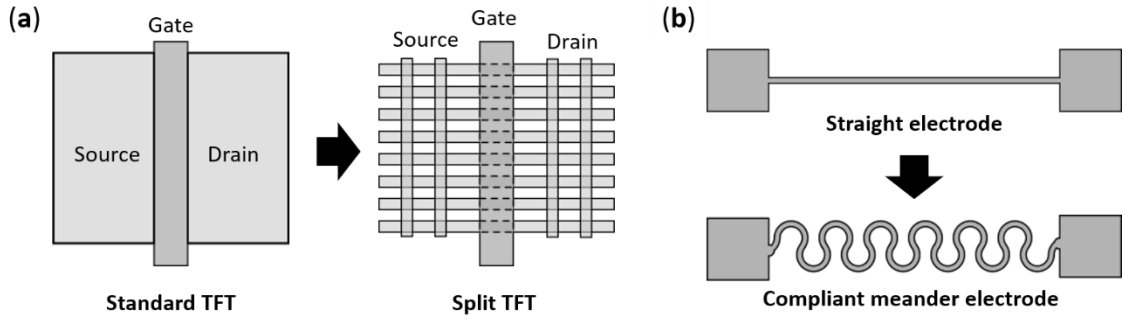

Fig. 1.3 Representative design strategies for electrodes: (a) changing a standard TFT into a split TFT with multiple active islands that have more robustness (adapted from [38]). (b) utilization of compliant electrodes (adapted from [41]).

2 THIN FILM SYNTHESIS

Thin film synthesis has a long history, starting with decorative coatings thousands of years ago. 5000 years ago in Egypt, free standing gold films below 1 µm thickness were produced by beating and bonded with copper/mercury amalgam [46]. In the 1600s and 1700s, the number of techniques and the range of materials for thin film synthesis increased due to the establishment of vacuum pumps and electrical power [47]. Apart from the established electrochemical methods for thin film synthesis, also chemical vapor deposition (CVD) and physical vapor deposition (PVD) techniques arose. Sputtering, a PVD technique, is known since the early 1800s and was further developed over time. In 1921 the yield of direct current (dc) diode sputter deposition was improved in combination with magnetic fields until it reached today's forms [47]. Nowadays, thin films are additionally used for protective and functional coatings due to their low weight and outstanding mechanical properties compared to bulk materials.

PVD techniques in general convert the material to be deposited into vapor, transport it to the substrate and condense matter at the substrate, which is followed by nucleation and film growth. In PVD techniques the chemistry does not change from target to film. PVD can be differentiated by the method used to generate vapor, such as evaporation and sputtering [48,49]. In contrast, CVD techniques deposit a solid from a vapor by means of a chemical reaction on or near a normally heated substrate surface [50].

2.1 MAGNETRON SPUTTER DEPOSITION

Magnetron sputter deposition (MSD) is a PVD technique, commonly used for thin film growth in electronics, for hard coatings in tool manufacturing and for decorative coatings [47,50–52]. In sputtering, incidence particles, which are usually ions (e.g. Ar^+), collide with the source material (target) where an exchange of momentum takes place. The incidence particles cause collision cascades near the target surfaces and ejects sputtered atoms [53], which are transported to the substrate by their momentum and grow a film on the substrate surface [54]. The strengths of sputtered films are their high thin film quality and their ability of depositing under conditions far from thermodynamic equilibrium.

A dc MSD system (Fig. 2.1), consists of a grounded vacuum chamber (anode), a magnetron, a target (cathode) and a substrate holder , which can be grounded, floating,

or biased [55,56]. In the evacuated vacuum chamber ($\leq 10^{-3}$ Pa) a negative potential of several hundred Volts and currents of 0.1 to tens of Amperes is applied between target and chamber. This leads to a glow discharge of the working gas, typically Ar [48,53] (0.1 to 10 Pa in a dynamic equilibrium), and provides Ar^+ ions and electrons, which forms a quasi-neutral plasma. Ar is most commonly used as background gas due to its high natural abundance and its suitable atomic mass for collision processes with target atoms of different atomic masses [48,53]. The degree of ionization is usually smaller than 1% [49]. The Ar^+ ions accelerate through the sheath region between plasma and the negative biased target (Fig. 2.1), which is commonly referred to as dark space [48–50,54]. In the dark space, the Ar^+ ions are exposed to a negative potential of several hundreds of Volts, which translates to tens or hundreds eV of kinetic energy and is capable of breaking the atomic bonds on the target material and initiates collision cascades in the target. These collision cascades lead subsequently to sputtered atoms and the removal of surface atoms [48,50].

The deposition yield is enhanced by the magnetron (Fig. 2.1), an arrangement of inner and outer permanent magnets behind the target [48,49,54]. The magnetron creates a magnetic field ($\vec{B}$), which in combination with the electrical field ($\vec{E}$) forms the Lorentz force ($\vec{B} \times \vec{E}$) [54]. The Lorentz force confines the electrons into a circular or elliptical drift, creating more Ar^+ ions through more frequent collisions of electrons and Ar gas (Fig. 2.1), and increasing the deposition rate. However, while the restricted plasma decreases the substrate temperature and increases deposition rate [51,54], it also leads to the formation of erosion grooves (Fig. 2.1), often called a race tracks [54,57], which limit the utilization of the target material and the target lifetime, due to the simultaneous receding of the target material and the approach of the stationary magnets [49]. Consequentially, the change of the target's surface morphology and roughness during MSD leads to larger angle distribution of the sputtered atoms and to slight changes of the deposited film structure and properties [58].

Targets and magnetrons are available in different geometries. The respective planar targets can be rectangular, squared or round. Due to the unequal erosion of the target only 10 to 50% of the target material is utilized at the end of their lifetime [48,49]. Newer developments are rotatable cylindrical targets, which can utilize up to 90% of the target material at the end of its lifetime due to a nearly even erosion over the profile length [59]. These targets are more frequently used for large-scale industrial deposition chambers [49,60]. Furthermore, water cooling is more efficient in rotatable cylindrical targets, which reduces temperature gradients and improve control over the deposition conditions [56].

MSD differentiates between balanced and unbalanced magnetrons. In the case of the balanced magnetron layout, the inner and outer magnetic poles in the magnetron are equally balanced, concentrating the plasma close to the target region, trapping the electrons in the plasma and limiting the ion current drawn to the substrate. Unbalanced magnetrons are divided into type-1, where the inner magnetic pole is strengthened compared to the outer magnetic pole and opposite type-2 unbalanced magnetrons. Unbalanced type-2 magnetrons, as sketched in Fig. 2.1, have stronger outer magnets, therefore allowing stray magnetic field lines to extend to the substrate, leading to a less confined plasma. The unbalanced type-2 magnetron enables more charged particles and a higher particle flux to reach the substrate, leading to improved microstructures of the growing films [55,61].

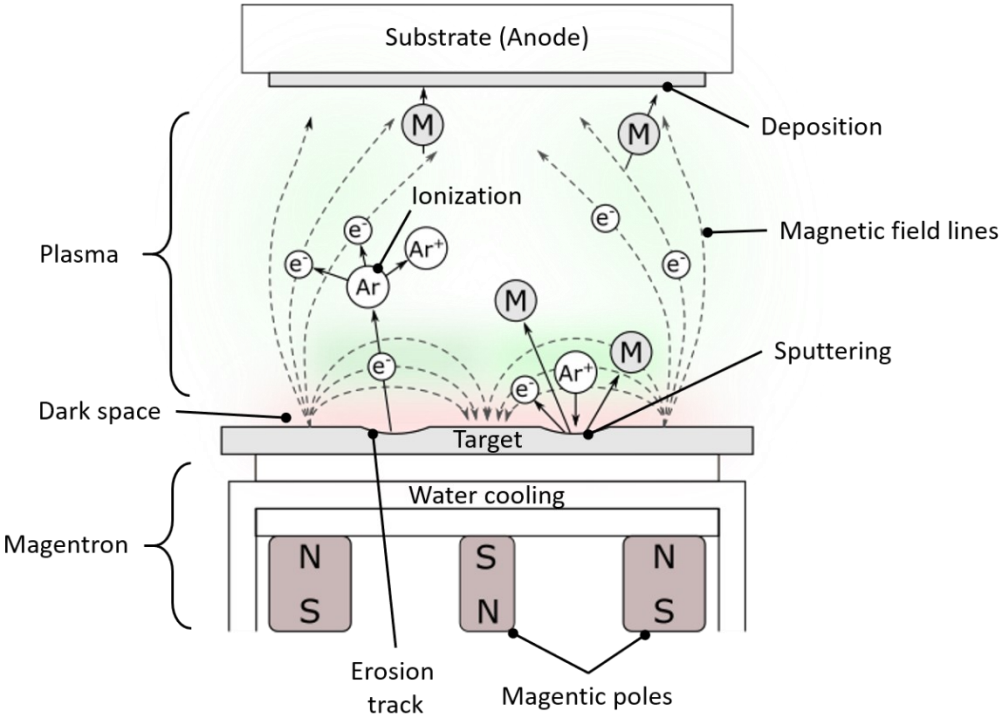

Fig. 2.1 Schematic illustration of an unbalanced type-2 magnetron sputter system, including ionization and sputtering events (modified from [55]).

However, the efficiency of the sputtering process is called sputter yield and is the number of sputtered atoms per incident particle, which is depended on the involved working gas, target elements, discharge power, and Ar gas pressure [48,54]. Different target elements have depending on their mass and bond energy different sputter yield. Furthermore, during transport through the gas phase, the chance of a sputtered particle to collide with a gas particle depends on the gas pressure [62]. Considering a plasma ionization of less than 1% [49], the number of sputtered particles is very small compared

to the amount of working gas atoms. Thus, the occurrence of collisions between sputtered particles during transport can be neglected [63]. Collisions of sputtered particles with the working gas impact the sputter yield, the range of the angular distribution of the sputtered particles, the energy of the sputtered particles that reach the substrate, and subsequently the film properties [62,64,65].

2.2 FILM GROWTH

The properties and structure of magnetron sputter deposited thin films are controlled by the deposition parameters and growing conditions, which are usually in a non-equilibrium state. Both thermodynamic and kinetic aspects have to be considered during film growth [49,66]. A profound understanding of the physical principles behind film growth is necessary to understand the structural evolution of thin films [49,67–69].

2.2.1 CONDENSATION AND NUCLEATION

The energy of the atoms arriving after the transport through the gas phase are in a range of 5 to 50 eV [54]. On the substrate surface the arriving atoms may either condense as loosely adsorbed adatoms, will be reflected, or will be re-sputtered by other arriving particles [70] (Fig. 2.2a). The ratio of the atoms staying on the surface versus the atoms leaving the surface is called sticking coefficient [48,71]. Once an atom arrives on the substrate surface, it will form weak van der Waals bonds. The adsorbed adatoms use surface diffusion to find energetically favorable sites to form stronger bonds [50,66]. Energetically favorable trap sites for single adatoms are steps, clusters of adatoms, and defects on the substrate, such as scratches, grain boundaries, voids in the lattice, impurities and boundaries of different crystallographic orientations [72].

The mobility of the adatoms on the surface plays an important role for the structure of the growing film and depends on the kinetic energy of the adatoms, the substrate temperature, and the species of the adatoms and the substrate [48]. Adatoms in close proximity form small clusters. These initial clusters are very small and not yet stable. Depending on the energetic conditions they are in a dynamic equilibrium of gaining and losing adatoms and can also combine with other clusters [50,66]. Once a cluster reaches a critical size, it becomes a stable island and a low energy site for further adatoms, which enables film growth [50,66] (Fig. 2.2a).

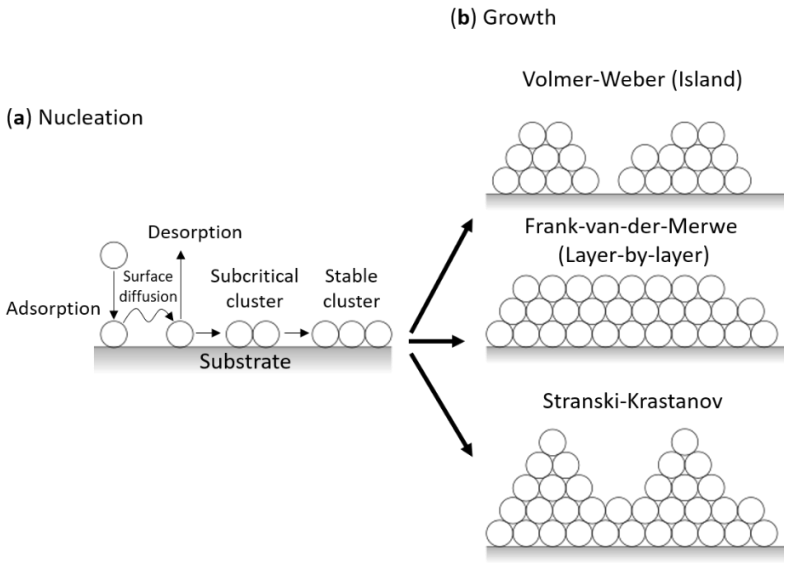

Fig. 2.2 Scheme of (a) nucleation processes and (b) different types of film growth (based on [50,54]).

2.2.2 TYPES OF FILM GROWTH

Dependent of the species of the substrate and adatoms different growth modes can occur [52,73]. These growth modes are depicted in Fig. 2.2b and are called (i) Volmer-Weber [74], (ii) Frank-van-der-Merwe [75–77], and (iii) Stranski-Krastanov [78]. Different species of adatoms can either show more attraction to the substrate or to the adatoms themselves. In Volmer-Weber mode, the attraction of adatoms to each other is larger than to the substrate. This is very often the case when substrate and adatom species are different. In this instance, three-dimensional island growth is initiated and forms polycrystalline films with columnar structure. In Frank-van-der-Merwe mode, adatoms are more strongly attracted to the substrate than to each other. Here, two-dimensional layer-by-layer growth occurs. This type of growth is prominent in the single crystalline epitaxial growth of semiconductor films [54]. The Stranski-Krastanov mode is a mixed mode and combines initial layer-by-layer growth for one or a few monolayers until it becomes energetically more favorable for island growth. This mode occurs more frequently in metal-metal and metal-semiconductor systems, where lattice mismatches at the interfaces cause the films to accumulate stress and strain with increasing film thickness. The resulting stresses can be relaxed in the Stranski-Krastanov growth mode.

2.2.3 STRUCTURE ZONE MODELS

The structural evolution and morphology of growing films are defined at an atomic level and are strongly related to the deposition conditions [79,80]. The first structure zone model (SZM) to relate film structure and deposition conditions, such as the homologous

temperature, $T_H = T_S/T_M$ (substrate temperature and melting temperature of film in Kelvin), was proposed by Movchan and Demchishin [68] for evaporated films. Later Thornton [69,81] adapted the SZM to magnetron sputter deposited thick films (several 10 to 100 µm) and related the film structures additionally to the working gas pressure, which affects the kinetic energy of the bombarding particles. Barna and Adamik [82,83] further introduced the effects of impurities and compared the grown structures at different film thicknesses and their relation to grain size. In general, impurities cannot be entirely avoided during MSD. Even at low impurity content, they segregate at grain boundaries and cause smaller grains and less textured films. At high impurity content, structures are composed of randomly oriented globular grains [82]. The general relation of the film structure and film thickness, starting from nucleation sites [80,83], is illustrated in Fig. 2.3. A description of the individual zones will be introduced in the next paragraphs.

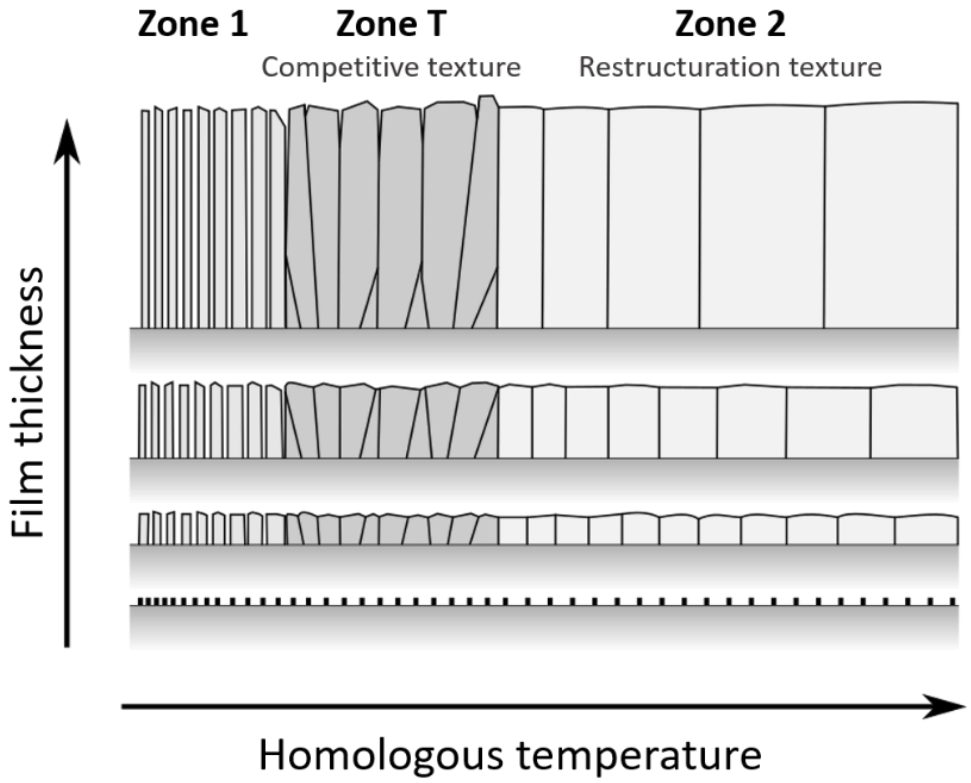

Fig. 2.3 Basic SZM for various film thicknesses (adapted from [80,83]).

Anders [67] modified the three axes of the 3 dimensional SZM to make it more applicable in general terms (Fig. 2.4). The generalized temperature, *T**, includes the homologous temperature and a temperature shift caused by the potential energy of particles reaching the surface. The logarithmic generalized energy, *E**, which previously has only been the effect of the working gas pressure, encompasses now the effects on the

substrate caused by the kinetic energy of the arriving particles. The vertical z-axis, *t**, represents the qualitative film thickness, which induces an indication of thickness reduction caused by densification and (re-)sputtering, as well as negative thickness by ion etching (Fig. 2.4). Depending on the deposition conditions, different film structures are achievable. As shown in the SZM of Anders' [67] (Fig. 2.4), four regimes can be differentiated and roughly ordered by the rising of *T**, namely *zones 1*, *T*, *2*, and *3*, which have also been described Barna, Adamik, and Thornton [69,82,83]:

- In ***zone 1*** (Fig. 2.3 and 2.4) adatom mobility is very low and leads to small island growth resulting in fibrous grains with pores and low density. Shadowing effects [50,69], where better exposed areas grow faster and low adatom mobility may result in high surface roughness, may occur.
- In ***zone T*** (Fig. 2.3 and 2.4) the grain structure through the film thickness is not homogeneous and is dominated by randomly oriented fibrous grains that form a v-shaped structure. This is caused by a slightly higher surface diffusion compared to *zone 1* and causes competitive grain growth, where more favorably oriented grains grow over other grains. In *zone T* the film structure is denser compared to *zone 1* and *zone T* is a transition zone on the way to *zone 2*.
- Films in ***zone 2*** (Fig. 2.3 and 2.4) are governed by larger columnar grains, than the previous two zones. More adatom diffusion enables more grain boundary mobility and restructuring of the film. With the driving force of surface energy minimization, smaller randomly oriented grains are dissolved as a consequence of grain coarsening and coalescence. The film surface is smooth and the columns with planes parallel to the surface have the lowest surface energy. Films in *zone 2* have comparable density to their bulk counterparts.
- In ***zone 3*** (Fig. 2.4), large equiaxed grains are dominant due to bulk diffusion and recrystallization.

Under real conditions the SZM are not accurate, since impurities, which already have a strong effect in low concentration on the film structure, are not sufficiently considered [82].

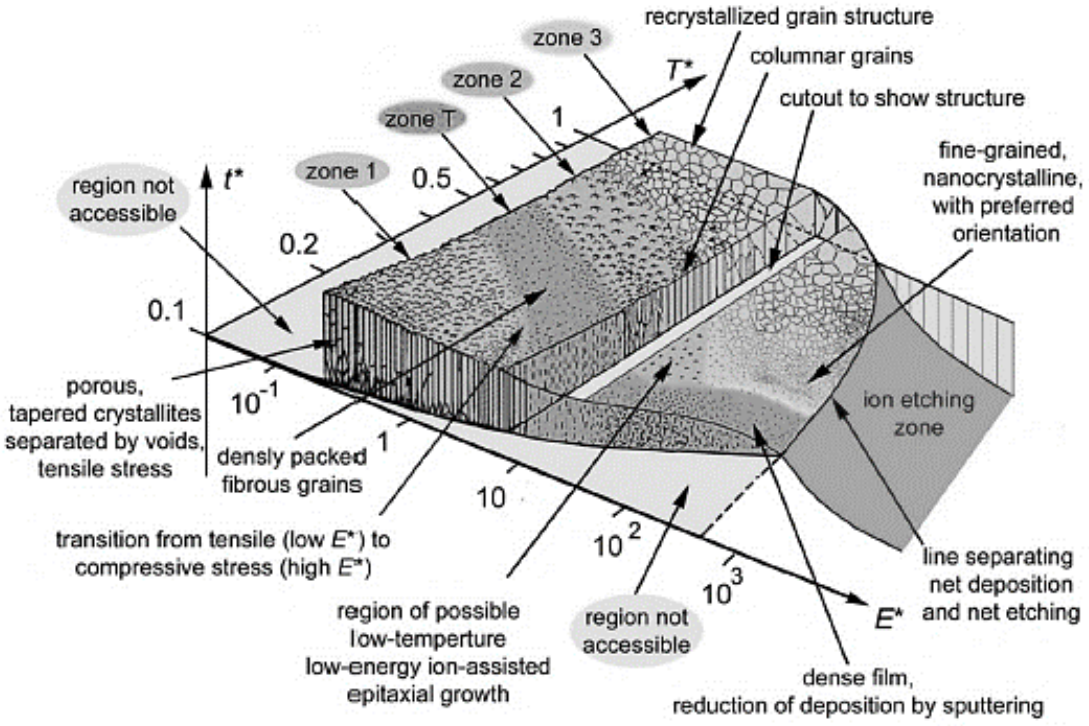

Fig. 2.4 SZM proposed by Andre Anders [67].

2.3 DEPOSITION CHAMBER

All deposited thin film systems in this thesis were deposited in a custom-built laboratory scale dc MSD system (Fig. 2.5), evacuated by a combination of rotary vane pump and turbomolecular pump. The sputter system is grounded and equipped with three unbalanced AJAA320-XP type-2 magnetrons, each controlled by an individual generator. The substrate holder is a rotatable plate and 40 mm opposite of the circular arranged magnetrons. The setup is equipped with Ar as working gas and can add N_2 or O_2 for reactive sputtering.

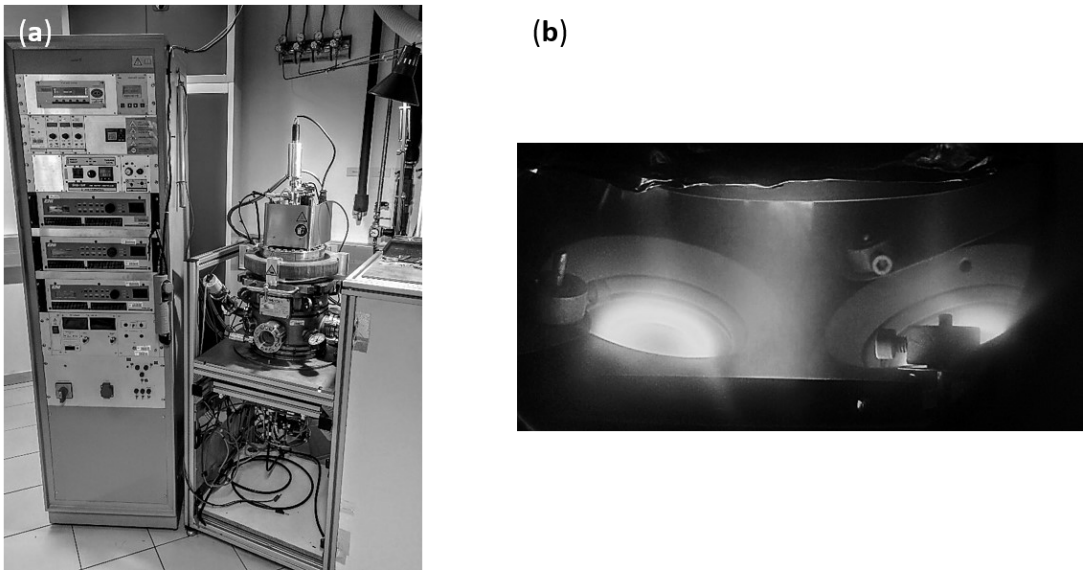

Fig. 2.5 (a) Custom-built laboratory scale dc magnetron sputter device. (b) View inside the operating deposition chamber.

3 ELECTRO-MECHANICAL PROPERTIES OF THIN FILMS

The investigation of the electro-mechanical behavior of thin films is a necessity to determine their suitability in flexible electrical devices, such as foldable displays. A standard testing method is uniaxial tensile loading due to its relative simplicity and speed in execution and analysis [84] compared to biaxial tensile tests [85] and bending tests [86]. The uniaxial tensile tests can be combined with *in situ* 4-point probe (4PP) resistance measurements to relate mechanical with electrical properties and behavior [87,88]. When thin films are bonded to polymer substrates, they display different behavior, compared to free standing films or foils. The substrates help suppress localization of the damage and enable the films to reach higher yield stresses [84,89,90], which makes the investigation of metal-polymer compounds essential. Nevertheless, there is no such thing as an unbreakable material. Flexible TFT display electrodes are composed of multilayer stacks consisting of ductile and brittle films on a polymer substrate [21,22]. When put under uniaxial tensile strain, ductile films form local necks that gradually transform into cracks, while brittle films immediately form through thickness crack s (TTCs) and fracture at low strains [90]. Uniaxial tensile tests of different bilayer systems showed that brittle layers, regardless of their number or position in multilayer stacks, are responsible for the fracture of the multilayer stacks [15,91–96]. However, brittle films are necessary as diffusion barriers and adhesion layers and often cannot be replaced with ductile materials [36,97,98]. Regardless, tuning the film thickness, structure, the grain size, and residual stresses of a film can improve its fracture behavior under uniaxial tensile loading. Smaller film thicknesses and grain sizes have shown to emphasize brittle behavior of inherent ductile films [91,95,99–102]. However, smaller grains have also displayed stronger resistance to electro-mechanical failure as well as compressive residual stresses [42,103]. Alloying of brittle films has also shown to improve the mechanical behavior, but very often is accompanied with a large increase of electrical resistivity [15,44].

The positions of initial necks or TTCs under uniaxial tensile loads are related to randomly distributed defects [4,104]. In brittle materials the maximum tensile strength is defect controlled and can be accounted for by Weibull weakest link models [105,106]. Under tensile load, defects, such as scratches, grain and phase boundaries, voids in the lattice, pores, and impurities, lead to local concentrations of stresses. When the local stress at the defect exceeds the yield stress, necks and TTCs form.

3.1 DUCTILE BEHAVIOR

In free standing films the localization is not hindered and rapture occurs at low strains [107–109]. When the elastic limit is reached, glide planes in accordance with the Schmid factor are activated, leading to shearing of the free standing film with typical shear angles between 40° and 50° upon rupture [110] (Fig. 3.1b). The typical small thicknesses of the films allow dislocations to move across the grains and escape at the surface, which disables strain hardening and facilitates gliding along the planes [111].

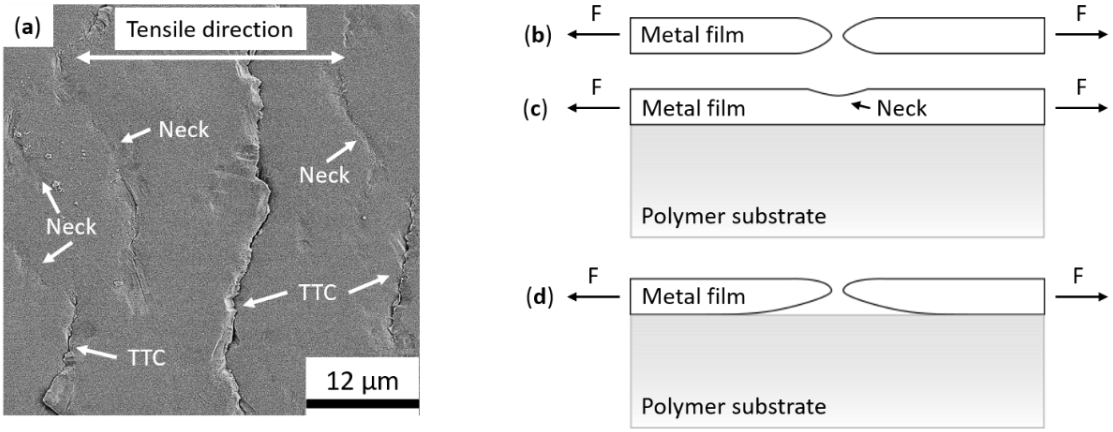

Fig. 3.1 (a) *Ex situ* scanning electron microscopy micrograph of a polymer supported 1 µm thick Cu film with necks and TTCs after uniaxial tensile straining. Types of ductile behavior of metallic films (adapted from [84,90]): (b) free standing film, (c) polymer supported film, and (d) polymer supported film with delamination.

Ductile films under uniaxial tensile loads start to deform from localized deformation, i.e. necking [111]. A neck will form perpendicular to the tensile direction and start to grow with increasing strain until the film will eventually rupture. As illustrated in Fig. 3.1a,c, a ductile film supported by a polymer substrate will form necks beyond its yield strength. However, the polymer substrate distributes strain equally via the interface and delocalizes the strain in the film, leading to numerous randomly distributed necks across the surface as shown in Fig. 3.1a. As a consequence, films bonded to substrates reach higher yield strengths under uniaxial tensile strain compared to their free standing counterparts. Only at high strains, necks propagate through the film and will form TTCs. If the bond between film and substrate is insufficient and delamination takes place, the film can be considered free standing and will form a localized neck with subsequent rupture of the film (Fig. 3.1d). In this case delamination and necking facilitate each other [84,90,111]. However, this phenomena has also been shown to not be true for all metal film-polymer substrate cases [112].

3.2 BRITTLE BEHAVIOR

Brittle films show very little or no local plastic deformation before they fracture at low strains (<1-2%). Brittle films rupture from cleavage, the breaking of a single array of atomic bonds. Under uniaxial tensile load, polymer supported brittle films fracture at low strains and immediately form TTCs perpendicular to the tensile direction as is illustrated in Fig. 3.2a,c. As consequence, polymer substrates do little to prevent the fracture of brittle films (Fig. 3.2b,c). In the fractured film, direct stress transfer is no longer possible. Continued fracture arises from interfacial shear stress between film and polymer [84].

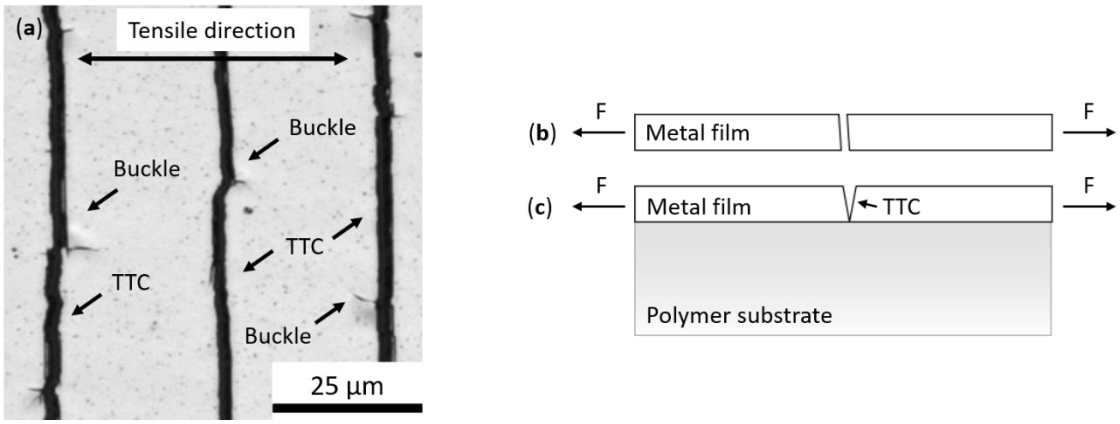

Fig. 3.2 (a) *In situ* confocal laser scanning microscopy micrograph of a polymer supported 440 nm thick Mo film with straight TTCs and buckling at 14% engineering strain. (b) and (c) illustrate the typical brittle behavior of free standing and polymer supported brittle films (redrawn from [90]).

3.3 FRAGMENTATION TESTING

Fragmentation testing is a common method to examine the mechanical behavior of metal or ceramic films on polymer substrates [84,113,114]. The method was adapted from fiber composite materials and has been under continuous development ever since [84,90,115,116]. In fragmentation tests under uniaxial tensile load the number of cracks grows until saturation is reached. A key prediction of crack analysis is that in the saturation regime the shortest and longest observed crack spacings, λ_{min} and λ_{max}, respectively, follow the relation: $\lambda_{max} = 2 \cdot \lambda_{min}$. Fig. 3.3 presents a schematic illustration of the relation between crack spacings and stresses. At the positions x = 0 and x = L, cracks are formed and cause stress relaxation in the film (Fig. 3.3a). Now, the shortest distance for another crack to occur is at a distance of λ_{min}, where shear stress can exceed the fracture strength of the film (Fig. 3.3a). One can imagine that a fragment

of the length λ_{min} can barely transfer enough shear stress to fracture the fragment (Fig. 3.3b). Therefore, fragments exceeding λ_{max} are expected to fracture until all fragments are in a range between λ_{min} and λ_{max}. At this point the saturation regime is reached and no further cracking takes place. This is referred to as the shear lag theory and allows the deduction of the maximum shear stress, τ_{max}, at the interface [117,118]:

$$\tau_{max} = K \frac{h\sigma_f}{\lambda_{sat}}. \quad (3.1)$$

In Eq. 3.1, h is the film thickness, σ_f the film's fracture stress, λ_{sat} the saturation crack spacing and K is a numerical constant (normally equal to π). The models found in literature vary a bit, depending on the usage of the minimum, average, or maximum λ_{sat} value and if residual stresses were accounted for [119]. For a better understanding of periodic cracking concepts and its applications, the reader is referred to Agrawal and Raj's work [113].

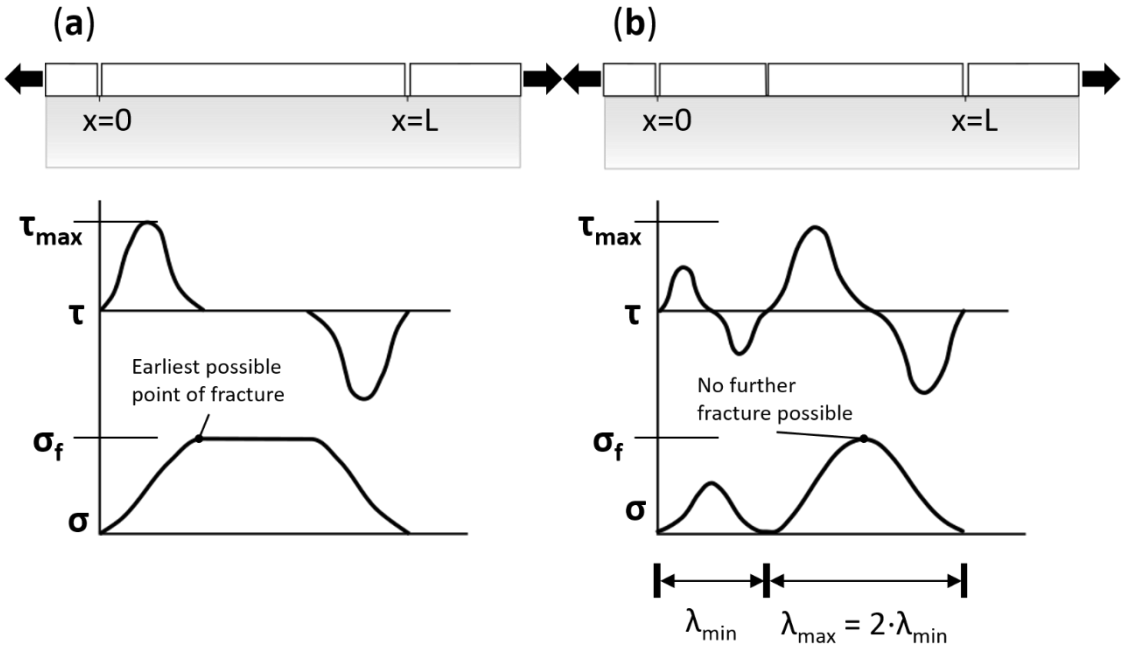

Fig. 3.3 Shear lag model: schematic of theoretical shear and fracture stress as a function of crack spacings (redrawn from [118]).

Once more, consider the fragmentation of a polymer-supported film system under uniaxial tensile load. Analysis of the fractured films yield characteristic values, such as crack onset strain (COS), or initial fracture strain, and λ_{sat}, from which the interfacial shear stress can be derived, as shown in Eq. 3.1. Furthermore, if delamination in form of buckles occurs in the tensile strained fractured films, the evaluation of adhesion is

possible [120] and will be briefly covered Chapter 7. The fragmentation data is usually obtained from accompanying *ex situ* or *in situ* optical microscopy (OM) [121], atomic force microscopy (AFM) [122], scanning electron microscopy (SEM) [123] or confocal laser scanning microscopy (CLSM) [124]. However, *in situ* fragmentation testing is more precise and provides data as a function of the engineering stain. Plotting the evolution of the inverse crack spacing, or crack density, as a function of the engineering strain for brittle films reveals three stages of fragmentation [56,104,125] in accordance with the previously described shear lag model (Fig. 3.4):

- When COS is reached in ***Stage I*** (random cracking), cracks form due to local stress concentration at random distributed defects (weak spots) of the film and propagate perpendicular to the tensile direction.
- With increasing engineering strain in ***Stage II*** (mid-point cracking), the crack spacing approaches the limits for stress transfer according to the shear lag model. The nucleation rate of new cracks decreases. If delamination occurs in this stage, buckles can form due to a Poisson's effect, which induces compressive stresses transverse to the tensile direction.
- In ***Stage III*** (saturation regime), the critical stress transfer length is reached and no further cracks can form. If delamination occurs, it is the dominant mechanism and buckles can form until the substrate ruptures.

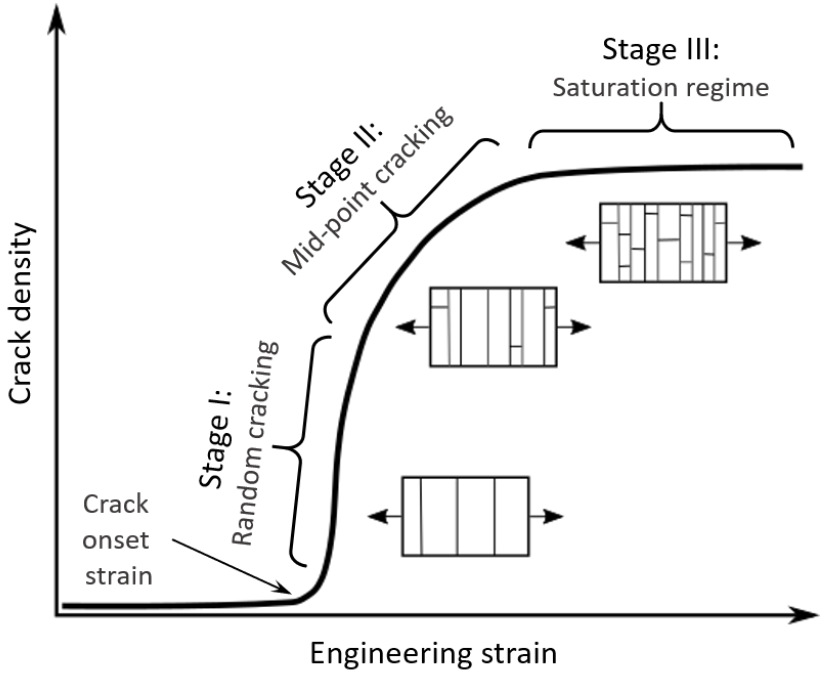

Fig. 3.4 Evolution of crack density as function of engineering strain (adapted from [56,104]). The scheme shows the three stages of brittle film fracture with representative illustrations of the crack patterns (perpendicular to load) and buckles (delaminations, parallel to load).

3.3.1 MONOTONIC *IN SITU* UNIAXIAL TENSILE TESTS

There are various methods to mechanically test a polymer-supported film, such as biaxial tensile straining [126–128], uniaxial tensile straining [129,130] and bending [86,131–133]. The most conventional and easiest method to realize is uniaxial tensile straining, which can be combined with other measurement techniques to gain a more comprehensive understanding of the material behavior.

***In situ* microscopy measurements**

As mentioned before, fragmentation tests are usually accompanied by various microscopy methods, having different advantages and disadvantages, see Table 3.1. Depending on the type of experiment (*ex situ* or *in situ*), the material (ductile or brittle), and the expected or investigated feature size, different imaging techniques may be better suited. The main difficulty of *in situ* fragmentation tests is to fit the tensile setup under the respective microscope. Portable tensile stages are commercially available for most conventional microscopy techniques. However, the vacuum chambers used in SEM are a particularly difficult obstacle for the setup.

Table 3.1 Overview of *in situ* imaging techniques for uniaxial tensile testing

Imaging technique	Resolution	Acquisition time	3D imaging
OM [121]	Low	Fast	No
SEM [123]	High	Medium	No
AFM [122]	High	Slow	Yes
CLSM [124]	Medium	Medium	Yes

In situ CLSM and AFM are able to perform 3D imaging and can be used to distinguish between necks and TTCs in ductile films, as demonstrated for AFM by Cordill and Marx [122]. There, a height ratio Δ/h of 0.15, where Δ is the deformation depth and h is the film thickness, was defined as demarcation between necks and TTCs. In Fig. 3.5a, height profiles of an *in situ* strained Al/Mo 300/30 nm bilayer from CLSM and AFM is shown. The height profiles help to determine if a surface deformation is a neck or a TTC, as is shown in Fig. 3.5a, where the deformation depths are right at the demarcation between necks and TTCs. The height profiles of CLSM and AFM are a good match. The

small lateral mismatch is caused by relaxation of the sample, due to longer recording time of the AFM image and because the AFM image was recorded after the CLSM image. The deformation depths measurement was modified from [122]. Due to the width of the crack gaps, the average height in a distance of ~1 µm from the deepest point was used to determine the deformation depth, *Δ*, as demonstrated in Fig. 3.5b. A direct comparison of Fig. 3.5c,d shows that the CLSM as well as the AFM micrograph look very similar and display the same surface features, however, Fig. 3.5a shows that the slower AFM yields more surface details on a smaller image scale. Both CLSM and AFM are most suitable for *in situ* tensile strained ductile samples, as long as the user is aware of the individual advantages and disadvantages of each technique (see Table 3.1).

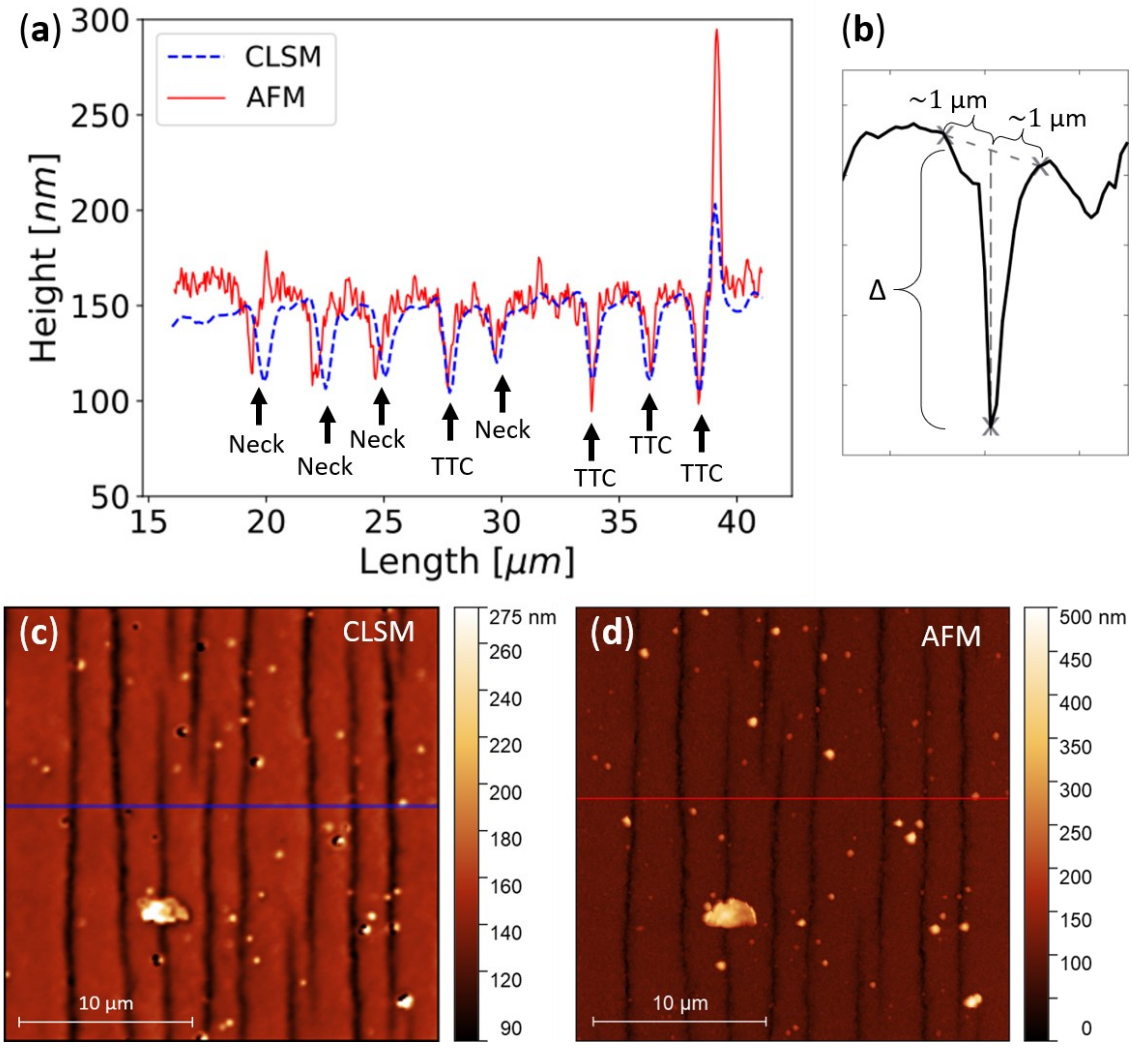

Fig. 3.5 Comparing CLSM and AFM imaging of an *in situ* strained polymer supported Al/Mo 300/30 nm bilayer at the same areal position. (a) Height profiles of CLSM and AFM at the same position. (b) Schematic neck/crack depth, *Δ*, determination. (c) CLSM and (d) AFM micrograph of the same area marked with the respective height profiles extracted in (a).

In situ 4PP measurements

Other fragmentations tests include *in situ* 4PP measurements, to relate mechanical and electrical behavior to each other. For electrodes in flexible TFT displays, besides the ability to withstand fracture against stretching and bending, the electrode's electrical resistance plays an important role for its function. The incorporation of the 4PP measurements into the tensile grips for polymer-supported thin film testing is easy to realize [87,88], and sketched in Fig. 3.6. *In situ* monitoring of the 4PP resistance has proven to be a precise method to determine COS of brittle films due to its sensitivity to defects and matches, in general, well with the results from *in situ* imaging techniques. An exception are ductile films in the range of 100 nm thickness and more, where the formation of necks can be observed earlier with imaging techniques than with electrical resistance measurements, due to its slow electrical response (Fig. 3.7a). Initial necking of thick tensile strained ductile films hardly changes the measured electrical resistance of the film and therefore shows a too late response (Fig. 3.7b,c). Simplified finite element models show that initial shallow necks barely hinder the electrical current flow (Fig. 3.7c). The COS with electrical 4PP measurements can be identified as the deviation of the normalized electrical resistance, R/R_0, from the theoretical behavior [87,88]

$$\frac{R}{R_0} = \left(\frac{L}{L_0}\right)^2 = (1+\varepsilon)^2 \,. \tag{3.2}$$

In Eq. 3.2, R and R_0 are the respective electrical resistance and initial resistance, L and L_0 are the respective gauge length and initial gauge length and ε is the engineering strain. The theoretical behavior assumes volume conservation and is only applicable as long as there is no damage of the measured film. Once necks, cracks, or grain growth occurs, the measurements will deviate from Eq. 3.2. R/R_0 after deviating from Eq. 3.2 is difficult to interpret. R/R_0 still increases when crack density reaches saturation. Glushko et al. [134] showed for ductile films that there is a strong dependence of R on the crack length, which still grows due to the fusion of shorter cracks to longer cracks in the saturation regime. Glushko et al. [135] has also demonstrated a recovery of the electrical resistance for ductile films during unloading of the films. Brittle films with their long TTCs display a continuous increase of R/R_0 during straining, which is likely related to the loss of conducting bridges.

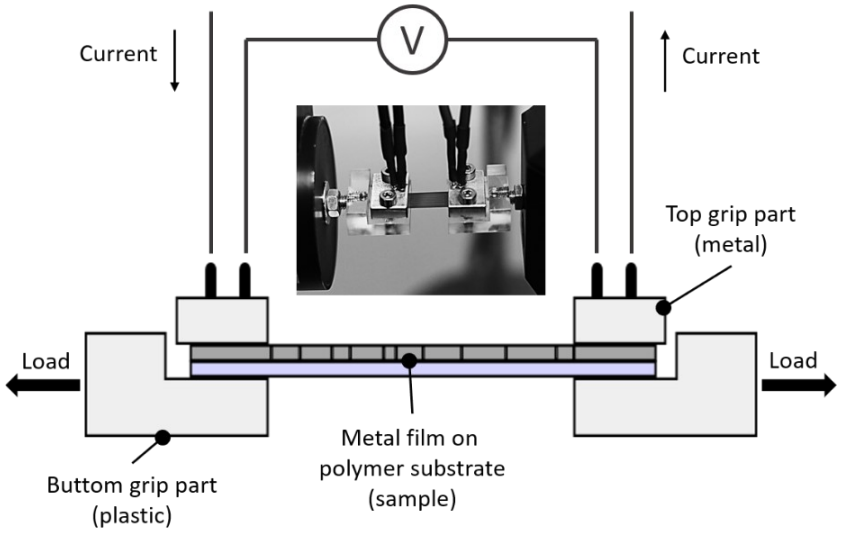

Fig. 3.6 Schematic of an *in situ* 4PP tensile test setup (redrawn form [88]). The inset shows a picture of the setup with a mounted sample.

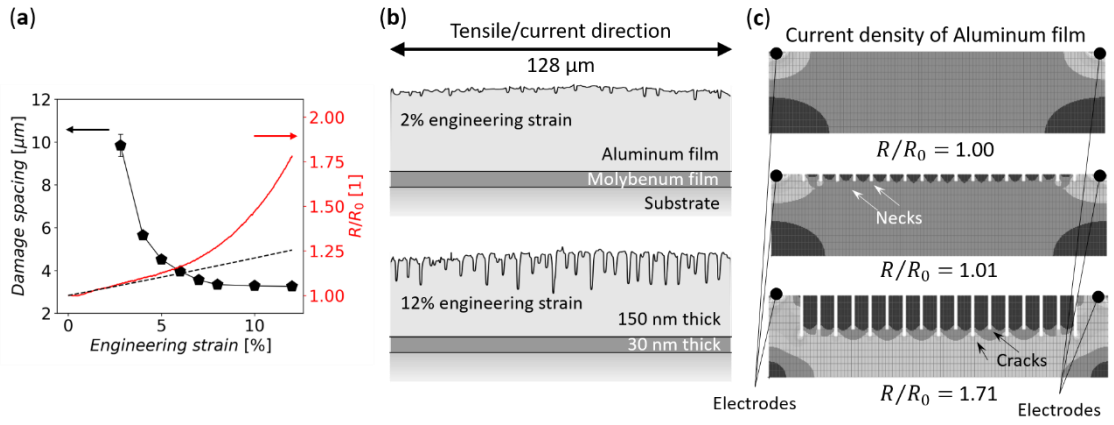

Fig. 3.7 *In situ* tensile behavior of a polymer supported Al/Mo 150/30 nm thick bilayer. (a) In red R/R_0 (from 4PP measurements) and in black the crack spacing (from CLSM). (b) Extracted height profiles at 2 and 12% engineering strain. (c) Current density from finite element simulations of a sample without damage and with damage similar to (b).

In situ XRD measurements

Advanced fragmentation test techniques on crystalline thin films include *in situ* X-ray diffraction (XRD) to determine the evolution of film stresses as a function of engineering strain. Typically, experiments are performed with synchrotron radiation, due to faster measurement times, more intensity and higher brilliance of the X-ray beam compared to laboratory instruments [136,137]. While measurements for the uniaxial case (parallel or perpendicular to the straining direction) [91] are more common due to their relatively

simpler realization, biaxial measurements [85] are more suitable to actual flexible application loads.

To determine in-plane film stresses in XRD measurements, the crystalline lattice spacing, *d*, and its shift due to internal or external (compressive or tensile) stresses is measured from which subsequently lattice strain and film stress can be derived. The *d*-spacing is determined from the scattering angle *2Θ* of diffraction peaks fulfilling Bragg's Law ($n\lambda = 2d\ sin\,\Theta$), knowing the wavelength of the X-ray beam, λ. The elastic strain, $\varepsilon_E = \Delta d/d_0$, is determined by the peak shift Δd and the unstrained lattice spacing, d_0 [136,138]. The film stress can be calculated from the elastic strain using Hooke's Law.

In the $\sin^2\psi$ analysis [138,139] the elastic strain, $\varepsilon_{\varphi\psi}$, is measured as a function of ψ at a fixed φ position (parallel or perpendicular to the straining direction in uniaxial tensile tests) (Fig. 3.8a). Rotating along several ψ angles, planes at an angle to the surface fulfilling Bragg's Law are measured. Assuming a biaxial stress state for thin films ($\sigma_{11} = \sigma_{22}$, $\sigma_{33} = 0$) the principal equation to determine film stress with the $\sin^2\psi$ method is written as [138]

$$\frac{d_{\varphi\psi} - d_0}{d_0} = \left(\frac{1+\nu}{E}\right) \cdot \sigma_\varphi \cdot \sin^2(\psi) - \left(\frac{\nu}{E}\right) \cdot (\sigma_{11} + \sigma_{22}). \qquad (3.3)$$

E and *v* are the elastic constants of the film and σ_φ is the in-plane stress. From the resulting slope (Fig. 3.8b), which predicts a linear behavior of the *d* vs. $\sin^2\psi$ curve (Eq. 3.3), σ_φ can be obtained. For a good quality of the results a wide range (from 0 to 1) of $\sin^2\psi$ is recommended, which is often not possible due to beam shielding and detector collision.

The elastic properties *E* and *v* in Eq. 3.3 are replaced by the X-ray elastic constants (XEC) S_1 and $S_2/2$ to account for the elastic anisotropy of the crystal structure [138]. Using different models (Voigt [140], Reuss [141], Eshelby/Kröner [142,143], or Hill [144]) for interactions between crystals, XECs can be experimentally determined for new materials [145] or calculated from data bases.

I*n situ* XRD fragmentation tests in reflection geometry enable further insights into the mechanical behavior of the films. This method also can be used to determine the film stresses of multilayer stacks (Fig. 3.8c), when each layer is made of a different material, otherwise the resulting film stress will be an average of the layers made of the same material. In Fig. 3.8c, the combination of three monotonic *in situ* uniaxial tensile measurement methods, 4PP, microscopy, and XRD, on polymer supported Al/Mo 150/30 nm thick bilayers are displayed. The stress measurements indicate a fracture of the bilayer before it becomes visible by CLSM, which is probably attributed the limited

observed area in the microscope during random cracking and to initially shallow necking of the ductile Al layer. The *in situ* XRD measurements in Fig. 3.8c enable the observation of the stress evolution of the individual Mo and Al layers in the bilayer film system and show their individual behavior.

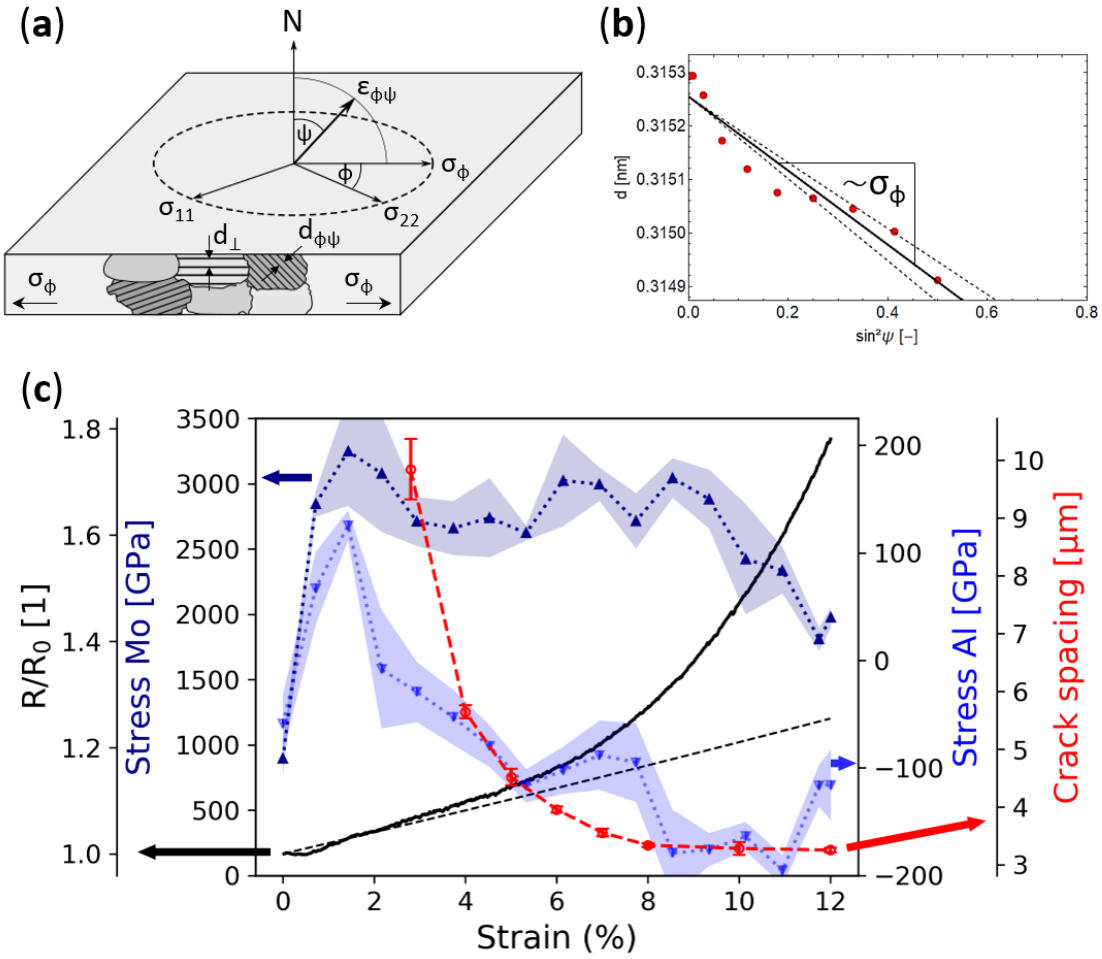

Fig. 3.8 (a) Schematic diagram of the XRD-sin²ψ in-plane stress measurement of thin films, showing the diffraction planes and lattice spacings parallel to the surface, $d_\perp$, and at an angle $\varphi\psi$ with $d_{\phi\psi}$ (redrawn from [139]). (b) Exemplary d vs. $\sin^2\psi$ plot, showing the in-plane film stress proportional to the slope, which can be calculated from XECs. (c) Combination of advanced monotonic *in situ* uniaxial tests (4PP with the normalized resistance R/R_0 + microcopy with crack spacing + XRD with stresses), showing the straining behavior of a polymer supported Al/Mo 150/30 nm thick bilayer. The theoretical resistance behavior (Eq. 3.2) is shown as black dashed line.

However, the following limitations of this method have to be put under consideration: (i) samples have to be crystalline, (ii) a minimum film thickness is necessary to obtain a peak signal (~50 nm, material and X-ray beam dependent), (iii) only little sample texture is tolerable, otherwise it inhibits the ψ range for $\sin^2\psi$ analysis, and (iv) the beam wavelength has to be similar to the atomic spacings of the sample.

3.3.2 INTERMITTENT CYCLIC BENDING TESTS

As mentioned in Chapter 1, recent developments in industrial and university research in electronics lead towards flexible electronic devices. Among them are flexible foldable and rollable TFT displays, of which electrode development and characterization is the main focus of this thesis. Cyclic bending tests closely resemble folding and rolling processes, which are better suited to evaluate the robustness and reliability of potential electrode thin films or whole flexible devices. Compared to uniaxial tensile tests of conductive films, in cyclic bending tests bending radii in the range of 20 to 1 mm are used [27], which roughly correspond to bending strains of 0.3 to 3.0%. The bending strain, ε_b, is determined by the relation $\varepsilon_b = d_s/2r$, where d_s is the substrate thickness and r is the bending radius [146] and is further illustrated in Fig. 3.9a. For TFT structures on polymer substrates, the thin film thickness, which is commonly in a range of a few hundred nm thickness, is negligible for ε_b compared to the substrates with several tens of µm thickness. In bending tests the applied strain is relatively low compared to uniaxial tensile tests (<5%), however, cycle repetitions in the range of a few thousand to several hundred thousand may lead to similar damage densities, as shown for Al/Mo bilayer systems on polyimide (PI) substrates [15,17] (compare Chapters 4 and 6). High numbers of bending cycles lead to cumulative damage. The resulting cumulative damage depends on the material system, the film thicknesses, the applied bending strain, and the type of applied bending [16,17] (see Chapters 5 and 6).

Theoretically, during bending experiments, compressive, tensile and mixed (alternating between compressive and tensile) bending loads can be applied (Fig. 3.9b). The different types of bending loads can be generally ordered by the severity of damage. Under the same conditions the different types of bending loads can be ordered with increasing destructiveness as compressive, tensile, and mixed, respectively [86]. The terms compressive, tensile, and mixed refer to the stresses applied to the studied film or TFT structure during a bending action.

The resulting damage may vary quite a bit, whether the materials tested under cyclic bending are ductile or brittle. Depending on the relaxed or bent sample investigated, an analysis may come to different conclusions. Tests on ductile evaporated Ag and brittle printed Ag film samples showed that cyclically bent films with brittle behavior have closed crack gaps in the relaxed state, while ductile films show more plasticity and opened crack gaps with extrusions, resulting in higher surface roughness [146]. On the other hand, the opened crack gaps of brittle samples in the bent state are expected to either lose all or the majority of its electrical conductivity. Most electronic

flexible devices are expected to function in their relaxed and mechanically loaded state, since avoiding cracks is the most desirable goal.

A bending setup with a defined and exchangeable radii equipped with *in situ* electrical, optical, and even XRD measurement possibility would be the most ideal one. However, in reality, among the many existing and proposed bending setups for metallizations on polymers, such as 4-point bending, micro beam bending, and bending with and without defined radius, the desired ideal setup is not among them [131,133,147–153]. In general, *in situ* bending has often limitations regarding the maintenance of a constant bending radius or the localization of the bent area. Often the radius cannot be changed or the radius is an ellipsoid, which makes analysis more difficult. Also, the integration of optical, electrical and XRD measurements is difficult to integrate into an *in situ* bending setup. Therefore, many concepts are in existence, having various advantages and disadvantages for specific analyses. The various types of bending concepts have as common issue, the lack of a common failure criterion. For testing flexible devices the maintenance of their function is used as a failure criterion, while a deterioration of the functions is observed, but not further considered [27,30,37,154,155]. In case of flexible polymer-supported electrodes there is no common failure criterion or an acceptable threshold for cracks and conductivity [131,133,147–153]. Only, Sim et al. [156] suggested R/R_0 reaching 25% as failure criterion based on their observations on the damage behavior of polymer-supported evaporated Ag films under cyclic uniaxial tensile loads.

In the current thesis, a custom built bending apparatus, the FLEX-E-TEST [86], was utilized, see Fig. 3.9c. The FLEX-E-TEST consists of grips for sample mounting, attached to a wheel. The rotation of the wheel is controlled by a computer and allows the application of compressive, tensile, and mixed bending loads (Fig. 3.9b). The samples are mounted onto grips, which have a defined radius and are exchangeable with other grips of different radii. During a bending action a grip approaches the anvil. This motion forces the sample once it reaches the anvil to bend along the radius of the grip until the grip passes the anvil (Fig. 3.9b). During the bending of the film, the bent area of the film does not touch the anvil. Repeated tests have shown that the FLEX-E-TEST causes an unequal damage density distribution, which has to be compensated by the evaluation of the areas with higher damage density, which are closer to the grips. The setup allows continuous cycling of the sample and can be performed in an intermittent mode in combination with CLSM and 4PP resistance measurements in the relaxed sample state. Further details regarding the operation and evaluation of the FLEX-E-TEST can be found in Chapters 5, 6, and 8.

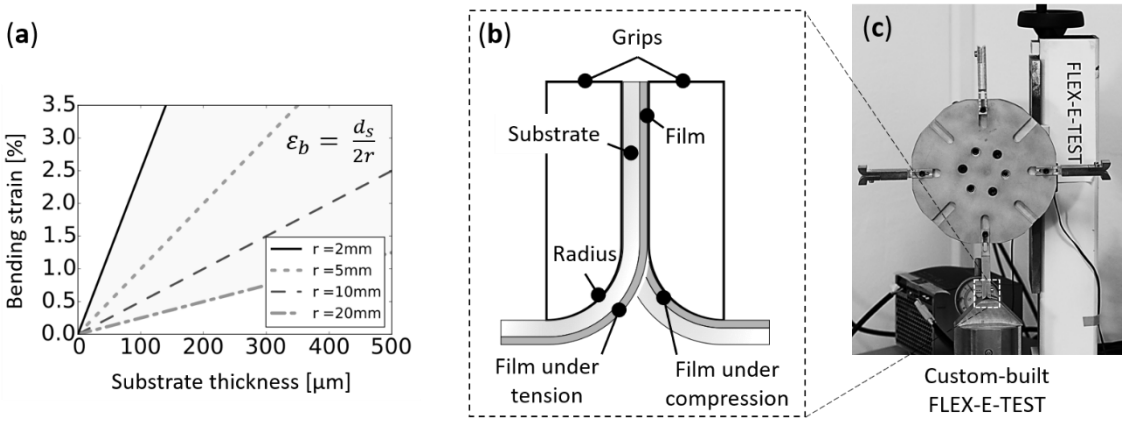

Fig. 3.9 (a) Overview of the relation between substrate thickness, radius, and bending strain. (b) Schematic of the mounted sample under different stress conditions dependent on the movement direction of the FLEX-E-TEST. (c) Picture of the custom-built bending device, the FLEX-E-TEST

Chapter 4 was almost identically published by the author of this thesis in [15]. In the current thesis, all superfluous equations were replaced with references to the main text. Furthermore, the figure and reference numbering was adapted to fit the thesis.

4 ELECTRO-MECHANICAL BEHAVIOR OF AL/MO BILAYERS STUDIED WITH *IN SITU* STRAINING METHODS

4.1 INTRODUCTION

Metallic thin films deposited on polymer substrates enable flexible and lightweight applications for sensors, mobile energy sources, microelectronics and display technologies [1, 2]. Depending on the desired application, different demands on material systems are of relevance [3, 4]. Frequently, multilayer systems are chosen in order to combine the advantageous properties of each individual layer into one single composite system [5, 6]. These multilayer systems often consist of ductile and brittle materials, where thin brittle layers can increase the adhesion to the substrate or act as diffusion barriers [160]. Little is understood about the mechanical behavior of multilayer films on polymer substrates and their influence under tension, compression, or bending. For fully functional flexible devices, manufactured from both ductile and brittle materials, further investigation of the electro-mechanical behavior of multilayer films is of importance. When loaded in tension, brittle films typically fracture at low strains and ductile films locally thin in the form of necks [90]. In general, it has been found that brittle layers cause ductile layers to act in a more brittle manner under tensile strain, leading to a potential failure of the multilayer system [91–93]. As shown by Putz et al. for the system Au/Cr, the brittle Cr layers induced cracks that usually do not form in a ductile Au film and lead to early electrical failure [93].

The combined ductile and brittle mechanical behavior has been under investigation in bilayer and nanoscale multilayer film systems [91–96]. The role of the brittle layer fracture on the ductile layer is of special interest. Both Gruber et al. [95] and Marx at al. [91] observed higher film stresses when the Cu layer thickness was decreased in Cu/Ta or Cu/Cr systems, respectively. These studies of Cu layers with increasing thicknesses on brittle Cr [91] and Ta [95] layers also reported a strong influence of the brittle layer and its thickness on the crack morphology and film stress of the ductile layer. Polyakov et al. [94] further demonstrated the influence of ductile layer thickness under tension with XRD of nanoscaled multilayers. It was shown that ductile Cu layers (2 – 20 nm) in Cu/Nb multilayers exhibited increased strength and failure strain when

they were thinner [94]. The brittle Nb layers (10 nm) showed decreased strength and strain, appearing to be a type of load-share behavior between the layers [94]. What these studies have in common is that the addition of brittle layers can dramatically decrease the fracture strength of the whole film system under tension.

Brittle interlayers can be necessary for strong adhesion between substrate and ductile layer. One way to decrease the influence of the brittle behavior on the ductile layer is to optimize the ductile/brittle film thickness ratio [91,92,94,95]. The influence of the interlayer has been shown to become less evident by increasing the thickness of the ductile layer by an order of magnitude compared to the brittle interlayer [91,92,94,95], however, a more systematic study has not yet been performed. The current study focuses on the electro-mechanical performance of sputter deposited molybdenum (Mo) thin films on flexible PI substrates [42] by changing the thicknesses of ductile aluminum (Al) layers. These Al/Mo bilayers are similar to the material system used in current display technologies and allow for the suitability for flexible display applications to be evaluated. *In situ* fragmentation tests were used to investigate the electro-mechanical behavior of the flexible bilayer systems [15, 16]. Different Al/Mo thickness ratios (1:1, 3:1, 5:1 and 10:1) were tested with *in situ* tensile tests to determine the optimal thickness ratio for fully working flexible devices. The tensile tests combine 4PP resistance measurements and surface imaging techniques, such as SEM and CLSM [92], which enable the observation of electrical conductivity and of the evolution of surface deformation during straining as well as allowing for a correlation of how local deformation in ductile films manifests in resistance measurements.

4.2 MATERIALS AND EXPERIMENTS

The studied material system consisted of bilayers of Al (top) and Mo (bottom) thin films (Al/Mo) on flexible PI substrates. The brittle Mo layer acts as an adhesion layer, while the Al is the charge carrying layer. A laboratory scale dc magnetron sputter system was used to synthesize a series of Al/Mo bilayered thin films on 50 and 125 µm PI (UBE Upilex-50S) substrates. The substrates were fixed with Kapton tape on a rotatable sample holder at a distance of 40 mm from the target. Powder metallurgically prepared Mo (99.97% purity, Ø 50.8 mm, provided by Plansee SE) and Al (99.99% purity, Ø 50.8 mm, provided by J. Lesker) targets were mounted on two unbalanced AJA A320-XP magnetrons. The base pressure of the chamber before each deposition run was below 1×10^{-3} Pa. Prior to deposition the substrates were plasma cleaned for 2 min with an asymmetrically bipolar pulsed dc plasma of -350 V and 50 kHz at an Ar pressure of

1 Pa. For thin film deposition the targets were subsequently operated by a dc current in power controlled mode, using 156 W for Mo and 166 W for Al, at a constant Ar pressure of 0.5 Pa in order to yield equivalent deposition rates of 35 nm/min for both metals. The deposition rates were determined from the deposition time of test depositions for both metals and their respective film thicknesses. Four different bilayered samples with different thickness ratios of Al/Mo (1:1, 3:1, 5:1 and 10:1) and one single layered Mo sample (30 nm) were fabricated to study the influence of the ductile film thickness on fracture and deformation during tensile straining. The above deposition parameters led to deposition times of 51 s for a layer thickness of 30 nm, 2 min 8 sec for 75 nm, 4 min 16 s for 150 nm and 8 min 32 s for a layer thickness of 300 nm. The thicknesses were verified from focused ion beam (FIB) cross-sections in the SEM. The 10:1 bilayer and the 30 nm Mo film were deposited onto a 50 µm PI substrate, while the other bilayers were deposited on 125 µm PI substrates. Cordill et al. [161] demonstrated for chromium thin films on polyethylene terephthalate substrates that the substrate thicknesses have no significant influence on crack initiation and crack spacing of metallic thin films.

The grain sizes of the Al layers were attempted to be evaluated with electron backscatter diffraction. However, due to the low Al thicknesses (30 nm-300 nm), it was only possible to characterize on the 300 nm Al film (10:1). Using a step size of 30 nm, it could only be determined that the film microstructure was bimodal consisting of very few 100 nm grains in a nanocrystalline matrix smaller than 30 nm. Also, as known for sputter deposited films, the grain size is typically on the order of the film thickness. Therefore, the grain sizes of the Al films are considered similar nanosized and will not greatly influence the mechanical behavior.

Two types of *in situ* tensile straining experiments were performed using samples that were cut from the substrates with a scalpel to the size of 6 mm $\times$ 40 mm. The first *in situ* experiments with 4PP electrical resistance measurements were performed to observe the change of the electrical resistance of the bilayer systems under continuous tensile load. In the *in situ* 4PP tensile experiments, the bilayers were continuously strained with a displacement rate of 5 µm/s to a maximum engineering strain of 12% using a commercial MTS Tytron 250 device, which recorded load, displacement and time. The electrical resistance was measured simultaneously using the 4PP method with the electrodes integrated into the grips holding the sample with an initial gauge length of 20 mm. The resistance was measured with a digital multimeter (Keithley Model 2000 Multimeter). Following the procedure of Glushko et al. [88], resistance was recorded as a function of time using the free software Scilab [162]. According to literature

[87,88,130,163,164] the theoretical resistance of a conductive film increases due to the change of the sample geometry under strain assuming a constant volume and resistivity of the sample. This is described by Eq. 3.2 [87,88,130,163,164]. This relation is applicable until substantial structural changes in the film occur, for example, necks and TTCs. Thus, when the COS is reached the observation of TTCs is likely, allowing for an indirect determination of the presence of cracks with electrical resistance measurements. In this study the electrical failure or COS is defined as a 10% deviation from the theoretical resistance acquired from Eq. (1). The initial resistance measurements before straining were also used to evaluate the bilayer resistivity. The film resistivity was calculated from the experimental data including gauge length, film thickness, sample width and initial resistance, using $\rho = R\ {}^{A}/_{l}$, where ρ is resistivity, R is electrical resistance, A is the cross-sectional area of the bilayer film and l is the initial gauge length. Adding an Al layer to a 30 nm Mo film decreases the resistivity of the bilayer film system. The resistivity reaches a plateau at 6 to 7 µΩcm (Table) for Al/Mo thickness ratios greater 1:1. As a reference the resistivity of sputter deposited 100 nm pure Mo films range between 12 and 40 µΩcm [165]. The resistivity of 1 µm pure Al films deposited by chemical vapor deposition is found to be around 3 µΩcm [166].

The second *in situ* experiments were performed via the combination of a tensile straining device with an Olympus LEXT 4100 OLS CLSM which allows for 3D imaging of surfaces. These experiments were utilized to observe the deformation onset strain (DOS) and COS as well as to evaluate the deformation and TTC spacings under tensile strain. Two small scale tensile stages were used for these experiments. Using the long distance lenses of the Olympus LEXT 4100 OLS CLSM, the Anton Paar TS 600 straining stage was utilized and with the short distance lenses the straining of the samples was performed with a custom-built screw driven tensile device [167]. The use of two different tensile devices and lens systems for the *in situ* CLSM experiments yields the best resolution of the surface images for quantitative deformation analysis. The samples mounted on the Anton Paar straining stage were discontinuously strained under the microscope up to a maximum of 12% engineering strain with a displacement rate of 5 µm/s. Roughly 15 pauses with a holding time of 2 minutes each were made for image recording. The displacement of the custom-built straining device is controlled manually using a screw-driven mechanism. The engineering strain is calculated from external measurements of the gauge length with a high-precision caliper to a maximum strain of 14.4% (using 25 pauses for imaging). From the recorded laser intensity and height topography images the evolution of surface deformation and crack formation as a function of applied strain were obtained. To differentiate shallow necks and TTCs, the

Δ/h ratio (*Δ* is the deformation depth and *h* is the Al layer thickness) was adopted from Cordill et al. [122,130]. Necks have *Δ/h < 0.15* and TTCs have *Δ/h > 0.15.*

To investigate deformation initiation and crack propagation through the bilayer, cross-sectional analysis was performed on selected samples after straining. FIB milling using a LEO 1540XB workstation (Zeiss) with a milling current of 100 pA was performed to cut cross-sections into the bilayers. For a comparison of the cracked Mo interlayer and the deformation of the Al layer after straining, the Al layers were etched away with a 30% sodium hydroxide solution. Depending on the thickness of the Al layer, the etching took approximately 10-30 s. The saturation crack and deformation spacing of the respective Mo and Al layers for each bilayer system as well as the single 30 nm Mo film were confirmed from SEM images using the software ImageJ [168]. The crack or deformation spacing of each sample was averaged from at least three images recorded from different positions on the sample. For each image, three line profiles parallel to the straining direction were used for the determination of the crack or deformation spacing.

4.3 RESULTS

The electrical response of the bilayers during uniaxial tensile straining for different Al layer thicknesses is shown in Fig. 4.1. For better comparison of the samples, the normalized resistance, R/R_0, is displayed as a function of engineering strain. During loading, R/R_0 increases continuously following the theoretical constant volume approximation (Eq. 1) [87,88,130,163,164]. It is evident that thicker Al layers have a beneficial effect on the resistance compared to the brittle Mo single layer. The resistance at high strains is orders of magnitude lower with thicker Al layers compared to the 30 nm Mo film. Furthermore, thicker Al layers also delay the COS determined from the *in situ* 4PP experiments. The 10:1 bilayer, which has the highest thickness ratio among the tested samples, showed that no COS was observed for strains up to 12%. A comparison of COS values showed that increasing the Al layer thickness has a proportional beneficial effect on the COS (Table).

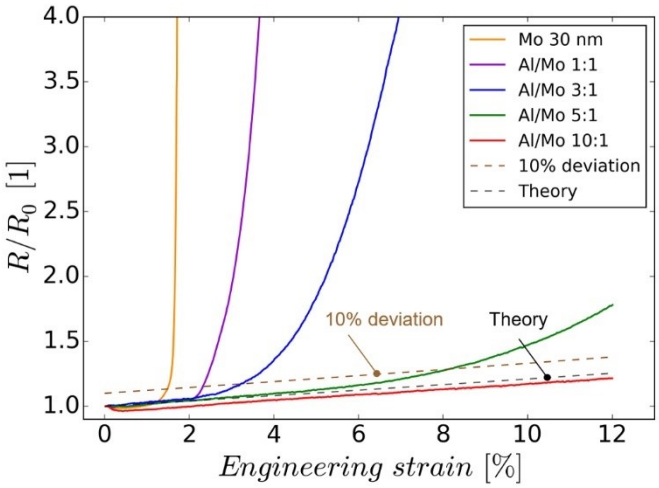

Fig. 4.1 Representative normalized resistance R/R_0 vs. engineering strain at a displacement rate of 5 µm/s. The increase in the Al layer thickness leads to a retardation of resistance increase and lower R/R_0 at higher strains. The dashed lines represent the theoretical resistance behavior and the threshold for electrical failure at 10% deviation from the theory.

Table 4.1: Summary of the values obtained from in situ tensile tests. The crack and deformation spacings were determined with post mortem SEM images. COS and resistivity values are averages of 2 to 4 electrical measurements. Deformation onset strain (DOS) was obtained from a single in situ measurement with CLSM.

Samples	Bilayer resistivity [µΩcm]	COS [%]	DOS [%]	Saturation crack spacing – Mo (ε = 12.0%) [µm]	Saturation deformation spacing – Al (ε = 12.0%) [µm]
Mo 30 nm	26.6 ± 1.1	1.6 ± 0.08	0.97	2.3 ± 0.1	-
Al/ Mo 1:1	13.5 ± 0.8	2.1 ± 0.20	2.00	3.1 ± 0.2	3.1 ± 0.4
Al/ Mo 3:1	7.3 ± 0.3	3.6 ± 0.38	2.45	3.4 ± 0.2	3.4 ± 0.2
Al/ Mo 5:1	6.0 ± 0.2	8.8 ± 0.66	2.80	3.2 ± 0.2	3.2 ± 0.3
Al/ Mo 10:1	7.0 ± 0.1	-	< 4.00	2.0 ± 0.2	2.4 ± 0.2

Fig. 4.2 shows a direct comparison of the deformation morphology from *in situ* CLSM tensile tests at the DOS, Fig. 4.2a-e, and at the maximum strain (12%), Fig. 4.2f-j. While in Fig. 4.2a-d (Mo, 1:1 to 5:1) long straight necks were observed at the DOS, in Fig. 4.2e (10:1) necks were hardly detectable and are marked by black arrows. The barely visible short necks in the 10:1 bilayer become more distinct during straining (Fig. 4.2j). At 12% strain the 30 nm Mo film shows numerous cracks and even buckles (delaminations at the Mo-PI interface). With the addition of thicker Al layers, the occurrence of buckles is suppressed.

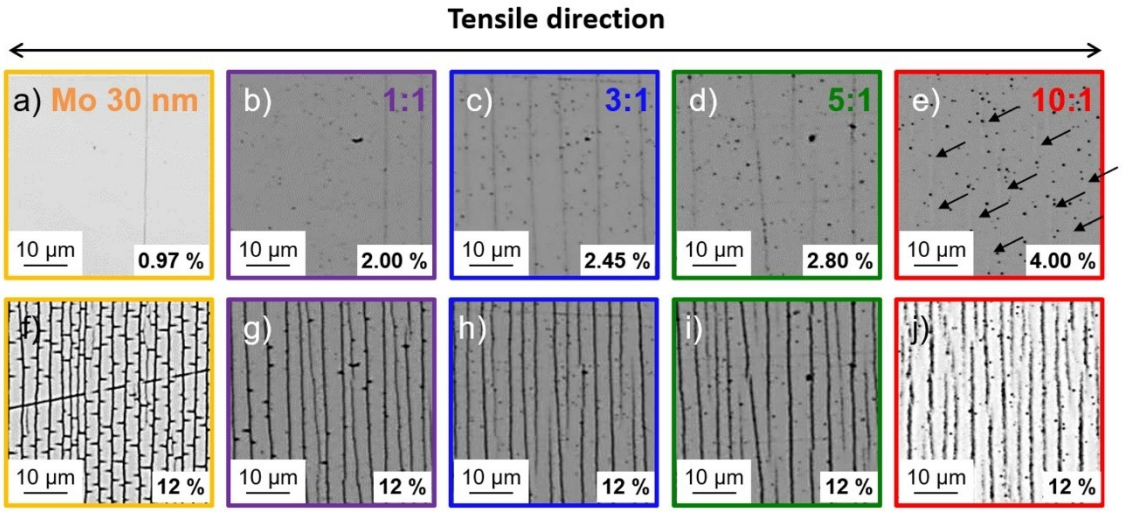

Fig. 4.2 Extracted images of the CLSM images obtained from in situ tensile experiments. Tensile direction is indicated by the arrow. (a)-(e) illustrate the film surfaces at the DOS, noted in the lower right corner. While in (a)-(d) straight deformations are visible, the deformations in (e) are hardly visible and indicated by black arrows. (f)-(j) show the same positions of the respective bilayers at 12% strain, where deformation saturation occurs (at 8% to 10%).

Using *in situ* tensile straining combined with CLSM, the evolution of crack (Mo) and deformation spacing (Al/Mo) was obtained as a function of applied strain (Fig. 4.3). It should be noted that the deformation spacing is a measure of distance between shallow necks and TTCs, whereas the crack spacing only include the distance between TTCs [167]. All bilayers show saturation of the deformation spacing at the end of the tensile experiment. For the Mo film and the 1:1 bilayer, the deformation spacing is equivalent to the crack spacing since only TTCs were observed. Similar to the COS in Fig. 4.1, the DOS was determined as the strain where first deformations were observed on the Al surface. A comparison of the COS and DOS values (Table) shows that for the 1:1 thickness ratio electrical and mechanical failure are in good agreement, however, with increased Al layer thickness the COS is more delayed compared to the DOS and is a direct effect of the Al layer thickness.

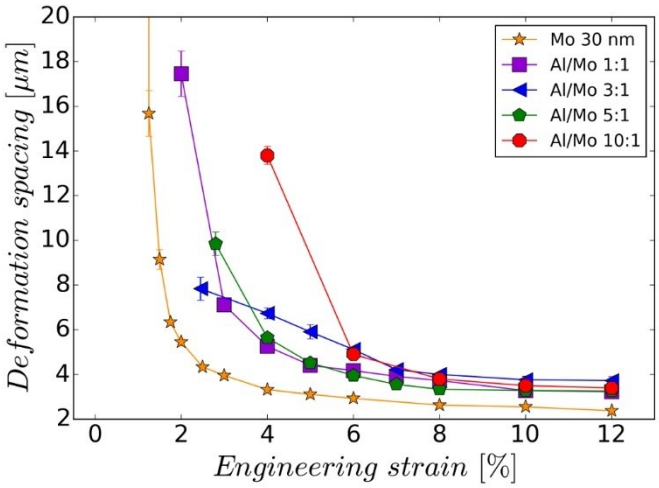

Fig. 4.3 The evolution of deformation spacing of the thin films during the in situ straining with CLSM. For the Mo film and the 1:1 bilayer the deformation spacings are equivalent to the crack spacing. The lines have no mathematical meaning and are only used to guide the eye.

An overview of the post mortem saturation deformation and crack spacings of the 30 nm Mo film and the bilayer systems at 12% strain is shown in Fig. 4.4a. The deformation spacings in the Al layers tend to be slightly higher compared to the single 30 nm Mo film. However, the trend does not seem to correlate with the thickness of the Al layer. The highest deformation spacing for the Al surface in Fig. 4.4a was recorded for the 3:1 ratio with 3.4 ± 0.2 µm in Table . The lowest deformation spacing of 2.4 ± 0.2 µm was found in the Al layer with the 10:1 ratio and is close to the crack spacing of the 30 nm Mo reference with 2.3 ± 0.1 µm. To investigate crack density of the buried Mo layer, the Al film was etched away with a 30% sodium hydroxide solution. Fig. 4.4b shows a CLSM image of the etched 10:1 bilayer with SEM micrograph insets after straining up to 12%. The white dashed lines demarcate the borders of the etched area. A comparison of the reference Mo film and the adjacent Mo films in the bilayer stacks after etching is included in Fig. 4.4a revealing a similar trend as the unetched Al top layers. The deformation spacings in the Al layers are approximately the same as the crack spacings in the respective Mo layers, indicating that the brittle Mo interlayer dictates deformation of the overlying Al. Only at 10:1, Al can sufficiently plastically deform to prevent TTC formation induced by the brittle interlayer.

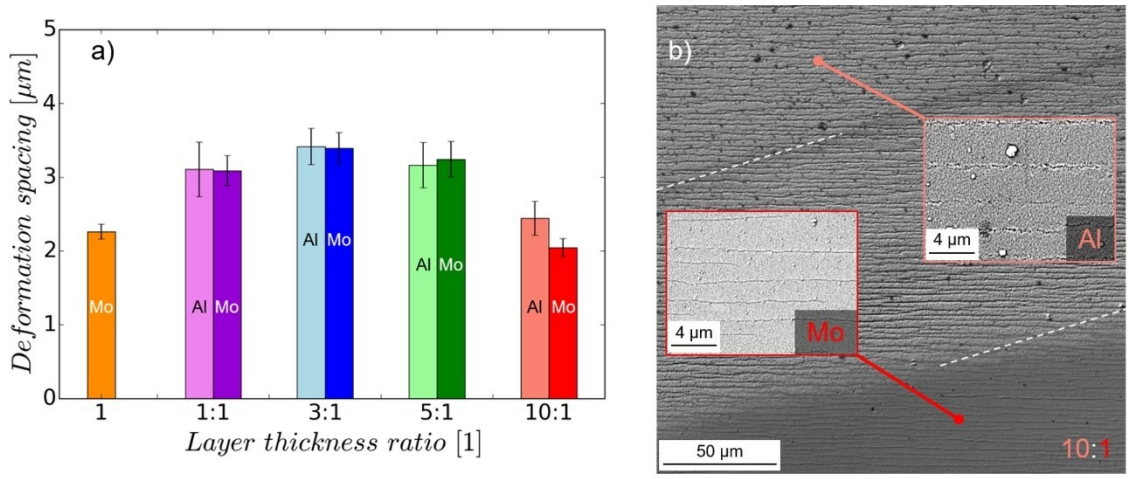

Fig. 4.4 (a) Post mortem saturation deformation spacing analysis at 12% strain of the bilayers obtained from SEM micrographs. Only the thickest bilayer system shows dissimilar deformation spacing for the Al and Mo layers. The highest overall deformation spacing was recorded for Al/Mo 3:1.The exact values are found in Table 4.1. (b) CLSM laser image of a 10:1 etched bilayer with SEM insets. The dashed white lines mark the boundaries of the etched areas. The upper area shows the Al surface and the lower area shows the Mo layer.

SEM micrographs of post mortem FIB milled cross-sections parallel to the straining direction are shown in Fig. 4.5. The bilayer with the lowest thickness ratio (1:1) shows TTCs. The formation of TTCs in the Mo film and the 1:1 bilayer has a direct impact on the conductivity of the films and leads to earlier failure (Fig. 4.5). The bilayers with higher thickness ratios (3:1, 5:1 and 10:1) illustrate cracked Mo layers and necking of the Al surfaces. The bilayer with a 3:1 ratio have a 20% to 25% share in TTCs among the total number of deformations (appraised from several FIB cross-sections). On bilayers with higher thickness ratios at 12% strain, only necks and shallow cracks were observed. Bilayers with thickness ratios of 3:1, 5:1 and 10:1 preserve subsurface pathways, marked by white dashed lines in Fig. 4.5, that are still capable of electron conduction. The fact that even after 12% tensile strain the Al layers with higher thickness ratios are not completely fractured confirms the improved electro-mechanical behavior of these systems. The cross-sections in Fig. 4.5b-d also demonstrate that the cracks in the Mo interlayer and on the Al surface are at the same positions. This was similar to what was

observed by Marx et al. [91] for Cu/Cr bilayers. For higher ratios of Cu/Cr (20:1) a higher number of cracks (lower crack spacing) in the brittle Cr layer was reported [91].

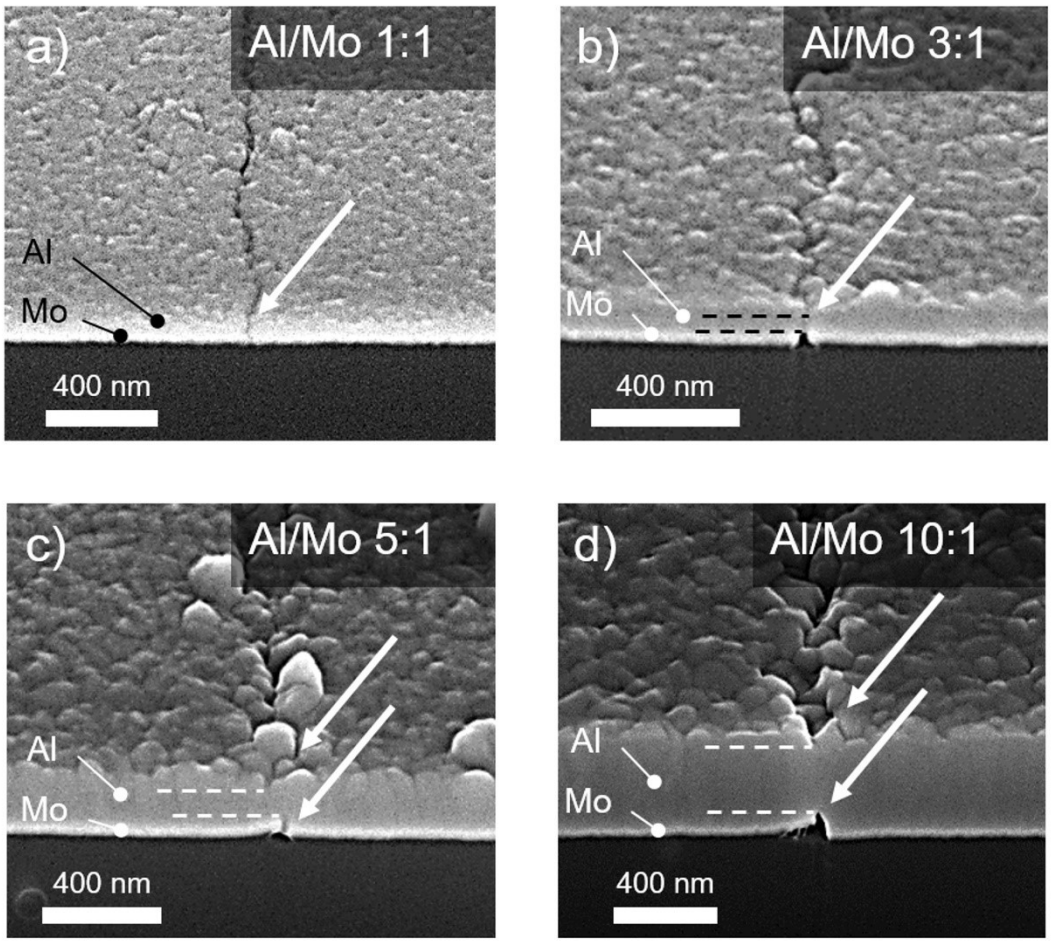

Fig. 4.5 Post mortem FIB cross-sections after a maximum strain of 12%. (a) TTCs in both metal layers, while the Al layers in (b), (c) and (d) only show surface deformation and are still connected and intact in the area between the white dashed lines.

4.4 DISCUSSION

The results of the *in situ* resistance measurements illustrate that increasing the Al layer thickness has a beneficial effect on the electro-mechanical behavior of the Al/Mo bilayers. Thicker ductile layers reduce the influence of the brittle layers and enable the bilayer to achieve a higher COS (Fig. 4.1). The critical thickness ratio of the Al/Mo layers for a maximum strain of 12% to prevent brittle failure induced by the 30 nm Mo interlayer is between the thickness ratios of 5:1 (150 nm Al) and 10:1 (300 nm Al). For 5:1 ratios a COS of 8.8% ± 0.7% was determined and a thickness ratio of 10:1 did not show electrical failure within the tested strain range (max. 12%). In thicker Al layers (≥3:1), the formation of TTCs is prohibited or delayed, leaving Al subsurface pathways

for electrical conduction (Fig. 4.5). The *in situ* resistance measurements show that the COS can be tuned by adjusting the thickness of the ductile Al layer. This allows optimal performance with less material used. The COS values are always higher than the observed DOS values as localized deformation precedes crack formation. It is noted that the DOS is observed within a small range of strain, approximately 2-4% strain, while the COS ranges between strains of 2-9%. The narrow range of DOS is most likely related to the yield strain of the Al film and could be confirmed with future *in situ* XRD measurements [92]. The increased Al thickness helps to increase the electrical COS values and requires more plastic deformation, thus strain, before TTCs form which increases the measured resistance. These results are significant because the microstructure of the Al films is believed to be similar in the nanocrystalline regime and that the observed behavior is more dependent on the Al film thickness.

In situ tensile tests with CLSM showed that surface deformation starts as locally thinned regions (necks), which gradually transform into TTCs with increasing strain. Bilayers with thinner Al layers (thickness ratio 1:1 and 3:1) display TTCs through both metal layers early in the straining process. This is also indirectly observed by the 4PP data (COS) in Table . The COS and DOS for bilayers with thickness ratios of 1:1 and 3:1 are comparatively close and are an indication of brittle fracture. While deformation of the higher thickness ratios (5:1 and 10:1) was observed in CLSM, this is not observed at the same strain in the 4PP data. This can be attributed to the weaker impact of the shallow initial surface deformations on the resistance. An increased Al layer thickness has a stronger impact on electronic conduction than surface necking.

Similar thickness ratios of other material systems are not comparable at this time due to the fact that a similar range of thickness ratios was not studied using similar experiments. For example, similar experiments with the CLSM were not performed on the Cu/Cr system [91] which has different thickness ratios (5:1, 10:1, and 20:1). However, *in situ* XRD experiments were performed and found that the yield stress increases with decreasing film thickness and that the engineering strain at which the yield stress occurs increases with increasing film thickness [91]. This is approximately the DOS for the Cu/Cr system and the behavior is similar to the Al/Mo system. Furthermore, the Au/Cr and Inconel/Ag systems [92,93] with a thickness ratio of 5:1 were characterized with *in situ* CLSM, but due to the total film thickness being less than 200 nm, both film systems failed in a brittle manner with TTCs, thus no DOS could be assessed. This leads to the theory that not only the film thickness ratio is important, but also the total bilayer thickness. When the total bilayer thicknesses are compared for all mentioned systems (Al/Mo, Cu/Cr, Au/Cr, and Inconel/Ag), the best performing

thickness ratios are the 5:1 and 10:1 Al/Mo with total thicknesses of 180 nm and 330 nm, respectively, and the 20:1 Cu/Cr having a total thickness of 210 nm. These results indicate that bilayers should have a thickness ratio of at least 5:1 and a total bilayer thickness near 200 nm in order to avoid brittle fracture of the conductive ductile layer. However, this assessment is by no means a universal result and requires further investigation.

The saturation deformation spacing follows no observable trend with respect to the thickness ratio. The bilayer ratios of all of the films have essentially the same saturation crack or deformation spacing for the Al and Mo layers. Even though a maximum crack spacing can be found on the 3:1 ratio (Fig. 4.4), all of deformation spacing values for the Al and Mo layers should be considered to be similar within the experimental error. During tensile straining, the Mo layer fails first via crack formation and the cracks act as stress concentration points in the normally ductile Al layer. Cracks in the Mo layer correspond directly to deformation and necking the Al films (Fig. 4.5 and Fig. 4.4). This one-to-one relationship between Mo cracks and Al deformation is different to what was observed for the Cu/Cr system [91], where the 20:1 thickness ratio resulted in much smaller and shorter cracks in the Cr layer compared to the sample having a 5:1 thickness ratio. The deformation spacing of the bilayers reaches a plateau at 8% to 10% strain and this value is expected in similar fragmentation tests [113]. The main cracking mechanism for the Al/Mo bilayer system supported by a PI substrate is the brittle fragmentation of Mo that forces the ductile Al layer to deform and leads to cracks initially at the interface and necking on the Al layer surface. During straining deeper necks become cracks in the conductive Al and lead to electrical failure. The importance of the neck depth for electrical conductivity indicates that not only the thickness ratio between ductile and brittle layers is of importance, but also the thickness of the ductile film. Furthermore, since the grain sizes are similar for all Al films, it can be recognized that the effects on the COS, DOS and deformation spacing are independent of the microstructure and can be considered to be pure Al film thickness effects.

4.5 CONCLUSIONS

In situ tensile tests with surface analysis and electrical resistance measurements allowed the observation of the electro-mechanical behavior of a ductile/brittle Al/Mo bilayer system on a flexible PI substrate. An increased thickness of the Al layer (30, 75, 150 and 300 nm) delays electrical failure up to a maximum strain of 12%. Thicker Al layers are left with thicker undamaged subsurface pathways for conduction. A lower thickness

limit for the channels has been found near 150 nm Al layer thickness. Cracks originate in the Mo interlayers and act as stress concentration points in the Al layer, causing deformation and even brittle fracture of the ductile layer. The deformation spacing was found to have no clear relation to the thickness ratio or conductivity. However, TTCs were found to directly impact conductivity. By tuning the thickness of the conductive Al layer, the COS of the bilayer system can be adjusted to the requirements of an application. Conceivable next steps closer to application are cyclic tensile and bending tests of the Al/Mo bilayer systems to analyze, compare and optimize them for different loading conditions.

Chapter 5 was almost identically published by the author of this thesis in [16]. In the current thesis, all superfluous equations were replaced with references to the main text. Furthermore, the figure and reference numbering was adapted to fit the thesis.

5 COMPRESSIVE AND TENSILE BENDING OF SPUTTER DEPOSITED AL/MO BILAYERS

5.1 INTRODUCTION

An increased proliferation of commercially available rollable flexible electronics in everyday life is anticipated for the near future [1]. For realization, today's devices need further improvements to sustain their lifetime and reliability under bending conditions. Critical aspects for rollable electronic devices are the materials and the device architecture, which ensure stable electro-mechanical behavior and long lifetimes. Apt material systems for bending loads with high cycle numbers are yet to be found. Improving and modifying materials that are already in use for rigid electronics are logical next steps for new rollable and foldable applications. Therefore, sputter-deposited Al/Mo bilayers that are similar to the interconnects used in current TFT flat panel display technologies [21,22], were studied here. This material combination is one of the most widely adopted in the TFT industry due to its low electrical resistivity in the range of 3 μΩcm, easy pattern-ability in common wet etchants (e.g. a mixture of phosphoric acid, nitric acid and acetic acid) [32], as well as wide availability and low cost sputtering targets.

5.2 MATERIALS AND EXPERIMENTS

For an appropriate estimation of lifetime and reliability of flexible devices, quick and simple tests emulating real loading conditions are desired. So far no test standard has been developed, but different scientific groups have proposed different concepts for bending tests, some based on beam deflection, others on bending along a radius [131,133,147–151,169–171]. This study utilizes a custom-built device based on bending along a radius, which ensures reproducible characterization, adequate testing time, a defined bending strain, and the option to test several samples simultaneously [86,146]. Aided by *ex situ* electrical 4PP resistance measurements, CLSM, SEM and FIB milling, further insights on the damage evolution are gained. Applying either compressive or tensile bending loads, by simply changing the direction of the bending, will elucidate the

functional limits of the tested material systems in order to design devices with appropriate lifetimes.

The studied material system is a direct current magnetron sputter deposited bilayer system, consisting of an Al layer with thicknesses of 30, 75, and 150 nm in combination with a 30 nm Mo adhesion layer on 50 µm thick transparent polyethylene terephthalate (PET – Melinex 401CW). These layer thicknesses lead to respective Al/Mo thickness ratios of 1:1, 2.5:1 and 5:1. The 2.5:1 bilayer will be referred to as 3:1 bilayer for simplicity. Deposition parameters can be found in ref. [15]. For cyclic bending experiments, a sample geometry of 40 mm × 6 mm was used. Bending tests were performed using the custom-built FLEX-E-TEST [86,146]. The device consists of a wheel with curved grips having a defined bending radius of 2 mm (Fig. 5.1a). Samples were clamped into a grip on one side and, when moved against an anvil, are bent according to the grip's bending radius. Using the relation $\varepsilon = d_s/2r$, where d_s is the substrate thickness and r the bending radius, the respective bending strains, ε, can be estimated. With the used bending radius of 2 mm and a substrate thickness of 50 µm, the applied bending strain is 1.3% for all samples.

Cyclic bending was performed either under tensile strain or compressive strain until 20,000 (20 k) cycles (equals 18 bending cycles per day over three years) were reached using a frequency of 1 Hz. The tests were interrupted after 25, 50, 75, 100, 200, 500, 1 k, 2 k, 5 k, 10 k and 20 k cycles for *ex situ* resistance measurements and CLSM imaging. The electrical resistance was measured with a Keithley 2000 digital multimeter of only the bent area (Fig. 5.1b) (~ 6 mm × 3 mm) by placing the sample between two flat grips connected by two electrical contacts, similar to monotonic tensile testing [88], but without applying any strain. Continued observation of the bent areas of the bilayers with CLSM showed a concentration of the mechanical damage next to the grip for the Al as well as the Mo layer (Fig. 5.1c). In order to obtain a representative measure of the mechanical damage across all samples and applied cycles, an identical area of 640 µm × 640 µm at identical positions on the samples was used to determine the damage density (indicated by the red square in Fig. 5.1c). Damage, including cracks, scratches and any other surface features, were determined from CLSM images using the free software ImageJ [168] and utilizing a line intercept method with three profile lines for manual counting. To separately record the damage of the individual layers, the Al layers were observed from top and the Mo layers were accessed through the transparent PET substrate from the bottom. The final mechanical damage of the Al top layer after 20 k cycles was additionally investigated using SEM and showed good agreement with CLSM images.

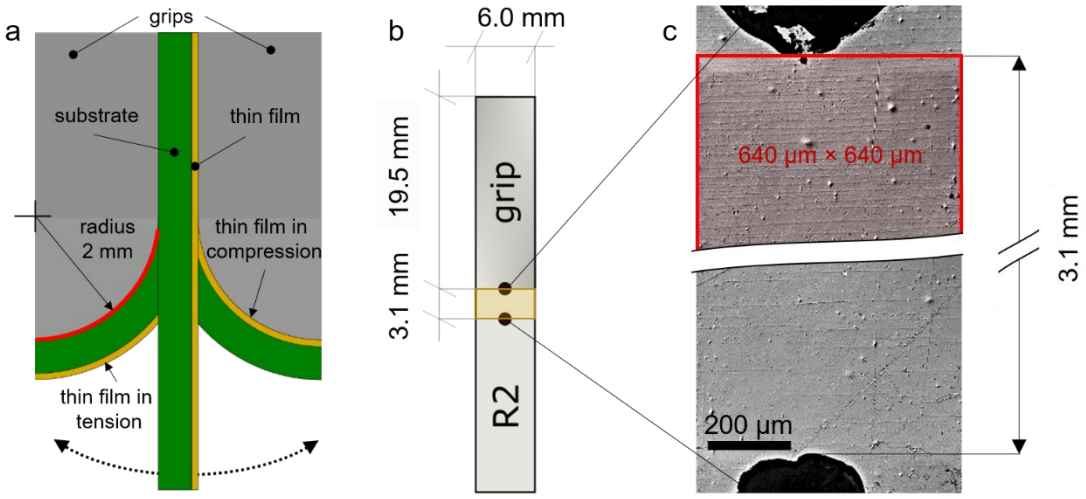

Fig. 5.1 (a) Controlling the direction of sample rotation enables bending under tensile or compressive strain. (b) Sketch of the sample with the rectangle marking the bent area between the dots. (c) The stitched CLSM image displays the concentration of cracks closer to the grip area. The image was taken from a 3:1 bilayer under tensile bending load after 20k cycles. The top area marked in red (640 µm × 640 µm) near the grip has the highest damage concentration and was used to evaluate the damage for all samples.

5.3 RESULTS AND DISCUSSION

Under cyclic tensile bending strain, a relation between bilayer thickness and damage was observed (Fig. 5.2a, b). Thicker Al layers promote less damage formation in the form of fatigue cracks. The thickness ratio influences the total amount of damage as well as the rate of damage formation. In the 1:1 bilayer, TTCs form after only 25 cycles and from there on the damage density increases at a slower rate, leading to the highest damage density. The 3:1 and 5:1 bilayers do not show such an abrupt damage density increase from the start, but show faster damage accumulation at higher cycle numbers. A comparison of the damage in the Mo layer (Fig. 5.2a) and the Al layer (Fig. 5.2b) illustrates that cracks and/or damage start simultaneously in both layers and continues forming at similar rates (Mo vs. Al) with increasing cycles. Only, the number of cracks in the respective layers vary slightly, most likely due to the difficulties imaging through the PET substrates. Note that the initial damage density values include scratches found in the substrate. In the 1:1 bilayer the Mo layer contains more damage than the other bilayer systems.

The same samples show a different behavior under compressive bending strain (Fig. 5.2c, d), having lower damage densities compared to tensile bending. After 20 k cycles the 1:1 bilayer has approximately 40% less cracks under compressive bending compared to tensile. The 3:1 and 5:1 bilayers have a roughly 10 times lower damage

density under compressive bending compared to the 1:1 bilayer. All bilayers exhibit a similar amount of damage after 20 k cycles for both of their respective Mo and Al layers when compressive bending is applied. The damage density in the Mo layer of the 1:1 bilayer (Fig. 5.2c) increases more gradually than the Al layer surface (Fig. 5.2d), which suddenly rises after 25 cycles. Both layers form cracks immediately and end up with a similar amount of damage, but the brittle Mo layer demonstrates a retarded initial damage increase compared to the Al layer. This could again possibly be attributed to physical limitations of the CLSM when measuring through a polymer substrate or indicates a preferred crack initiation in the Al layer for compressive bending. The two thicker bilayers show no pronounced changes in the damage density under compressive loading in comparison to tensile loading. The Al layers display almost identical damage density for 3:1 and 5:1 bilayers (Fig. 5.2d). With the current experimental setup, the crack initiation layer could not be confidently identified.

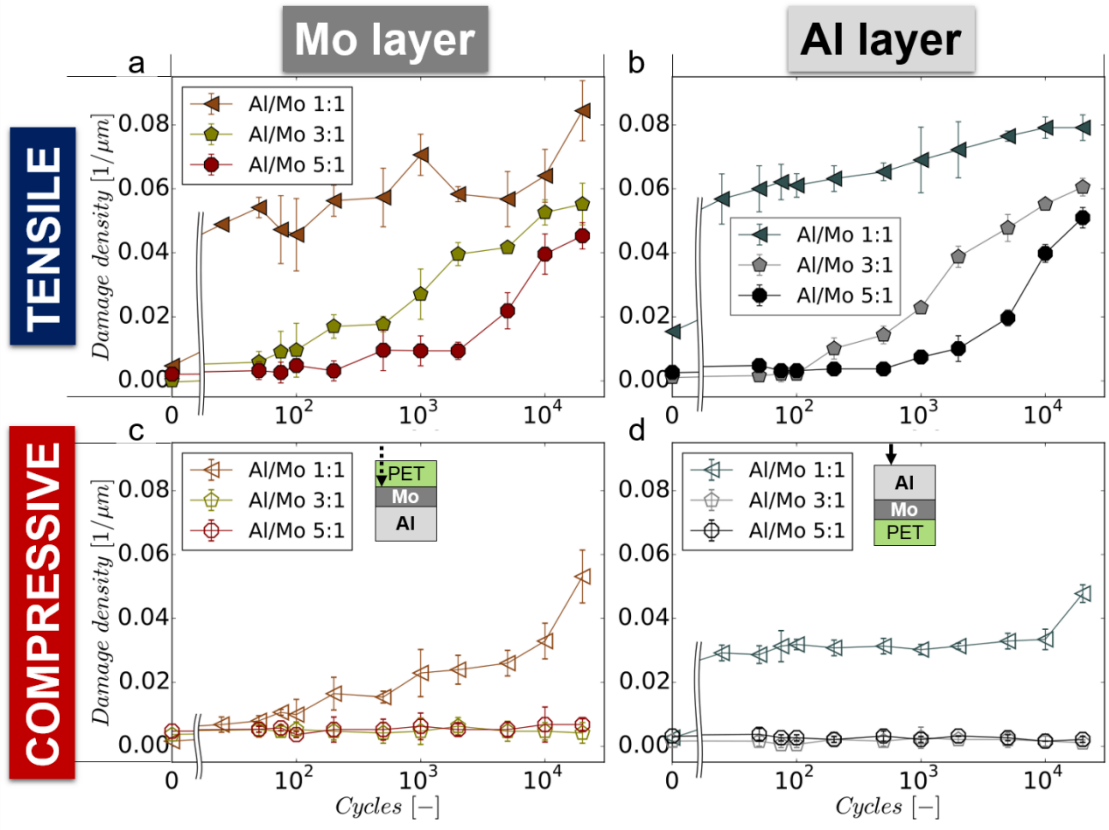

Fig. 5.2 Evolution of damage density over cycle number at 1.3% bending strain. For a better overview the damage density is linear and the number of cycles is logarithmic. The lines only guide the eye and have no mathematical meaning.

Closer inspection of CLSM images illustrate that upon formation of shorter cracks perpendicular to the bending direction, the cracks quickly grow in length until they are hindered by other defects, such as droplets, voids, scratches and other cracks. The

following conclusions could be drawn from surface damage evolution during cyclic bending: (i) thicker Al layers are less prone to crack formation, (ii) most cracks are TTCs, which is substantiated by similar damage densities in both the Mo and Al layers, and (iii) tensile bending induces more damage compared to compressive bending. For example, during tensile bending the thicker Al layers have lower damage densities than the 1:1 (bilayers: 1:1 0.08 μm^{-1}, 3:1 0.06 μm^{-1} and 5:1 0.05 μm^{-1}) and during compressive bending the 1:1 bilayer has 0.05 μm^{-1}, while the 3:1 and 5:1 bilayers show almost no damage (Fig. 5.2). This disparity is caused due to compressive bending pushing crack faces together (less destructive), while tensile bending will pull the crack faces apart and increase damage with each cycle.

The formation of cracks in the bent area indicates immediate electrical failure of the 1:1 bilayer, as is illustrated by the rapid increase of the measured electrical resistance (Fig. 5.3a, b). Due to the relative small initial resistance values measured for the three bilayer thickness ratios 1:1, 3:1 and 5:1 (2.2 Ω, 0.8 Ω, and 0.3 Ω, respectively), the measured resistance displays the individual differences better than R/R_0 or $\Delta R/R_0$ (Fig. 5.3). The resistance curves in Fig. 5.3 for tensile and compressive bending show that the resistance increases for the bilayers with 1:1 ratio immediately upon cyclic bending (note the logarithmic x-axis). Tensile bending produces a larger increase in resistance than compressive bending in the bilayers and results in resistance values, which are an order of a magnitude higher (Fig. 5.3a). The stronger resistance increase for tensile bending is also reflected in greater damage density compared to compressive bending. The thicker bilayers (3:1 and 5:1) yield, in general, lower initial resistance values and show less electrical sensitivity under bending. Apart from the 1:1 bilayer, which shows the highest resistance increase, the resistance of the 3:1 bilayer under tensile bending increases tenfold after 20k cycles. Under compressive bending (Fig. 5.3b), the 3:1 bilayer shows no significant changes, similar to the 5:1 bilayer under either bending direction. The thicker Al layers (3:1 and 5:1 bilayers) display better electrical conductivity because the increased Al layer thickness better accommodates the resulting damage caused by the bending before channel cracks occur. Conductive areas were maintained for thicker Al layers after the formation of cracks, necks and extrusions. Also, similar to other ductile/brittle thin film systems (Au/Cr, Cu/Cr and Inconel/Ag) [92,93,172] during uniaxial tests, an increasing ductile Al layer thickness was also found to confine the brittle nature of the Mo adhesion layer for the whole bilayer and reduce damage density during bending tests.

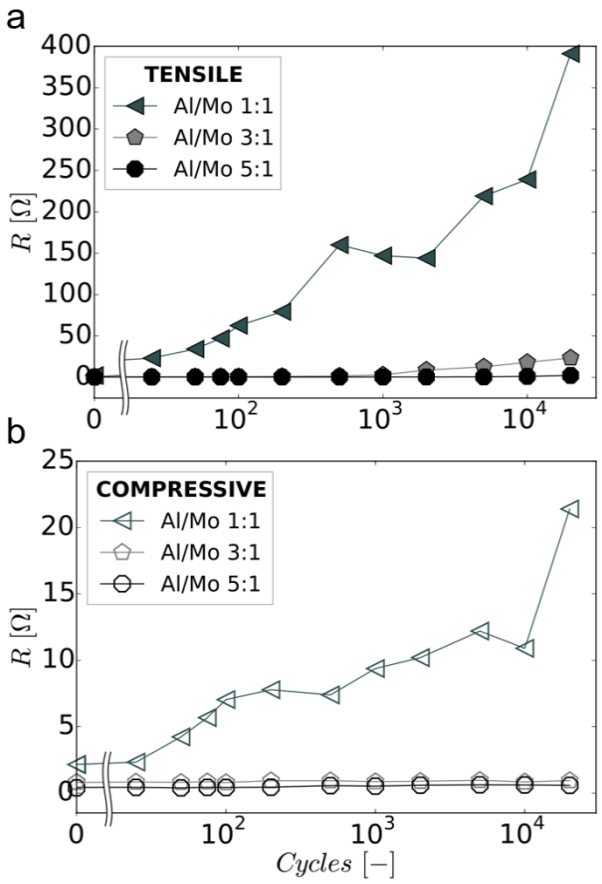

Fig. 5.3 Measured electrical resistance within the bent area (a) under tensile bending and (b) compressive bending. The lines act as guides for the eye and have no mathematical meaning.

As previously addressed, repeated bending induces damage in the form of TTCs. Fig. 5.4 illustrates that the crack openings decrease with thicker bilayers and allow bridging between crack fronts, enabling current flow. A comparison of several FIB-cuts reveal a less frequent occurrence of TTCs for thicker bilayers. Other surface defects like grain boundary cracks or twins found in Cu films of similar thickness and bent under high cycle fatigue conditions [133] were not observed with SEM or CLSM before or after bending. However, extrusions and cracks along grain boundaries could be detected on 5:1 bilayers, similar to Cu samples of comparable thicknesses [170,173]. According to Essmann et al. [174], the heights of extrusions are limited by grain size. The observed extrusions on the 5:1 bilayer (Fig. 5.4c) were very small compared to their film thicknesses, indicating nano-sized grains in the range of the respective film thicknesses (30 nm, 75 nm and 150 nm). Hence, the influence of the grain size on the electro-mechanical behavior of these bilayers is considered to be negligible. If the grain size of the Al films were larger, then different electro-mechanical behavior would be expected,

as demonstrated by cyclic uniaxial tensile straining on Cu [175] and thermally cycled Al thin films [176].

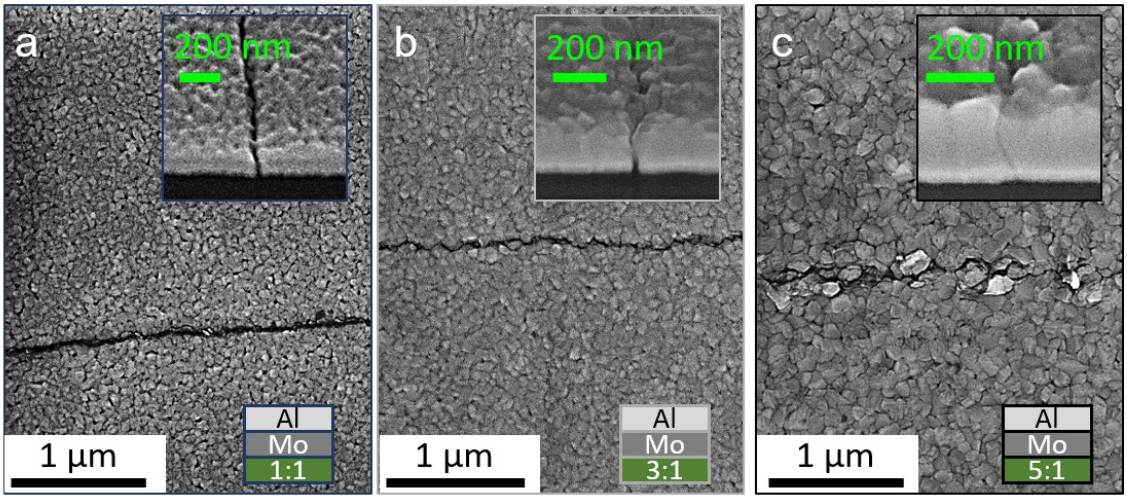

Fig. 5.4 Comparison of SEM images of the bilayers under tensile loading after 20 k cycles. The insets in (a), (b) and (c) show FIB cross sections of the respective bilayer.

As expected, cyclic bending leads to a loss in electrical conductivity due to the accumulation of TTCs in the studied Al/Mo bilayer system on flexible substrates. Especially bending with a tensile load yields higher resistance values and more mechanical damage compared to compressive bending after 20k cycles. In contrast to Cu and printed Ag films [86,177], no strain induced grain growth due to cyclic tensile loads could be observed for Al/Mo bilayers when comparing SEM images before and after bending. A lack of visible ductility and plasticity with decreasing Al layer thickness can be attributed to the dominance of the brittle interlayer (Mo), which was confirmed for Cu/Cr and Al/Mo bilayers under uniaxial tensile strain [15,91]. Comparing the Al and Mo layers of the tested samples reveal comparable damaging behavior at similar rates under bending, independent of the bending load. Since damage in the individual layers is usually found at the same position and no crack deflection into the interface is visible in the FIB-cuts, a strong adhesion between both metal layers can be concluded. The influence of different bending modes has already been discussed in literature [86], where it was demonstrated that the negative impact on damage density by the type of bending load is in general ranked as mixed > tensile > compressive for printed and evaporated Ag films. The tensile > compressive trend for surface damage is in agreement with this work and could also be extended for the electrical conductivity of Al/Mo bilayers. A comparison of the same Al/Mo bilayers that were investigated in this study, but on polyimide substrates, under uniaxial tensile strain reveals the differences between bending and uniaxial tensile tests. Under the previously reported maximum

uniaxial tensile strain of 12%, the 1:1, 3:1 and 5:1, bilayers showed saturation crack densities of approximately 0.3 μm^{-1} each [15], compared to a maximum of 0.08 μm^{-1} for 1:1 bilayers, as investigated within this study (Fig. 5.2). While uniaxial tensile tests can quickly reach the limits of thin films at high engineering strains, no quantitative predictions for cyclic flexible applications can be made. Similar conclusions such as the positive effect of thicker Al layers for the electrical resistance under load can be found for uniaxial tensile [15] and bending tests, but still, the results from uniaxial straining cannot substitute the results from bending tests. These findings are substantiated with earlier bending and uniaxial tensile experiments on printed Ag lines [146]. Similar to uniaxial tensile tests [15], increasing the Al layer thickness improves the measured electrical conductivity of the bilayer and a low resistance can be maintained for more bending cycles. It has also been shown that bending fatigue cracks occur at lower bending strains (1.3%), when compared to the crack onset strains of uniaxial tensile tests (1:1 2.1%, 3:1 3.6% and 5:1 8.8%) [15].

5.4 CONCLUSIONS

The results obtained show that the requirements imposed on rollable flexible devices under compressive bending are best fulfilled for the tested Al/Mo system. A foldable device with an extremely long lifetime is possible as long as folding is only applied under compressive bending with a bending strain ≤1.3%, corresponding to a bending radius of 2 mm and a substrate thickness of 50 µm. Film thickness ratios greater than 3:1 will have less mechanical damage accumulation and a smaller impact on the electrical properties than thinner Al/Mo bilayer ratios. This is because the thicker Al layer can accommodate more plastic deformation before TTCs form and cause the resistance to increase.

Chapter 6 was almost identically published by the author of this thesis in [17]. In the current thesis, all superfluous equations were replaced with references to the main text. Furthermore, the figure and reference numbering was adapted to fit the thesis.

6 CORRELATION OF MECHANICAL DAMAGE AND ELECTRICAL BEHAVIOR OF AL/MO BILAYERS SUBJECTED TO BENDING

6.1 INTRODUCTION

For TFT based display technologies, the next development challenges aside from larger screens with higher resolutions are flexible organic light emitting diode displays [157,178]. Their mechanical flexibility will merge well with our day to day lives in the form of wearable electronics, medical sensors, entertainment and communication devices [1]. Curved and bendable displays are already available, but either their radii of curvature are nowhere near the desired level below 1 to 3 mm for portable flexible displays or their reliability (e.g. number of bending cycles) is insufficient. The current main concern with bendable displays is that smaller radii lead to early failure of the displays upon repeated folding. The cyclic bending loads can cause various types of damage in the circuitry of a display compound [179]. A possible countermeasure against this mechanical damage represents the structuring of rigid islands on a flexible matrix [39]. This way, the electronic components are better preserved. Nevertheless, thin metallizations connect these rigid islands and will have to bear the applied mechanical loads in order to maintain their function. One of the most widely used metallizations for source/drain electrodes in TFT flat panel displays are Mo/Al/Mo interconnections [21,22]. They have low resistivity in the range of 3 μΩcm, are easy to pattern and widely available [32].

For future flexible TFT-displays bending fatigue will be one of the main factors for failure. Currently, no standardized tests for bending loads have been developed. Different research groups have proposed various concepts for bending tests, some based on bending along a defined radius, bending without a defined radius, four-point bending and micro-beam bending [131,133,147–153]. For this study a testing apparatus based on the concept of bending along a radius was chosen [86]. It allows testing of multiple samples at the same time as well as intermittent evaluation of mechanical damage and electrical behavior necessary to understand bending failure. This study further investigates the bending reliability of a simplified Al/Mo bilayer system [16] on top of a flexible PI substrate and provides correlation of the mechanical damage and the

electrical behavior. This helps to determine lifetimes and reliable design criteria for future flexible and bendable devices.

6.2 EXPERIMENTAL METHODS

The studied bilayer system consists from top to bottom of an Al layer (30, 75 and 150 nm), a Mo adhesion layer (30 nm) and a 125 µm thick PI substrate (UBE Upilex-125S). The different thicknesses of the Al layer lead to Al/Mo bilayer thickness ratios of 1:1, 2.5:1 and 5:1. For simplicity the 2.5:1 ratio will be referred to as 3:1 bilayer. All bilayers were grown at room temperature by dc magnetron sputter deposition on 50 mm × 50 mm PI substrates. Prior to deposition the substrates were plasma cleaned for 2 min at an Ar pressure of 1 Pa with an asymmetrically bipolar pulsed dc plasma of -350 V and 50 kHz. Deposition was performed with a laboratory scale dc magnetron sputter system. The targets, powder metallurgically prepared Mo (99.97% purity, Ø 50.8 mm, provided by Plansee SE) and Al (99.99% purity, Ø 50.8 mm, provided by J. Lesker) were mounted on two unbalanced AJA A320-XP magnetrons. The PI substrates with 50 mm × 50 mm size were fixed with Kapton tape on a rotatable sample holder at a distance of 40 mm. The base pressure in the deposition chamber before each deposition run was 1×10^{-3} Pa. Deposition was performed at constant Ar pressure of 0.5 Pa using 156 W for Mo and 166 W for Al, yielding deposition rates of 35 nm/min for both metals. The deposition parameters are identical to previous works [15,16]. After deposition the bilayers were cut in 40 mm × 6 mm strips for the bending tests.

The bending tests were performed with the custom-built FLEX-E-TEST [16,86,146]. In this testing device samples are clamped into metal grips, as shown in Fig. 6.1. The radius, *r*, of the metal grips can be chosen to be 10, 5 or 2 mm. The bending strain, ε_b, is estimated from $\varepsilon_b = d_s/(2r)$, where d_s is the substrate thickness. The equation disregards the bilayer thickness, due to its negligible effect on the bending strain. Bending the samples along the radius of the grip leads to respective bending strains of 0.6% (r10), 1.3% (r5) and 3.1% (r2). The grips are mounted on a wheel, rotating at a frequency adjusted to 1 Hz in the current study. During the movement of the wheel, the grips pass an anvil, as sketched out in Fig. 6.1, causing the bilayer to conform to the radius of the grip. This means while the interval between bending processes for each independent sample is one second, the bending of the whole sample set happens in a fraction of that time and can be considered fast compared to similar bending tests [131,147–152]. Depending on the turning direction of the wheel and the orientation of the sample, the bilayers experience either tensile or compressive stresses. Alternating

the bending direction after 10 cycles combines compressive and tensile bending into a mixed bending. One or two Al/Mo bilayer samples were tested per thickness ratio (1:1, 3:1 and 5:1) and for each bending strain (0.6, 1.3 and 3.1%), leading to (3 × 3) 9 parameter configurations. The tests were performed until a final cycle number of 20,000 (20 k, equal to 18 cycles per day over three years) was reached. Intermittent measurements of the surface damage were carried out with CLSM and the electrical resistance of the relaxed (flat) samples were measured with a Keithley 2000 digital multimeter similar to ref. [16] after 0, 100, 500, 1 k, 5 k, 10 k and 20 k cycles were reached. After each defined number of cycles, the whole length of the bent area of the respective sample was imaged with CLSM to obtain comprehensive information of the damage caused by bending. The electrical resistance was determined by a manual 4-point probe method measurement using two spring contacts with rounded tips and a diameter of 0.5 mm (MISUMI NP20-B). The procedure was repeated four times at the border between the bent and unbent area (orange rectangle in Fig. 6.1 and 6.2) and the results averaged. The spring contacts were connected to a digital multimeter with one pair of contacts for current and the other pair for contact potential.

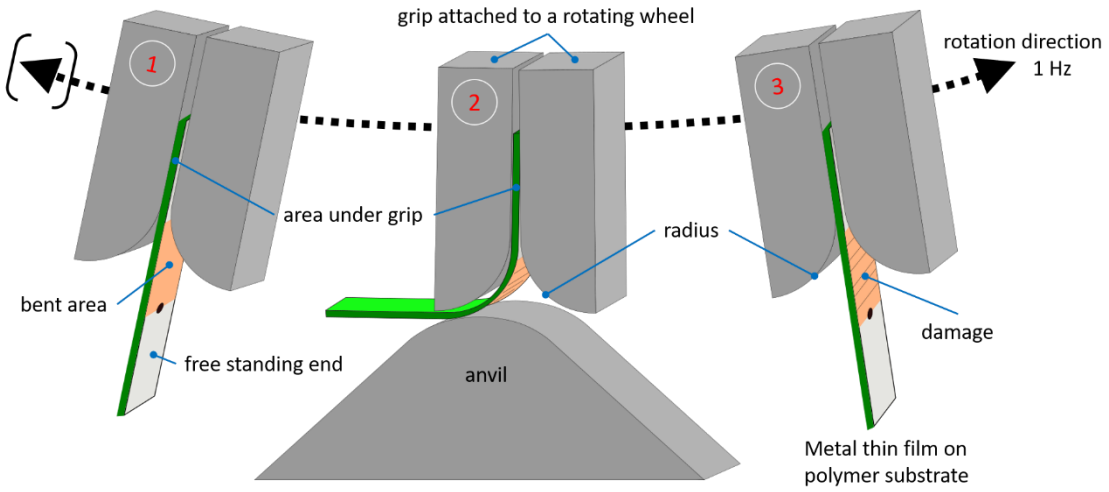

Fig. 6.1 Sketch of the working principle of the FLEX-E-TEST. The sample bends according to the radius of the grip when the anvil is reached. The grips are attached to a wheel that changes its rotation direction every 10 cycles.

The lengths of the bent areas correspond to a quarter of a circle of the matching radius. This means for radii of 10 mm (0.6%), 5 mm (1.3%) and 2 mm (3.1%) the bent areas have respective lengths, L_0, of 14.5, 7.5 and 3.1 mm and a width of 6 mm, corresponding to the sample width (Fig. 6.2a-d). Evaluation of the bent surface areas with CLSM revealed inhomogeneous damage distributions with an increasing number of bending cycles for 0.6% and 1.3% bending strains (Fig. 6.2c). Images at 0.6% and 1.3% bending strains indicated that in both cases the highest damage densities were found at

30% of the length L_0 of the bent area, starting from the end of the grip. The corrected areas for these two strains are 640 µm × 640 µm in size (Fig. 6.2a-c). Samples bent with 3.1% strain did not show inhomogeneous damage distribution after 10 k bending cycles and the damage was evaluated over the whole length of the bent area. This way, the worst-case scenario for surface damage was quantified, however, it is only a localized measurement. Damage, such as cracks and scratches, were analyzed using a line intercept method using three profiles to extract the damage density from the CLSM images. The surface damage was quantified using the free software ImageJ and Gwyddion [168,180].The resistance of the bilayers was measured over the whole length of the bent area (L_0), regardless of the inhomogeneous damage distribution, representing a global measurement.

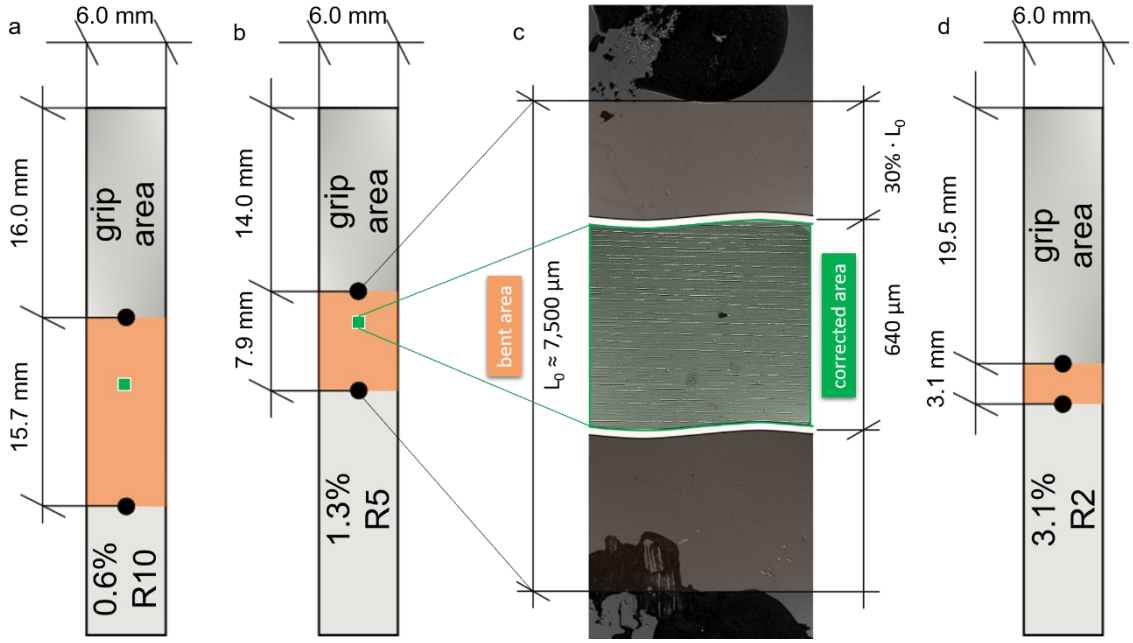

Fig. 6.2 (a), (b) and (d) illustrate the different areas of the 40 mm × 6 mm sample geometry. The upper part is held by the grip, the lower part is free and functions as lever to initialize the bending. The orange rectangle marks the area bent according to the radius of the grip (0.6, 1.3 and 3.1% bending strains, respectively). In (c) a stitched CLSM image of the bent area at 1.3% bending strain illustrates an inhomogeneous damage distribution. The inhomogeneity was accommodated by evaluation of a defined corrected area, where surface damage is the highest. At 30% of the gauge length L0, an area of 640 µm × 640 µm (green squares) was evaluated to determine surface damage. At higher bending strains of 3.1%, no gradient of the surface damage distribution was observed and therefore no corrected area applied.

Additional SEM images of the bilayers before and after 20 k bending cycles were made. FIB cross-sections of the bilayers at the end of the bending tests were performed to elucidate the damage for different bilayer thickness ratios at different bending strains.

6.3 RESULTS

On the surfaces of the as-deposited bilayers different features can be found, such as cracks, scratches, voids, and nodules [181]. The surface characteristics that were evaluated before and during testing consisted of damage that accumulates with an increasing number of bending cycles, such as cracks from bilayer fracture and scratches originating from the PI substrate or from repeated mounting, with both having a strong influence on the electrical conductivity of the bilayers. It should be noted that the scratches, originating either from the substrate or repeated mounting, are few in numbers and only make a small contribution to the total damage at the end of the bending tests. The cracks observed on all bilayers are straight through-thickness cracks (Chapter 5) [16]. Different bilayer thickness ratios and different bending strains lead to varying amounts of accumulated damage after 20 k cycles of mixed bending. This is displayed in Fig. 6.3, and quantified by the damage densities included in the respective images. The values for damage density showed a good match with SEM images obtained after the tests. Most of the damage consists of cracks with a few scratches. Note that a part of the accounted surface damage includes very fine cracks that are only distinguishable at full resolution of the original CLSM images. The more pronounced cracks are more recognizable because they are accompanied by extrusions and lead to better contrast in the CLSM. At a bending strain of 0.6% there is hardly any damage observed. At 1.3% and 3.1% there is a clear increase of damage for all thickness ratios. Generally, the measured damage densities increase for larger applied bending strains and thickness ratios, however, the 3:1 ratio tends to have the lower damage density out of all three bending strains.

Close examination of the intermittent CLSM images revealed that the damage starts as short cracks, as observed earlier for only compressive or only tensile bending of Al/Mo bilayers (Chapter 5) [16] and shown in Fig. 6.4. With increasing bending cycles, the number of cracks and the crack lengths increase. In Fig. 6.4 a bilayer at a bending strain of 3.1%, which was mentioned before to have a homogeneous damage distribution after 10 k bending cycles, is presented. There, cracks and extrusions grow earlier near the grip, which is represented by the upper row of Fig. 6.4 in comparison to the lower row, which is closer to the free end of the sample. Only after crack growth eventually reaches saturation around 10 k bending cycles, the damage density at 3.1% bending strain is evenly distributed along the bent area. At this point only extrusions are found more often closer to the grips, because larger stresses are near the grip.

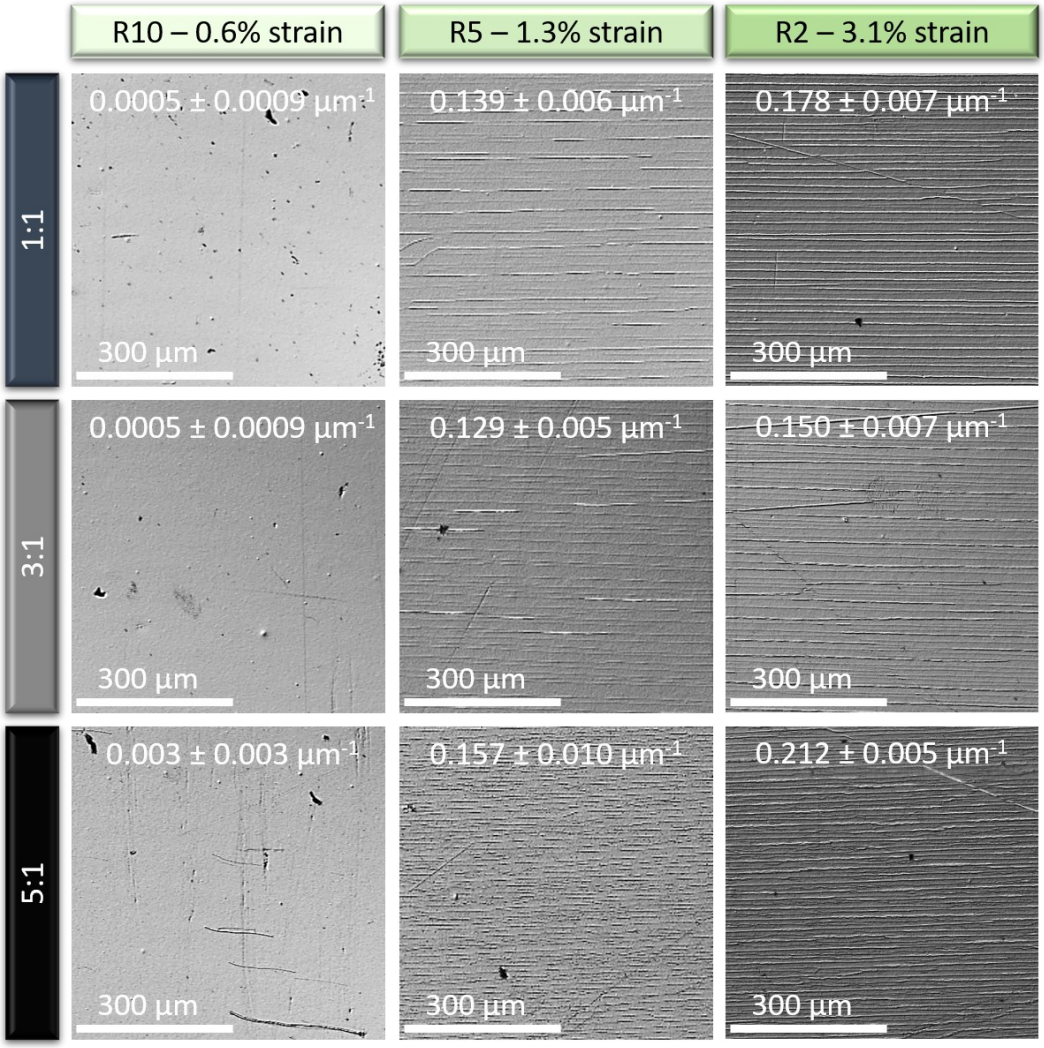

Fig. 6.3 Matrix of CLSM images with the areas of highest damage density for all bilayer thickness ratios and applied bending strains after 20 k bending cycles. The linear damage densities are given at the top of each image.

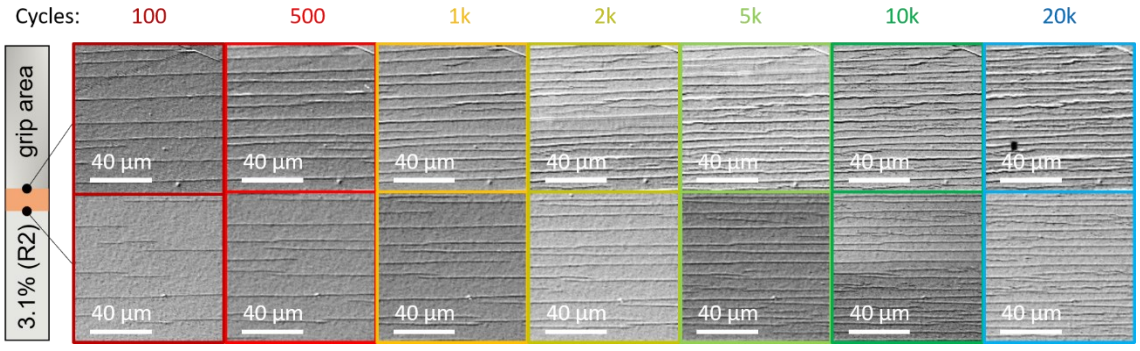

Fig. 6.4 CLSM images of the surface damage within the bent area at different cycle numbers. The images are from the 5:1 bilayer under a bending strain of 3.1%. The first row denotes the area closer to the grip, where cracks and extrusions start earlier. The second row shows an area at extended distances from the grip. At 10 k cycles the cracks are evenly distributed (saturation).

The use of intermittent bending allowed to gain quantitative evidence that higher bending strains cause more surface damage and lead to a significant increase of the electrical resistance (Fig. 6.5). The graphs in the first row of Fig. 6.5 illustrate that upon cyclic bending, there is practically no damage with 0.6% bending strain even after 20 k cycles. At 1.3% and 3.1% bending strains, the formation of damage increases quickly within the first 1 k bending cycles. Only the 1:1 bilayer at ε_b = 1.3% had delayed damage formation to 5 k bending cycles, with the surface damage saturating at higher cycles (10k-20k). The delay of the 1:1 bilayer in Fig. 6.5b is caused by very fine cracks, which were only clearly visible upon reaching 5 k cycles. It can be assumed that crack nucleation and growth is similar to the 3:1 and 5:1 bilayers in Fig. 6.5b. For each bilayer thickness ratio, the total amount of surface damage after 20 k cycles increases with the applied bending strain. A commonality of the bilayers at 20 k cycles is that among the three thickness ratios and bending strains, the 5:1 bilayer has the most damage followed by the 1:1 and then the 3:1. This outcome has not been resolved yet and will be not further discussed in this manuscript. The corresponding relative electrical resistance, which is measured when dismounted (unstrained state), generally yields higher values at higher bending strains analogous to the surface damage (Fig. 6.5), however, individual bilayer thickness ratios behave differently. Thicker bilayers yield lower relative resistance values R/R_0 during bending as well as lower initial resistance values R_0 (Appendix A). The relative resistance for 1.3% and 3.1% bending strain also displays a strong increase during the first 100 cycles, but does not necessarily reach saturation when the measured surface damage reaches a plateau. At 0.6% bending strain the change in resistance is relatively small, which corresponds to the predominant absence of surface damage (Fig. 6.5a,d). The elevated R/R_0 value at 5 k cycles for the 1:1 bilayer in Fig. 6.5d at 0.6% bending strain was caused by a single outlier and demonstrates the sensitivity of the spring contacts regarding surface conditions.

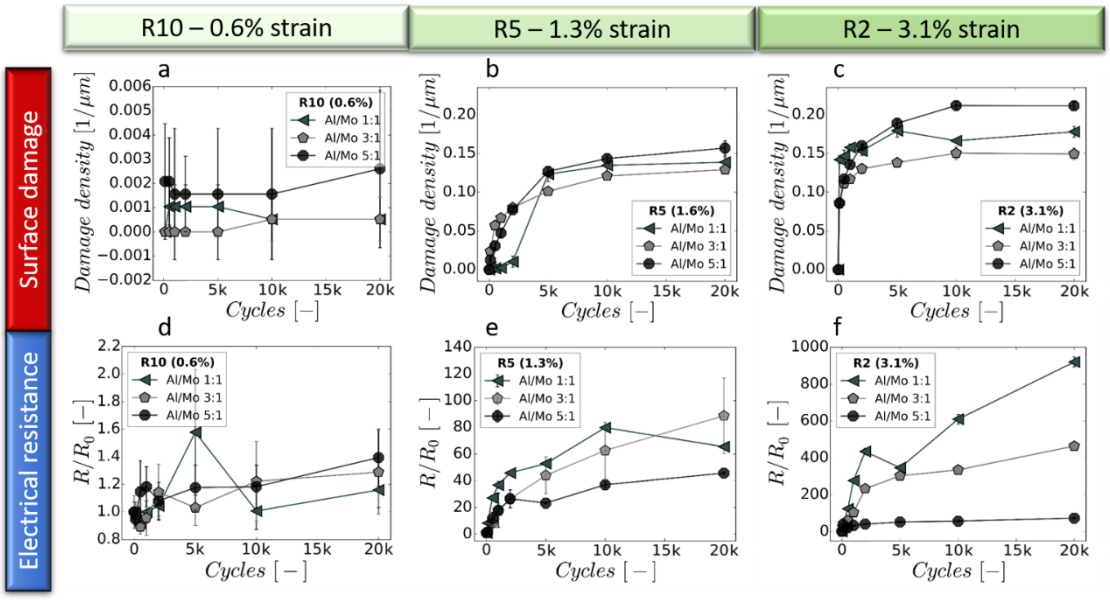

Fig. 6.5 Quantification of the electro-mechanical behavior during bending. (a-c) Evolution of the surface damage density as a function of the cycle number within the corrected areas (a-b) and the whole bent area (c). (d-f) The relative resistance changes in the unstrained state with increasing cycle numbers within the whole bent area.

6.4 DISCUSSION

6.4.1 RELATIONSHIP BETWEEN SURFACE DAMAGE AND RESISTANCE

There are two principle crack formation mechanisms: (a) cracks form due to the stress introduced by the bending strain or (b) from cyclic loading. The deformation onset strains of the Al/Mo bilayers are known from uniaxial tensile tests [15], where surface deformations in the form of necks were observed for the 1:1, 3:1 and 5:1 bilayers at 2.0, 2.5 and 2.8% engineering strains, respectively. Therefore, at the lower bending strains (0.6% and 1.3%) cracks most likely form through the accumulation of damage from cyclic bending. In the case of ε_b = 3.1%, damage is expected to form after the first bending cycle because the applied bending strain is higher than the deformation onset strain. The cross-sections of the bilayers after 20 k cycles in Fig. 6.6 show that nearly all cracks are TTCs. However, these micrographs after 20 k cycles are not necessary evidence that the cracks are TTCs from the beginning. Results from our previous work [16] (Chapter 5) with the same type of bilayers on a transparent PET substrate for similar bending conditions demonstrated that the cracks formed at the start of the bending experiments

are likely TTCs. Assuming this to be the case here as well, the crack depth should not affect the resistance.

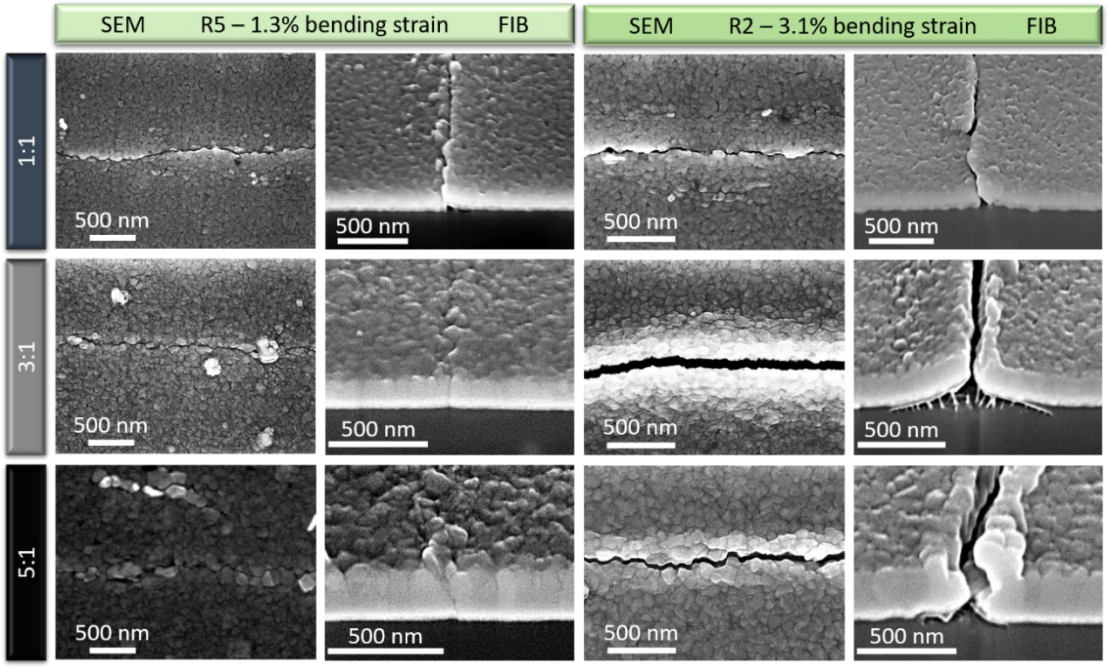

Fig. 6.6 The columns entitled "SEM" show typical cracks from the top surface and the columns entitled with "FIB" show cross-sections (not same crack) formed after 20 k cycles of mixed bending for 1.3% and 3.1% bending strain.

The electro-mechanical evaluation of cyclically bent and monotonic uniaxial tensile strained [15] Al/Mo bilayers demonstrates that tensile tests cannot substitute bending tests to quantify their long term reliability under realistic conditions. The saturation crack densities for monotonic uniaxial tensile strained Al/Mo bilayers at 12% engineering strain studied in [15] are between 0.29 μm^{-1} (3:1 bilayer) and 0.33 μm^{-1} (1:1 bilayer). In the current study, at 0.6% bending strain the saturation crack densities at 20 k bending cycles are below 0.003 μm^{-1}. For 1.3% bending strain the saturation crack densities are between 0.13 μm^{-1} (3:1 bilayer) and 0.16 μm^{-1} (5:1 bilayer). The highest saturation crack densities for cyclic mixed bending in the current study are recorded for 3.1% bending strain and range between 0.15 μm^{-1} (3:1 bilayer) and 0.21 μm^{-1} (5:1 bilayer). This illustrates that when crack/damage saturation density is reached, monotonic uniaxial tensile straining causes more damage than cyclic bending. For 3.0% engineering strain the bilayers under monotonic uniaxial tensile load range between 0.10 and 0.14 μm^{-1} [15], showing that under comparable strains, cyclic loads cause more damage. Because the large difference between the damage density in saturation and at comparable strains, observed for the monotonic uniaxial tensile strains [15] and cyclic bending, the same mechanical failure criteria should not be applied. A monotonic

uniaxial tensile test does not provide accurate information about when the same system cyclically bent will fail.

At the applied bending strains, the relative electrical resistance of the 1:1 and 3:1 bilayers display stronger changes than the 5:1 bilayer. Generally, the electrical resistance of the bilayers bent with 1.3% and 3.1% increases with the number of bending cycles without reaching saturation (Fig. 6.5e,f). This means that while the surface damage in the form of TTCs and the resistance are related to each other, their relationship is not simple. One cause for the continued resistance increase is the non-uniform deformation due to the applied bending and is especially important for the 0.6% and 1.3% bending strains. Recall that the mechanical damage is only evaluated at the point of highest damage, while the rest of the bent area is neglected by this local measurement. On the other hand, the electrical resistance is evaluated across the whole bent area for a global measurement. With continued cycling, cracks can still form and propagate in the lower region of the bent area, thus causing the resistance to continue to increase even when the observed mechanical damage density saturates.

The non-uniform damage area only accounts for the 0.6% and 1.3% bending strains. The 5:1 bilayer cycled at 3.1% (Fig. 6.4) only has non-uniform damage until 10 k cycles, but still the resistance increases after the mechanical damage density saturates and the surface damage is evenly distributed (Fig. 6.5). For this bending strain, assuming that the resistance changes mainly due to cracks, the following factors can be considered: crack depth, crack density, and crack length. The influence of the crack depth can already be neglected since it is known that all cracks are TTCs (see Fig. 6.6). This leaves the influence of the crack density and the crack length. From Fig. 6.4, it is observed that at the beginning of the bending experiments new short cracks (and scratches) form quickly and rapidly grow in length (Fig. 6.4, 100-2 k cycles). Once a certain damage density is reached, new cracks propagate slower until finally reaching their maximum length. At this point the surface damage saturates (Fig. 6.5c) and the number of cracks in the measured area practically does not change, which yields the results in Fig. 6.4. However, the resolution provided by CLSM is not high enough to detect if the observed cracks are a single long crack or if several smaller cracks create the illusion of one long crack. After 20 k cycles the samples were examined with SEM and several shorter cracks were observed (Fig. 6.7). This indicates that the long cracks observed in the CLSM may actually be composed of several smaller cracks with conductive bridges in between. With continued bending these shorter cracks will eventually connect and increase the resistance by increasing the pathways for electron flow.

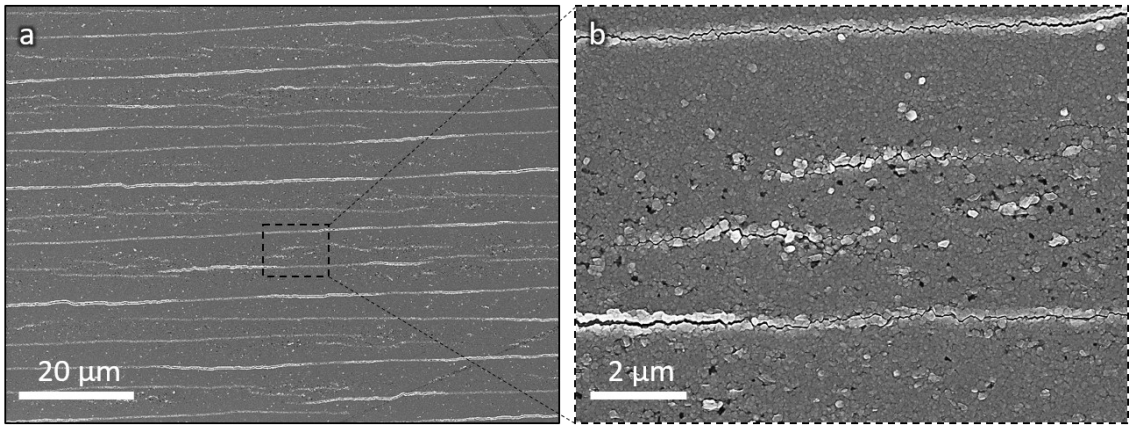

Fig. 6.7 SEM micrographs of a 5:1 Al/Mo bilayer bent with 3.1% bending strain for 20 k cycles. As seen in (a) there are many shorter cracks, often right next to each other, which may give the impression of a single long crack at lower magnifications and/or resolutions. The shortest cracks are in the range of few micrometers as shown in (b).

Further evidence for such behavior can be found with uniaxial *in situ* tensile cyclic straining tests at a similar range of 1% and 2% applied strain to ductile and brittle films such as Au, Cu, printed Ag and Mo [43,182]. Ductile metallizations like Au (500 nm) and Cu (500 nm) show an initial resistance decrease due to grain coarsening, accompanied by a surface roughness increase and TTC formation as the resistance increases, but does not saturate [182]. Brittle printed Ag (700 nm) and sputtered Mo (500 nm) manage to reach an electrical resistance plateau at 1% tensile strain within 1 k cycles during cycling [43,182]. The resistance saturation within 1 k cycles is attributed to the fact that the cracks which have formed through the film thickness do not increase in length. Basically, the crack density has saturated along with the crack growth in the plane of the film and the measured resistance also reaches a plateau. The Al/Mo bilayers represent a combination of ductile and brittle film behavior and both influence the combined electro-mechanical behavior. During cyclic bending, the Al/Mo bilayers show a brittle fracture pattern with long and straight TTCs, which is likely caused by the low fracture resistance of the Mo layer [15,42]. With reduced plastic deformation in the Al layer, the bilayers may only open and close their cracks during cyclic bending as observed for printed Ag and sputtered Mo [43,182]. However, at higher bending strains (3.1%), a rougher surface caused by plastic deformation around the cracks can be observed as shown in Fig. 6.6. The electrical behavior is not only a function of the crack density, but also relies on the crack length within the measured region. The crack length can be evaluated using the cracking factor approach [134], however, for very long cracks, as observed in this study, the relationship breaks down. Still, the average crack length is

overlooked, when the combined electrical and mechanical behavior of thin films is evaluated, and is a key parameter that must be taken into account.

Finally, from the resistance measurements in Fig. 6.5d-f it can be concluded that the increase in surface damage (crack nucleation and growth) within the first 2 k cycles has the greatest influence on the electrical conductivity of the bilayers. Later, in the saturation regime of the bilayer damage, the electrical resistance increases due to further crack propagation in the non-uniform bending area and the connecting of shorter cracks with continued cycling. Apart from that other reasons may also influence the electrical resistance. Continuous bending leads to a deterioration of the surface topography and impedes the spring contacts leading to higher measured resistance values and deviation. Other reasons for the increased resistance, that are not easily measured, may be the continued distortion and enrichment of defects in the bilayer's metal lattices, thus hindering electron transport [183].

6.4.2 LIFETIME PREDICTIONS AND DESIGN CRITERIA

A comparison of different bending conditions and bilayer thickness ratios offers valuable clues about the operational limits of a thin film system, as Alzoubi et al. [169,184] demonstrated for copper thin films. The current investigation concentrates on the effects of different bending strains and thicknesses ratios of Al/Mo bilayers. In Fig. 6.8 the data of this work is denoted under the term "mixed" for alternating between compressive and tensile bending. For a better understanding, the measured values in Fig. 6.8 can be found in section 6.6 (Appendix). The areas designated "tensile" and "compressive" represent data from Chapter 5 [16]. There, similar bilayers, but on different substrates (50 µm PET) were bent either compressive or tensile until 20 k bending cycles were reached. For the severity of the surface damage at ε_b = 1.3% the general trend of mixed > tensile > compressive bending as stated by Glushko *et al.* [86] could be confirmed. For the electrical resistance this trend was not very distinct for the Al/Mo bilayer at 1.3% bending strain. The resistances for mixed (current work) and tensile [16] bending in Fig. 6.8b overlap at 1.3% bending strain and the highest and lowest values for tensile bending actually exceed the values for the mixed bending by a small amount. This shows that only knowing the amount of surface damage is not necessarily sufficient to estimate the electrical reliability of the material system. This is further underlined by the comparison of the surface damage and the electrical resistance for all bending strains in Fig. 6.8. While the difference in surface damage of all bilayers under mixed bending loads for 1.3% and 3.1% bending strains are in a reasonably small range, the values are very different for the electrical resistance values

at the same bending strains. The thinner bilayer ratios are more sensitive to damage and usually display greater resistance changes. This can be attributed to the increasing influence of the brittle Mo layer when the Al/Mo thickness ratio decreases. Other ductile/brittle bilayer combinations such as Au/Cr, Cu/Cr or Inconel/Ag [91–93] confirmed in uniaxial tensile tests that the brittle layers induce brittle fracture of the bilayer with thicker ductile layers showing a better capability to compensate the fracture behavior induced by the brittle layers. A similar behavior is observed here for the 3:1 and 5:1 thickness ratios that was observed for Cu/Cr systems, but for higher ratios of 10:1 or 20:1 [91]. In the relaxed state, TTCs in the Al/Mo bilayers are still conductive as long as there is a connection between both sides of the crack gap. Thicker bilayer ratios have greater cross-sectional areas from the start and it is more likely for them to retain some conductive bridges after bending (Fig. 6.6). Experiments to decouple the effects of the bilayer thickness ratio and total bilayer thickness are to be carried out in the near future.

Furthermore, Fig. 6.8a indicates that all of the bilayers (1:1, 3:1, and 5:1) are undamaged and could withstand 20 k cycles at 0.6% strain (r10) without impacting the electrical resistance of the bilayers. At bending strains of 1.3% and 3.1%, a thickness ratio of 3:1 is appropriate for Al/Mo bilayers and thicker Al films will not improve the mechanical fracture behavior. These results can be applied as design criteria for future flexible electronics. However, these design criteria would not work well for the electrical behavior (Fig. 6.8b). The acceptable resistance values for gate and data bus-lines in TFT displays are interconnected with the display size and the display resolution [24–26,185]. Especially gate electrodes are sensitive to larger resistivity, which can lead to signal delay. Ikeda [24] estimated tolerable bus-line resistivities with pixel design simulations of a defined pixel architecture for rigid TFT displays. For a 10 inch SXGA display standard (1280 px × 1024 px), a reasonable size for a tablet computer, Ikeda's [24] simulation data yield acceptable resistivity values for the gate and data lines around 20 and 70 μΩcm, respectively. The resistivities for the corresponding 1:1, 3:1 and 5:1 Al/Mo bilayers are 13.5, 7.3 and 6.0 μΩcm [15]. The aforementioned limits from Ikeda [24] result in tolerable Al/Mo bilayer resistivity ratios for the TFT gates in the range of 2 to 3 and for the data lines from 5 to 10. The estimated tolerable resistivity ratios are comparable with R/R_0 ratios obtained from this study. The following assessment applies for the lifetime of Al/Mo bilayers in a 10-inch SXGA display according to the R/R_0 ratios in Fig. 6.5. At 0.6% bending strain all bilayers pass the requirements for gate and data lines after 20 k bending cycles. However, for the gate line at 1.3%, the 1:1, 3:1 and 5:1 bilayers reach lifetimes of 0, 100 and 100 cycles, respectively. As data lines, at 1.3% the 1:1, 3:1

and 5:1 bilayers can reach lifetimes of 0, 500 and 500 cycles, respectively. All bilayers fail the gate and data line requirements at 3.1% bending strain before reaching 100 cycles. The use of Al layers larger than 150 nm will increase the expected lifetime of the bilayers. On the other hand, only bent in compression [16], at 1.3% bending strain the 3:1 and 5:1 bilayers are able to withstand 20 k cycles for gate and data line requirements in a 10 inch SXGA display according to Ikeda's estimations [24]. This estimation is only valid for relaxed and flat substrates. What was not considered is the resistance in the bent/strained state, which is expected to be several times higher, similar to printed Ag under tensile cyclic testing [182], which will lead to earlier failure of all bilayers at 1.3% and 3.1% bending strain.

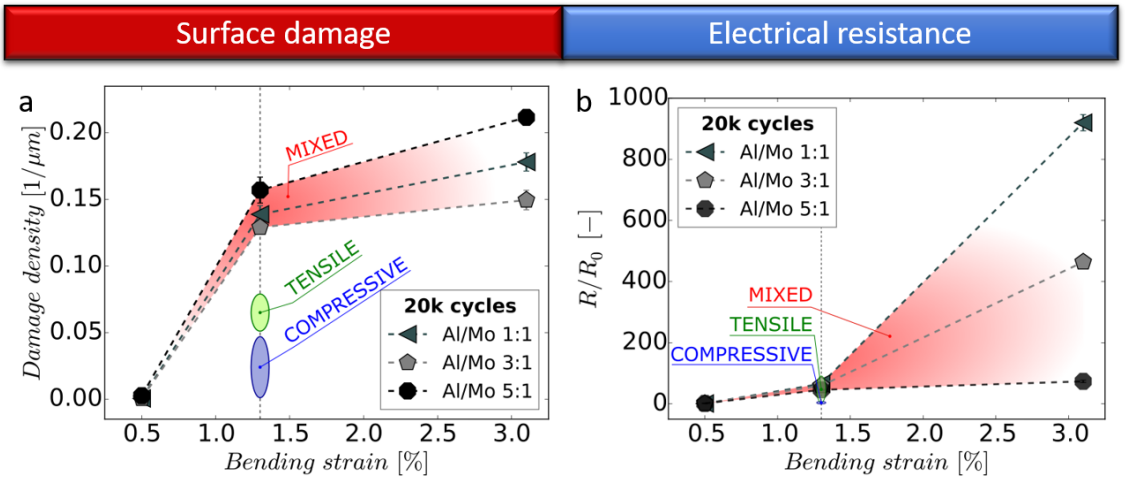

Fig. 6.8 Overview of surface damage and resistance after 20k bending cycles and comparison with tensile and compressive bending of similar bilayers from the previous Chapter 5 [16]. For a better understanding, the obtained values for the mixed bending are detailed in Appendix A.

6.5 CONCLUSIONS

Magnetron sputter deposited Al/Mo bilayer thin films with different layer thickness ratios (1:1, 3:1 and 5:1) on flexible polymer substrates were subjected to 20 k cycles of alternating compressive and tensile bending at three bending strains (0.6, 1.3 and 3.1%). The electrical resistance and mechanical damage evolution were investigated. The damage density in the film mainly depends on the bending strain. Thicker ductile layers combined with lower bending strains increase electrical reliability. The combination of both parameters can change the measured resistance by orders of magnitude after a few thousand bending cycles. Furthermore, the results show that the same samples under uniaxial tensile load do not resemble the damage density or electrical resistance of cyclic bent samples. The mechanisms behind the cyclic bending of conductive thin

films need further attention to better understand the effects of cyclic bending and the accumulation of damage in metallic thin films. The changes in electrical resistance are all related to the damage in the bilayers. The strong initial resistance increase is related to the growing crack density and the crack length until saturation is reached. The comparison of varying Al layer thicknesses and bending strains demonstrate how different parameters influence the results for similar samples, which have to be carefully considered for the design of an actual flexible device.

It has been demonstrated that bilayers can handle more mechanical damage, but electrically, even small amounts of mechanical damage increase the relative resistance by several times. The brittle Mo layer dominates the fracture behavior of the bilayer. Currently, alternating compressed and tensile bending with 0.6% bending strain will be reliable for 20 k cycles, but bending strains at 1.3% and higher will fail before reaching a lifetime 500 cycles. Apart from the flat relaxed state, an examination of the electrical bilayer resistance in the bent state will refine our understanding of the bilayer's limitations. Further modification of the bilayer's microstructure might possibly help suppress crack nucleation and expand the functionality to higher bending strains.

6.6 APPENDIX

More detailed data of the surface damage and electrical resistance.

Table 6.1 shows on overview of the intermittent optical and resistance measurements at 20 k cycles.

Damage density [µm^{-1}] after 20 k bending cycles (Al/Mo)			
ε_b [%]	**Al/Mo 1:1**	**Al/Mo 3:1**	**Al/Mo 5:1**
0.6 (r10)	0.0005 ± 0.0009	0.0005 ± 0.0009	0.003 ± 0.003
1.3 (r5)	0.139 ± 0.006	0.129 ± 0.005	0.157 ± 0.010
3.1 (r2)	0.178 ± 0.007	0.115 ± 0.007	0.212 ± 0.005
R_0 [Ω] at 0 bending cycles (Al/Mo)			
ε_b [%]	**Al/Mo 1:1**	**Al/Mo 3:1**	**Al/Mo 5:1**
0.6 (r10)	8.0 ± 0.6	2.7 ± 0.3	1.2 ± 0.0
1.3 (r5)	6.2 ± 0.5	1.9 ± 0.8	0.8 ± 0.0
3.1 (r2)	4.3 ± 0.5	1.6 ± 0.1	0.6 ± 0.0
R_{20k} [Ω] after 20 k bending cycles (Al/Mo)			
ε_b [%]	**Al/Mo 1:1**	**Al/Mo 3:1**	**Al/Mo 5:1**
0.6 (r10)	9.3 ± 1.0	3.5 ± 0.8	1.3 ± 1.7
1.3 (r5)	400 ± 1	170 ± 53	40 ± 1
3.1 (r2)	4000 ± 100	750 ± 17	50 ± 2

Chapter 7 was almost identically published by the author of this thesis in [45]. In the current thesis, all superfluous equations were replaced with references to the main text. Furthermore, the figure and reference numbering was adapted to fit the thesis.

7 BALANCING THE ELECTRO-MECHANICAL AND INTERFACIAL PERFORMANCE OF MO-BASED ALLOY FILMS

7.1 INTRODUCTION

Magnetron sputter deposited metallic thin films are used as interconnects in TFT displays. For the realization of flexible TFT displays, these metallic thin films have to maintain high electrical conductivity during mechanical loading, as well as being fracture resistant. Mo/Al/Mo multilayer stacks represent widely used metallizations for these TFT electrodes because they have low electrical resistivity, are easy to pattern, and the necessary raw materials for the multilayers are widely available [21,22,32]. In those Mo/Al/Mo multilayers, the brittle Mo layers act as diffusion barriers and adhesion layers, while the Al layer adds ductility and good electrical conductivity.

In the Chapters 4 to 6 [15–17], we studied a simplified Mo/Al bilayer system and showed that the Mo layer in Mo/Al systems negatively impacts the function and lifetime of multilayer films used in flexible display applications. The inherent brittle nature of the Mo layer dominates the mechanical behavior of the Mo/Al metallizations for stretching and bending loads [42,103]. In order to improve mechanical reliability and maintain the electrical function of the individual layers, an increase of the Al layer thickness can improve the reliability of those Mo/Al metallizations [15–17]. However, this measure is not sufficient. Due to an early fracture of the Mo layer, regardless the Al layer thickness, cracks start growing and the Mo/Al metallizations will eventually fail to function. Either the Mo layer has to be substituted by a different film material or optimized in order to keep up with the requirements for flexible applications. Jörg et al. [42] modified and improved the properties of Mo films by process optimization during magnetron sputter deposition. Higher discharge powers led to larger crystallite sizes and compressive residual stresses in the films, which improved both the electrical conductivity and the COS, respectively. The COS was determined from uniaxial tensile experiments, where the normalized electrical resistance R/R_0 is related to the engineering strain, ε, or with the normalized gauge length L/L_0 considering a constant volume approximation (Eq. 3.2) [87,88].

A deviation of R/R_0 from Eq. 3.2 is caused by the formation of structural defects, such as TTCs, and leads to electrical failure of the films, as well as signifies the limitation of Eq. 3.2. In other words, once Eq. 3.2 loses its validity, due to structural damage of the film, COS occurs. Biaxial effects, such as the influence of the substrates Poisson's ratio due to the much higher thickness of the substrate (50 µm) compared to the tested films (50 to 500 nm) and a change of the surface roughness of the films are not considered in Eq. 3.2. In this study the COS was determined at small strains and according to Glushko et al. [88], at small strains those influences are negligible. In the current work, a 10% deviation of the electrical resistance from the theoretical resistance determined with Eq. 3.2 was defined as the threshold to determine a clear COS.

Besides process optimization, another approach to improve the properties of the Mo layer is alloying with suitable elements. Jörg et al. [44,186] showed that alloying Mo with Re or Cu can improve the COS by at least 100%. However, the electronic structure in alloys at higher solute concentrations suffers from perturbations and leads to increased electron scattering, yielding high resistivities [44,187]. Alloying metals with different crystal structures may also lead to multiphase structures that can be detrimental to conductivity, as was reported for alloys of body centered cubic (bcc) Mo and hexagonal close packed Re [44].

In the current study, three Mo-alloy thin film systems, namely Mo-Al, Mo-Nb and Mo-Ta, were evaluated with respect to their suitability to replace pure Mo films in Mo/Al/Mo multilayers. The used alloying elements present a wide spectrum of Young's moduli with E_{Al} = 70.6 GPa, E_{Nb} = 104.9 GPa, E_{Ta} = 185.7 GPa and E_{Mo} = 324.8 GPa [188]. Al is a light and ductile element, which is already part of the process chain in display manufacturing. The weight of Nb is similar to Mo and both are known to show good miscibility. Ta is in the same group as Nb and chemically very similar. However, Ta is a heavy element with a higher Young's modulus than Nb and has shown good diffusion barrier properties as well as a beneficial effect on sheet resistivity by lowering it [189]. Therefore, the atomic masses of the used alloying elements Al, Nb, and Ta are respectively lighter, similar, and heavier compared to the atomic mass of Mo.

For comparison of the respective alloy thin films, the electro-mechanical behavior of the films was evaluated using monotonic uniaxial testing in combination with *in situ* 4PP resistance measurements. These tensile tests are easy to execute, time efficient and sufficient to qualitatively determine suitability of a material system for flexible applications [15]. Furthermore, the interface adhesion is evaluated on selected alloy compositions using the tensile induced delamination method [120] to ensure they fulfill their function as adhesion layers.

7.2 MATERIALS AND METHODS

In the current work, all atomic fractions of the Mo-based alloys are given in the form at.% alloying content. There are no stoichiometric compositions mentioned in this work.

Mo-Al, Mo-Nb and Mo-Ta alloy thin films were synthesized using a laboratory scale direct current magnetron sputter system. Up to three targets can be mounted onto unbalanced AJAA320-XP magnetrons, which are focused onto the rotatable sample holder at a distance of 40 mm. The base pressure of the chamber before each deposition run was below 1×10^{-3} Pa. Prior to film deposition, PI (UBE UPILEX-S 50 S, 50×50 mm^2, 50 µm thickness) and Si (100) substrates were fixed with Kapton tape to the rotatable substrate holder and plasma cleaned for 2 min at an Ar pressure of 1 Pa in an asymmetrically bipolar pulsed direct current plasma using a substrate voltage of -350 V and a frequency of 50 kHz. The 50 and 500 nm thick Mo-Al, Mo-Nb and Mo-Ta alloy films were synthesized by magnetron co-sputtering from Mo, Al, Nb and Ta single-element targets (∅ 50.8 mm × 6 mm) using two of the three available magnetrons. As reference, pure Mo films with the same thicknesses were used. All films were grown without external heating on floating substrates at an Ar pressure of 0.5 Pa. Chemical compositions within the three alloy film systems were varied by adjusting the power applied to the individual magnetrons, while maintaining similar deposition rates to achieve comparable growth conditions. Table 7.1 displays an overview of the alloy compositions studied. The chemical compositions were measured on the 500 nm thick alloy films grown on Si substrates using energy dispersive X-ray spectroscopy (EDS) with ZAF corrections. The ZAF correction corrects inter-element effects in a material, where Z is the correction of the atomic number, A for absorption effects and F for fluorescence. In addition, the chemical compositions of the 50 nm thin films – which cannot be easily measured – were calculated from the deposition rates of the individual elements, which were obtained from the time and thicknesses of the respective single element films. The thicknesses of these elemental reference films grown on Si substrates were measured using a white light optical profilometer (Veeco Wyko NT 1000) with Vison64 software via automatic step measurement. The comparison of calculated alloy compositions and the obtained EDS data on 500 nm alloy films yielded a compositional error of around ±5 at.%. The 50 nm thick alloy films used for the electro-mechanical and for the adhesion tests were deposited with the same deposition parameters as the 500 nm thick films on PI substrates. For these tests, the coated 50×50 mm^2 PI substrates were cut into strips of 6 mm width and 40 mm length.

Monotonic uniaxial straining with *in situ* 4PP resistance measurements were used for electro-mechanical testing. For each alloy composition, 2-3 samples were

tested using the same procedure. The 6 mm × 40 mm strips were mounted onto custom made grips with two embedded pins to measure the resistance with the 4PP method along the sample, as described in [88]. The grips are attached to a MTS Tytron 250 device, which measures simultaneously time, force and displacement. The *in situ* 4PP resistance measurements were performed with a Keithley 2000 digital multimeter and recorded with the free software Scilab [162] as a function of time to calculate the engineering strain. All experiments used a gauge length of 20 mm, a displacement rate of 5 µm/s (for loading and unloading) and the samples were strained to 12% engineering strain. After unloading, the formed cracks and crack spacings were evaluated using SEM images. The crack spacing was quantified using a line intercept method with five profile lines using the free software ImageJ [168].

The resistivity, ρ_0, of the samples was calculated from the initial resistance, R_0, with electrodes modified for the tensile straining device and the sample geometry with the relation, $\rho_0 = R_0 \, {A_0}/{l_0}$, where A_0 is the original cross sectional area and l_0 is the original gauge length (20 mm) of the mounted bilayer in the tensile stage before straining.

Additional experiments were performed to assess the adhesion energy of the different alloys. The tensile stress induced delamination model is best applied when the film has reached the initial buckling strain [120,167]. Samples with 10 at.% alloying element (Al, Nb, or Ta) and the pure Mo film were strained *in situ* under a CLSM. That way, the effect of the alloying content on the adhesion energy could be properly compared for all three alloys. To quantify the adhesion energy with the tensile induced delamination model, the films were strained to the point where the film starts to delaminate, or buckle, between the cracks. Buckles were then measured using a DI Dimension 3000 atomic force microscope. Using intermittent contact mode, 10-15 buckles were imaged for each film and the buckle dimensions assessed (buckle height, δ, and buckle width, $2b$). The buckle dimensions were then plotted as b/h versus $\sqrt{\delta/h}$ and fitted with Eq. 7.1

$$\sqrt{\frac{\delta}{h}} = (2\alpha)^{\frac{1}{4}} \frac{b}{h} \left(1 + \sqrt{1 + \frac{3}{4}\alpha \left(\frac{b}{h}\right)^4}\right)^{-\frac{1}{4}}. \qquad (7.1)$$

where h is the film thickness and α is a fitting parameter needed to calculate the adhesion energy, Γ [120]. Once the α-parameter is known, the adhesion energy is determined with knowledge of the modified elastic modulus, $E' = E_f/\left(1 - \nu_f^2\right)$ (where E_f is the film elastic modulus and ν_f is the Poisson's ratio of the film), using Eq. 7.2 [120]

$$\Gamma = \frac{\alpha h E'}{4}\left(\frac{2}{\pi}\right)^{\frac{1}{4}}. \qquad (7.2)$$

Due to the fact that the alloy films studied here are only 50 nm thick, it is not possible to measure a meaningful elastic modulus or Poisson's ratio values. Therefore, the elastic modulus and Poisson's ratio for Mo [188] will be used for all films. By using the same elastic modulus, relative changes in the adhesion energy can be determined.

7.3 RESULTS: ALLOYS UNDER MONOTONIC UNIAXIAL TENSILE LOADS

A comparison of the 50 nm Mo alloy film sheet resistivities on PI confirms a general increase with increasing alloying content no matter the alloying element, as displayed in Fig. 7.1. Mo-Al shows a larger increase than the Mo-Nb and Mo-Ta alloys. For the Mo-Nb alloys, only a slight resistivity increase was observed, however, the Mo-Nb with 10 at.% Nb has a larger average resistivity than 50 at.% and 90 at.% Nb, due to one sample with high initial resistance, probably due to preexisting damage of the films. The resistivity values of the Mo-Ta alloys are similar to the Mo-Nb alloys.

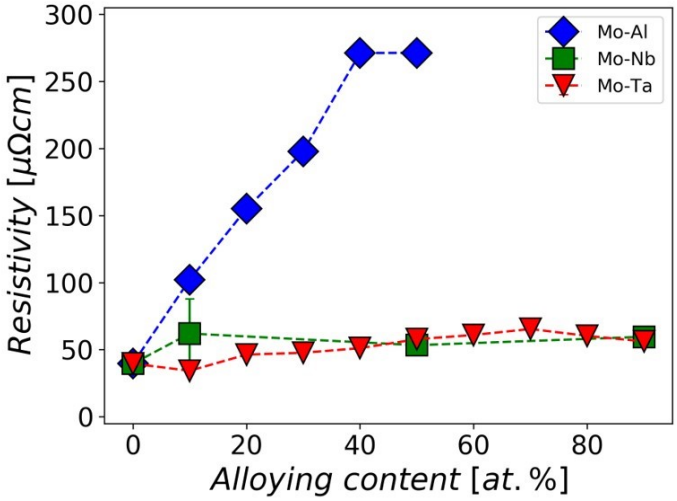

Fig. 7.1 Initial resistivity, ρ_0, before straining as a function of the alloying content for different 50 nm thick Mo alloy films. Pure Mo films are plotted as 0 at.% alloying content. The dashed lines have no mathematical meaning and are used to only guide the eye. Measured values in section 7.6, Table 7.6.1.

The progression of the normalized resistance during *in situ* electro-mechanical testing of the various alloys is shown in Fig. 7.2. Once structural defects, such as cracks, form in the thin films, the normalized resistance responds with an increase. The exact starting point of the deviation from the theory given by Eq. 3.2 is difficult to determine. Thus, as failure criterion, the COS in the current study is defined as 10% deviation from

Eq. 3.2. The COS obtained from the uniaxial tensile tests in Fig. 7.3 shows a similar trend as the resistivity plotted in Fig. 7.1, which exhibits an increase with higher alloying contents, starting from the pure Mo film with a COS of 1.1% strain. Mo-Al alloys follow the trend of increasing COS from increasing Al alloying content. However, from 40 to 50 at.% Al the trend is not applicable, due to a possible transition from nanocrystalline to amorphous structure in that range of Al content, as was reported by Car et al. [190]. Alloying Nb into a Mo film leads to a sharp decrease of the COS to 0.3% with 10 at.% Nb, however, it increases with increasing Nb content until it reaches 1.3% at 90 at.% Nb. The COS values of the Mo-Ta alloys show a continuous rise with increasing Ta content and reach a maximum of nearly 3.2% strain with 90 at.% Ta.

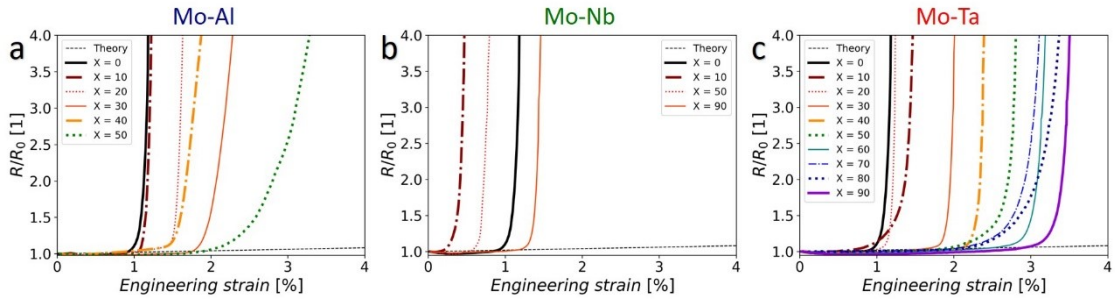

Fig. 7.2 Representative normalized resistance as a function of the engineering strain of (a) Mo-Al, (b) Mo-Nb, and (c) Mo-Ta alloy films obtained from monotonic *in situ* uniaxial tensile tests. The "X" denotes how much the Mo was alloyed in at.%. The COS is defined as 10% deviation from the dashed black theory line defined by Eq. 3.2.

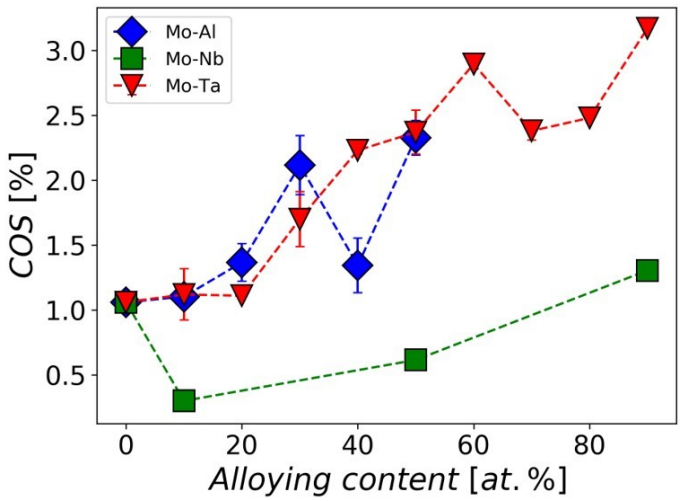

Fig. 7.3 COS versus alloying content for 50 nm thick Mo alloy films. Pure Mo films are plotted as 0 at.% alloying content. The dashed lines have no mathematical meaning and are used to only guide the eye. Measured values in section 7.6, Table 7.6.2.

A comparison of cracks from SEM images is shown in Fig. 7.4. All cracks observed were straight brittle cracks with some buckle delaminations visible. The measured crack spacings (Table 7.1) all range between 2.3 and 4.5 μm with the higher average crack spacings occurring for the samples with higher alloying content. The Mo-Nb alloys, however, are characterized by the opposite trend, with the samples with less alloying content films having a larger crack spacing.

Table 7.1 Overview of saturation crack spacings for the 50 nm thick Mo, Mo-Al, Mo-Nb and Mo-Ta films after straining to 12%. "X" denotes how much the Mo was alloyed in at.%.

Crack spacing [μm]	**X = 0**	**10**	**20**	**30**	**40**	**50**	**60**	**70**	**80**	**90**
Mo-Al	2.3 ± 0.1	2.9 ± 0.2	3.1 ± 0.1	3.2 ± 0.1	2.6 ± 0.1	4.1 ± 0.2	-	-	-	-
Mo-Nb		3.2 ± 0.2	-	-	-	2.7 ± 0.1	-	-	-	2.4 ± 0.1
Mo-Ta		2.7 ± 0.1	2.5 ± 0.0	2.9 ± 0.0	3.4 ± 0.3	3.7 ± 0.4	4.1 ± 0.3	3.5 ± 0.1	4.1 ± 0.1	4.5 ± 0.1

Analysis of the buckle data with the tensile induced delamination [120] found that alloying Mo with Al, Nb and Ta can increase the adhesion energy. Fig. 7.5 illustrates the data for all films (pure Mo, 10 at.% Al, Nb, and Ta) and the fit of Eq. 7.1 to the data. Using the α-parameter, the elastic modulus and Poisson's ratio for Mo, 324.8 GPa and 0.335 [188], respectively, the interface strength was calculated with Eq. 7.2. For pure Mo, Γ= 0.36 $\pm$ 0.17 J/m^2 and for Mo-Al and Mo-Nb the interface strength was statistically the same with Γ= 0.42 $\pm$ 0.14 J/m^2. Adding Ta to Mo increases the interface strength 3-fold to Γ= 1.4 $\pm$ 0.28 J/m^2. These adhesion values are similar to those previously measured for several different metal-polyimide film systems [103,120,167,191–194].

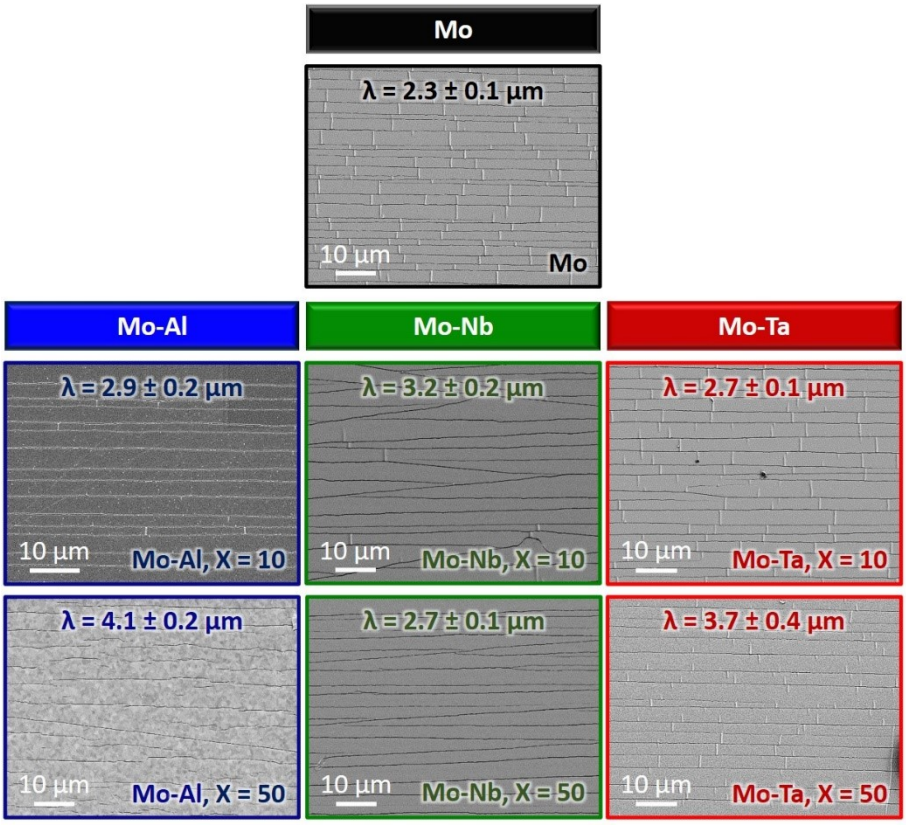

Fig. 7.4 Representative SEM surface images of 50 nm thick Mo, Mo-Al, Mo-Nb and Mo-Ta films after straining to 12%. The label at the top annotates the average crack spacing, λ, and the "X" in the lower right corner annotates how much the Mo was alloyed in at.%.

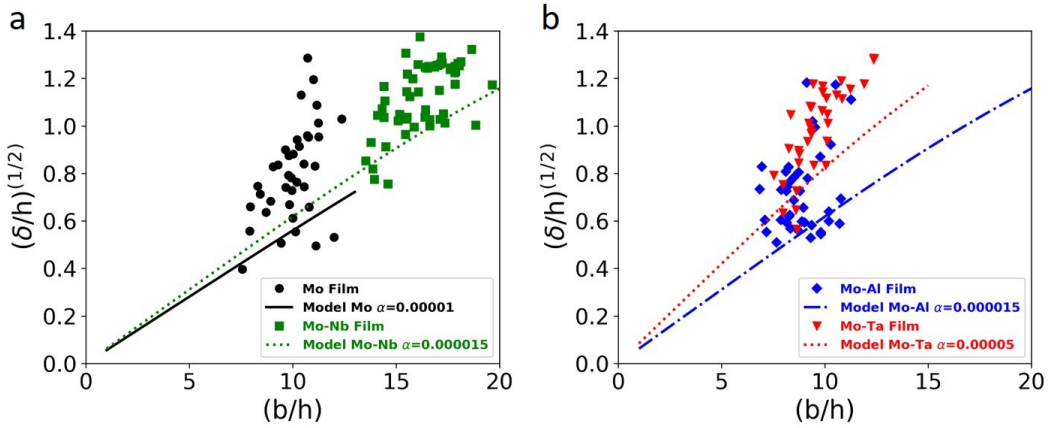

Fig. 7.5 Measured buckle dimensions normalized by the film thickness and plotted for (a) the pure Mo and Mo-Nb films and (b) the Mo-Al and Mo-Ta films. The lower buckle dimensions are fit using Eq. 7.1 to find the α-parameter needed to calculate the interface strength.

7.4 DISCUSSION

The resistivities of the 50 nm thick Mo-Al alloy films increase with rising alloying content and reach a maximum of 270 µΩcm for Mo-Al at 40 and 50 at.% Al (Fig. 7.1). In contrast, the resistivity of the 50 nm thick Mo film was 40 µΩcm. As a reference, the resistivities

of the pure bulk metals Mo, Al, Nb and Ta at 273.2 K found in literature are 4.9, 2.4, 13.27 and 12.1 μΩcm, respectively [195]. The increasing resistivity upon alloying is attributed to the larger scattering of the electrons with increasing fractions of alloying elements due to a growing number of defects in the bcc-Mo lattice [187]. The Mo-Al alloy resistivities agree well with values published in other studies [190,196], though the results in this work show a mostly linear relation between resistivity and Al content as is opposed to studies with comparable Mo-Al alloys [190,196]. The difference might be caused by the contact resistance and a contribution from the grips during the measurement [88]. As mentioned in section 2, there is an estimated error of ±5 at.% for all alloy compositions investigated within this work. Verification of the 50 nm thick alloys calculated composition was not possible by EDS.

The results obtained for the Mo-Al alloys in Fig. 7.1 and 7.3 indicate that the COS is more sensitive to the chemical composition than the resistivity. With a maximum COS of 2.5%, the 50 nm thick Mo-Al alloys surpassed the COS of a pure 50 nm thick Mo film (1.1%). Thus, using Mo-Al instead of Mo would enable more freedom for the design of flexible devices. However, while the COS increases by about a factor of 2 compared to Mo, the electrical resistivity rises by a factor of 7 (Fig. 7.1). The electrical resistivity of a polycrystalline thin film is usually related to its grain size [187], which itself is determined by the film thickness [197]. However, Car et al. [190] reported that Mo-Al alloys with 50 at.% Al and an amorphous crystal structure yielded a higher electrical resistivity. Due to the lack of grains, we assume that the electrical resistivity should be widely independent from the film thickness. The observed cracks in the Mo-Al films are all straight brittle cracks (Fig. 7.4) and do not illustrate any crack deflection (zig-zag or tortuous cracks) due to the addition of Al. This type of crack transformation from straight to wavy signifies a beneficial transition from brittle to ductile mechanical behavior. It was previously observed for Mo-Cu alloys [186], leading also to a higher COS with increasing Cu content. Finally, the addition of 10 at.% Al to Mo did not statistically change the adhesion energy to polyimide.

In comparison, the resistivities of Mo-Nb (50-60 μΩcm) are closer to the resistivity of the pure Mo film (40 μΩcm), as shown in Fig. 7.1. This is expected, due to the fact that Mo and Nb have both bcc structure and complete miscibility [198]. Among the three tested Mo-Nb alloys, samples at 10 and 50 at.% Nb yielded lower COS than the Mo reference (COS = 1.1%). With a low resistivity, but high sensitivity to damage, Mo-Nb alloys do not fulfill the necessary requirements to substitute Mo adhesion layers in flexible electronics. The crack spacings for the Mo-Nb films follow the opposite trend to the Mo-Al and Mo-Ta films, with the crack spacing decreasing rather than increasing

with increasing Nb content. The crack spacing combined with the poor COS values and having only a small increase in the adhesion energy excludes Mo-Nb alloys as adhesion promoting layers or as fracture resistant coatings for flexible TFT displays.

The tested Mo-Ta alloys, in the range from 10 to 90 at.% Ta content, yield films with electrical resistivity similar to pure Mo films (40 μΩcm). All Mo-Ta alloys have resistivities in a range between 35 and 65 μΩcm (Fig. 7.1). These results for the Mo-Ta alloys roughly match the results obtained by Hofer et al. [199], who studied single-phase Mo-based solid solution films with up to 63.7 at.% Ta. Note that the electrical resistivities in the current study have not been measured according to standard [200], were not corrected and, therefore, represent only qualitative data to compare those films examined within the current work. In particular, the values presented here are expected to be higher than those reported in other studies [190,196,199], caused by a constant electrical resistance term associated with contact resistance and resistance of the film under the grips used for the measurement [88]. The COS for Mo-Ta alloys in Fig. 7.3 rises with increasing Ta content and reaches a maximum COS of 3.2% at 90 at.% Ta. Again, the cracks that formed during straining were straight brittle cracks. Even for the 90 at.% Ta film with the highest COS, only straight cracks were observed. However, the average crack spacing did increase with increasing Ta content, achieving the largest crack spacing of 4.5 μm for 90 at.% Ta. All Mo-Ta films did exhibit delamination buckling after straining to 12%. The observation of delamination buckling would infer that Mo-Ta has poor adhesion. Quantifying the adhesion energy of only the 10 at.% Ta film evidenced that the interface strength was about 3 times higher than for the pure Mo film. Based on the result for the Mo-Ta alloy with 10 at.% Ta, a satisfactory adhesion strength of Mo-Ta alloys with higher Ta content is expected. Further characterization with transmission electron microscopy is needed to better understand the adhesion energy increase.

Overall, Mo-Ta alloys show the best prospects to substitute Mo films as electrode material in flexible TFT displays. The Mo-Ta alloys combine low resistivity similar to Mo-Nb alloys and Mo films, but also have high COS like Mo-Al alloys, as displayed in Fig. 7.6. One of the main issues of alloyed Mo films is that mixing different elements will lead to higher electrical resistivity due to the disturbance of the pure Mo lattice [187]. In order to optimize conductivity, elements with similar properties to Mo are best suited. For example, Mo-Nb and Mo-Ta alloys showed low resistivity. Both elements are neighbors with Mo in the periodic table and all three have a bcc crystal structure. However, a metastable tetragonal β-Ta modification can occur under non-equilibrium magnetron sputter conditions for pure Ta films [199,201]. Additionally, Ta is a heavy element and

likely beneficial for the use in diffusion barriers [189]. Mo films alloyed with Ta performed best among the tested alloys. Although Mo alloyed with Al, Cu or Re yield ductile alloys with a relatively high COS, their different crystal structure to Mo leads to alloys with high electrical resistivities, which is unsuitable for TFT displays [44,186].

Repeated stretching or bending of an electrode or device will eventually lead to failure. To improve lifetime and functionality, electrodes need low resistivity and high damage resistance (high COS). Within the present work, Mo-Ta also outperformed Mo-Al and Mo-Nb in regards to interface strength to polyimide and could also be assisting the improvement of fracture resistance. Since the beginning of testing metal films on polymer substrates with tensile straining, it has been stressed that the adhesion between the metal film and polymer substrate must be strong in order to mitigate crack formation [111,202].

The main design parameters for flexible thin film electrodes, COS and electrical resistivity, are displayed as a map with the tested alloys in Fig. 7.6. The lower right corner displays the most desirable combination of both parameters, which makes it easier to identify appropriate material systems, which are in this study the Mo-Ta alloys with at least 40 at.% Ta. Note that the oval colored areas in Figure 6 have no mathematical or statistical meaning and are only here to guide the eye.

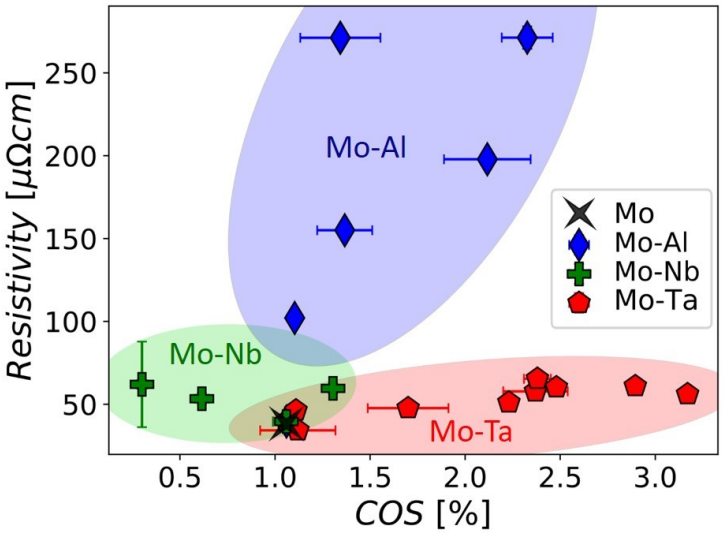

Fig. 7.6 Electrical resistivity versus COS for the 50 nm thick alloy films examined in the current Chapter. The oval colored areas for the alloys are to guide the eye and have no mathematical or statistical meaning.

7.5 CONCLUSIONS

Mo-Al, Mo-Nb and Mo-Ta films with thicknesses of 500 and 50 nm were co-deposited via direct current magnetron sputter deposition onto polyimide substrates. The electro-mechanical performance and interfacial strength of the 50 nm thick alloy and the pure Mo films were tested and compared. In order to identify the best suited material system for flexible thin film electrodes, monotonic *in situ* uniaxial tensile tests were performed along with a quantitative measurement of the interface strength for selected compositions. The two main properties of initial resistivity and COS were determined and compared. A combination of low resistivity and high COS should ensure improved qualitative lifetime of flexible electronics for repeated loading (stretching or bending) as well as good adhesion. Among the tested material systems, Mo-Ta alloys with 40 at.% Ta and more show the highest prospects to replace the Mo adhesion layers in current TFT display applications. Compared to pure Mo films, their electrical resistivity is similar and the COS and interface strength are 2 to 3 times higher, meaning that the material has a higher tolerance for damage formation and is well suited for use in flexible electronic applications.

7.6 APPENDIX

Table 7.6.1 Overview of initial electrical resistivities for the 50 nm thick Mo, Mo-Al, Mo-Nb and Mo-Ta films on PI. A standard deviation of "± 0" refers to an error smaller than 2.5 µΩcm. "X" denotes how much the Mo was alloyed in at.%.

ρ_0 [µΩcm]	X = 0	10	20	30	40	50	60	70	80	90
Mo-Al	40 ± 0	100 ± 0	155 ± 5	200 ± 0	270 ± 5	270 ± 5	-	-	-	-
Mo-Nb	40 ± 0	60 ± 25	-	-	-	55 ± 5	-	-	-	60 ± 5
Mo-Ta	40 ± 0	35 ± 0	45 ± 0	50 ± 0	50 ± 0	60 ± 0	60 ± 0	65 ± 0	60 ± 0	55 ± 0

Table 7.6.2 Overview of COS for the 50 nm thick Mo, Mo-Al, Mo-Nb and Mo-Ta films on PI. "X" denotes how much the Mo was alloyed in at.%.

COS [%]	X = 0	10	20	30	40	50	60	70	80	90
Mo-Al	1.06 ± 0.07	1.10 ± 0.03	1.37 ± 0.14	2.12 ± 0.23	1.34 ± 0.21	2.33 ± 0.13	-	-	-	-
Mo-Nb	1.06 ± 0.07	0.30 ± 0.03	-	-	-	0.62 ± 0.04	-	-	-	1.31 ± 0.01
Mo-Ta	1.06 ± 0.07	1.12 ± 0.20	1.11 ± 0.01	1.70 ±0.21	2.23 ± 0.03	2.37 ± 0.17	2.90 ± 0.04	2.38 ± 0.07	2.48 ± 0.01	3.17 ± 0.01

Chapter 8 was almost identically submitted by the author of this thesis for publication in [203]. In the current thesis, all superfluous equations were replaced with references to the main text. Furthermore, the figure and reference numbering was adapted to fit the thesis.

8 IMPROVED ELECTRO-MECHANICAL RELIABILITY OF FLEXIBLE SYSTEMS WITH ALLOYED ADHESION LAYERS

8.1 INTRODUCTION

Commonly used electrode material systems in TFT displays are Mo/Al/Mo multilayers, with Mo layer thicknesses of 50-200 nm and Al layer thicknesses of several hundred nm [21,22]. The Mo layers act as adhesion and diffusion barrier layers, while the Al layers provide the necessary high electrical conductivity. These Mo/Al/Mo multilayers display low resistivities of about 3 μΩcm [32]. Previous works [15–17,91–93] of electro-mechanical testing on simplified Al/Mo, Au/Cr, Ag/Inconel, and Cu/Cr bilayers showed that the brittle layers led to failure of the bilayers under uniaxial tensile strain [15,91–93] and cyclic bending [16,17]. For application of the Al/Mo systems in flexible displays, several possibilities to improve their electro-mechanical performance come to mind, as specified in the following: (i) modification of layer thickness, (ii) design changes to decrease the applied strain, (iii) tuning the microstructure and stresses of the Mo layer, and (iv) substitution of the Mo layer.

The fracture behavior can be modified by (i) changing the thicknesses of the brittle and ductile layers [95,103]. In general, better fracture behavior can be achieved by increasing the thickness of the ductile layer [15,91,95]. However, the improvement in damage resistance by increasing the Al layer thickness is likely limited, due to simultaneously growing dislocation activity at several hundred nm thickness [176].

Changing the design of a flexible device in order to apply lower strains on the TFT structures (ii) may improve robustness and lifetime of the device. Such improvements by design may be achieved by increasing the bending radius [17], the orientation of a TFT with regard to the bending axis [27], the addition of protective layers to move the brittle elements to the neutral plane [27], the establishment of multiple neutral planes through soft adhesive interlayers [29,30], or splitting the electrodes to achieve better crack resistance [38].

Modifying the Mo layer in a way that makes it behave more ductile and crack resistant (iii) can improve fracture behavior and can be implemented in existing

production processes. Jörg et al. [42] demonstrated how an appropriate change of sputter deposition parameters can improve fracture behavior and adhesion by increasing compressive stress of the Mo films. Further, the introduction of a zigzag structured Mo film instead of a Mo film with columnar grains improved the crack resistance [43]. However, these approaches are limited for large-scale applications.

Finally, substitution of the brittle Mo layer with other materials (iv) holds great potential. However, any new material to substitute Mo needs an adequate adhesion, good diffusion barrier properties, low electrical resistivity and ductile behavior with high failure strains in order to improve flexibility and lifetime. Furthermore, any new material system needs to behave similar to Mo in all processing steps of TFT structures, i.e. deposition, etching.

In this Chapter, a simplified bilayer system containing an Al layer and a newly developed Mo-based interlayer will be examined. The new interlayer is an improved Mo-Ta alloy with higher crack resistance, based on our results from a previous study on Mo-based alloys [45]. Mo-Ta alloys have an about 20% higher electrical resistivity and an up to three times higher COS than Mo films, and an improved adhesion to PI substrates compared to Mo interlayers of the same thickness [45]. The new optimized Al/Mo-Ta bilayers were tested with different Al layer thicknesses by monotonic uniaxial tensile tests with *in situ* 4PP resistance measurements (for potential stretchable applications) and by intermittent cyclic bending with *ex situ* 4PP resistance measurements (for foldable and rollable applications). At the end of the uniaxial tests und during the intermittent measurements of the bending tests, images with CLSM were recorded to evaluate the surface damage. The results will demonstrate an improved failure resistance for both types of loading when the Mo-Ta interlayer is used compared to Mo interlayers.

8.2 MATERIALS AND METHODS

8.2.1 THIN FILM DEPOSITION

The Al/Mo-Ta bilayers studied in the current work were deposited onto PI (UBE Upilex-S 50 S and 125 S, corresponding to 50 and 125 µm thickness, each with dimensions 50 × 50 mm^2) and (100) silicon substrates (dimensions 6 × 20 mm^2, thickness 325 µm) using a laboratory scale dc magnetron sputter system. Three circular planar targets (Al, Mo, and Ta targets with a diameter of 50.8 mm and a thickness of 6 mm each, provided by Kurt J. Lesker (Al, Ta) and Plansee SE (Mo)) were fixed to unbalanced AJAA320-XP

magnetrons and focused onto the center of a rotatable sample holder at a distance of 40 mm. Prior to deposition, the substrates were ultrasonically cleaned in ethanol for 5 min and dried in hot air. The substrates were mounted onto the rotatable substrate holder (kept on a floating potential) with Kapton tape. The base pressure of the sputter system was always less than 1×10^{-5} mbar. The substrates were plasma cleaned at an Ar pressure of 1 Pa in an asymmetrically bipolar pulsed dc plasma using a substrate voltage of -350 V and a frequency of 50 kHz for 2 min.

Two film thickness, namely 30 and 500 nm thick, Mo-Ta alloy films with 50 at.% Ta were deposited without external heating with constant discharge powers of 188 W for the Mo and 130 W for the Ta magnetron at an Ar pressure of 0.25 Pa. With these discharge powers, deposition times of 26 and 433 s were used for the 30 and 500 nm film thicknesses, respectively. As shown in our earlier work, the chosen composition Mo with 50 at.% Ta yields a Mo-based solid solution with incorporated Ta atoms [199]. During deposition of the Mo-Ta alloy, the shutter for the already powered Al target was closed. Subsequently, Al films with thicknesses of 30, 75 and 150 nm were deposited onto the 30 nm thick Mo-Ta alloy films with a discharge power of 166 W for the Al magnetron at 0.5 Pa Ar pressure, corresponding to deposition times of 51, 128, and 256 s, resulting in Al/Mo-Ta bilayer thickness ratios of 1:1, 2.5:1 and 5:1. The 2.5:1 ratio will be referred to as 3:1 ratio in the current study.

8.2.2 THIN FILM CHARACTERIZATION

The deposition parameters used induce high compressive residual stresses in the Mo-Ta interlayer. The residual stresses of the Mo-Ta alloys were verified with a custom-built wafer curvature device with two parallel laser beams by application of the modified Stoney equation [58,204,205] for a 500 nm thick Mo with 50 at.% Ta alloy film on a silicon substrate and was in the range of -1.9 GPa.

The thicknesses of the individual layers were calculated from the individual deposition rates of the Al, Mo and Ta targets. The deposition rates were obtained from single target depositions prior to bilayer deposition, where deposition time and film thickness were recorded. The thicknesses of the single target depositions were measured using a white light optical profilometer (Veeco Wyko NT 1000) with Vison64 software via automatic step measurement. The elemental composition of the Mo-Ta alloy interlayer was calculated from individual elemental deposition parameters. Furthermore, the elemental composition was verified on 500 nm thick Mo-Ta alloy films on silicon substrates by EDS, with built-in sensitivity factors for calibration. The 500 nm

thick Mo-Ta alloy films (50 at.% Ta) were deposited with the same parameters as used for the Al/Mo-Ta bilayers.

8.2.3 TESTING METHODS

For electro-mechanical testing, the as deposited films were cut into 6 × 40 mm² stripes. In the monotonic uniaxial tensile tests, two samples for each thickness ratio 1:1, 3:1, and 5:1 were tested. In the cyclic bending tests, three samples for each combination of Al/Mo-Ta thickness ratio and applied bending strain (1.3 and 3.1%) were tested.

Monotonic uniaxial tensile tests

Monotonic uniaxial tensile tests with *in situ* 4PP resistance measurements were performed, similar as in references [87,177], to compare the performance of the Al/Mo-Ta bilayers with previously tested Al/Mo bilayers. Using an MTS Tytron 250 microforce testing system, tensile tests were displacement controlled with a displacement rate of 5 µm/s during loading and unloading. The bilayers on 50 µm thick PI were strained up to a maximum of 12% engineering strain. The samples were mounted between two rectangular custom-built grips (about 15 × 20 mm²) embedded with two pins for 4PP resistance measurements, as sketched in Fig. 8.1a. The gauge length was 20 mm. The *in situ* 4PP resistance was recorded with a Keithley 2000 digital multimeter, using the free software Scilab [162]. As failure criterion for the uniaxial tensile tests, a COS deviating 10% from the theoretical normalized electrical resistance behavior using the constant volume approximation, Eq. 3.2, was defined [87,177].

Post mortem CLSM images of the strained surfaces were recorded to determine the surface damage. The damage density was evaluated from CLSM images using a line intercept method with three profile lines perpendicular to the crack direction in each image, utilizing the free software packages Gwyddion [180] and ImageJ [168]. Additional complementary SEM micrographs were recorded to inspect surface damage under higher magnification than CLSM.

Cyclic bending

Intermittent bending tests with the custom-built FLEX-E-TEST [16,17,86] were performed on the Al/Mo-Ta bilayers to record their performance under certain strain and loading conditions. The samples were mounted onto a grip attached to rotatable wheel. The wheel rotates at a frequency of 1 Hz and changes directions every 10 turns, thus alternating between applying compressive and tensile stress (mixed bending) to the Al/Mo-Ta bilayers (Fig. 8.1). Mixed bending was chosen because it has been shown

to be the most destructive type of bending [17,86]. During the movement of the wheel, the mounted sample passes an anvil and is forced to bend along the radius of the grips, as sketched in Fig. 8.1b. The radius, *r*, of the grips was 2 mm and applies bending strains, ε_b, of 1.3 and 3.1% for 50 and 125 µm thick PI substrates, respectively, as estimated from the relation, $\varepsilon_b = d_s/(2r)$, where d_s is the substrate thickness. The bilayer thickness of 180 nm (5:1 or 150/30 nm) is minor compared to the substrate thickness and is therefore considered negligible for the applied bending strain. The actual bending event takes place at roughly one eighth of a whole cycle in the FLEX-E-TEST. Calculating the approximate strain rate, $\dot{\varepsilon}$, with $\dot{\varepsilon} = \varepsilon_b/\Delta t$, and Δt being the duration of one bending event, yields approximate strain rates of 0.10 and 0.25 s^{-1} for 1.3 and 3.1%. bending strains, respectively.

The Al/Mo-Ta bilayers were cyclically bent up to 50,000 (50 k) cycles. After 20, 60, 80, 100, 500, 1 k, 2 k, 5 k, 10 k, 20 k, and 50 k bending cycles, the bilayers were dismounted for intermittent 4PP resistance measurements and CLSM images of the bent area. The setup for the *ex situ* 4PP resistance measurements is similar to the setup of the uniaxial tensile tests and consists of two rectangular grips, embedded with two pins for the electrical resistance measurement, and adjusted to the length of the bent area, which is approximately 3.1 mm for the applied bending radius [17]. The damage density was evaluated the same way as the uniaxially strained samples in the previous section, however, for the bending samples, five profile lines were used to accommodate the lower number of cracks at the beginning of the experiments. The areas chosen for surface damage evaluation were positioned in the bent area, centered directly under the grips, which exhibited higher damage densities than the areas further away from the grips [17] due to inhomogeneous damage evolution [16,17]. The sizes of the evaluated areas were roughly 630 × 700 µm². After the bending experiments SEM micrographs to complement the CLSM images were recorded.

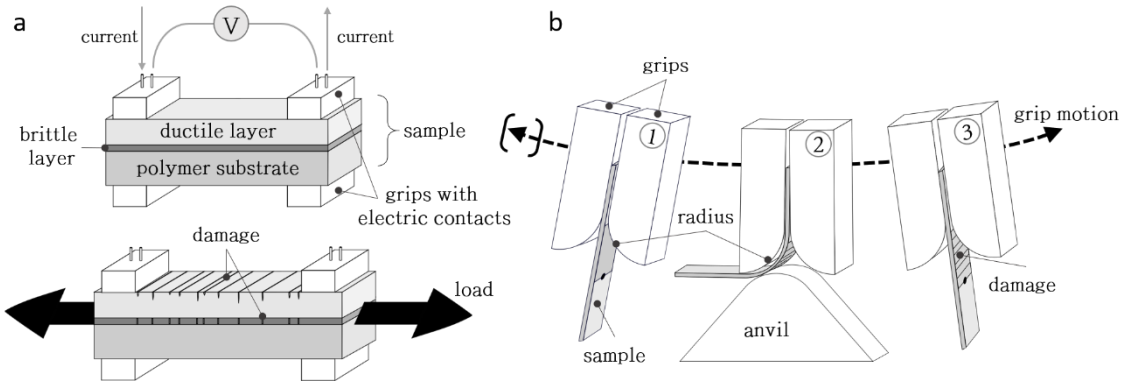

Fig. 8.1 (a) Scheme of the uniaxial tensile test with in situ 4PP resistance measurements. (b) Scheme of the cyclic bending procedure, adapted from [17]. The type of bending strain (tensile or compressive) depends on the direction of movement of the grips (left or right, i.e. clock- or counterclockwise).

8.3 RESULTS

8.3.1 MONOTONIC UNIAXIAL TENSILE TESTS

The COS of the Al/Mo-Ta bilayers increased with higher bilayer thickness ratios, as displayed in Fig. 8.2. The same behavior was observed for previously studied Al/Mo bilayers [15] with the same layer thicknesses and the data were added to Fig. 8.2. The comparison between Al/Mo-Ta and Al/Mo bilayers shows increased COS for Al/Mo-Ta bilayers with the same respective thickness ratios as the Al/Mo bilayers.

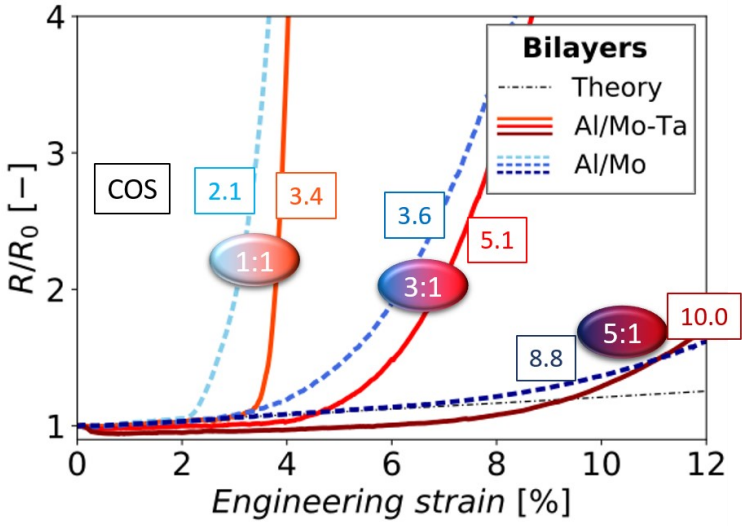

Fig. 8.2 Representative curves of the normalized electrical resistance (R/R_0) vs. engineering strain of Al/Mo-Ta and Al/Mo [15] bilayers obtained by *in situ* uniaxial tests. The values in the rectangular boxes denominate the respective average COS of the bilayers. The theory line was calculated after Eq. 3.2.

The CLSM surface images of the Al/Mo-Ta bilayers after strainng in Fig. 8.3a-c show long and straight cracks, typical for brittle fracture behavior such as in Mo films [42]. Similar to previously studied Al/Mo bilayers [15] (Fig. 8.3d-f), the fracture behavior of the Al/Mo-Ta bilayers is dominated by the brittle 30 nm thick Mo-Ta interlayer. Comparing the different thickness ratios of the Al/Mo-Ta bilayers reveals slight changes in the crack morphology with increasing Al layer thickness. In Fig. 8.3a (1:1 ratio) the cracks are perfectly straight lines, while in Fig. 8.3b-c (3:1 and 5:1 ratio) the cracks become slightly more wavy and shorter, due to the influence of the thicker and more ductile Al layers. A similar behavior is displayed in the Al/Mo bilayers in Fig. 8.3d-f. The characterization of the Al/Mo-Ta bilayer surface damage yielded average crack spacings of 3.3 ± 0.2, 4.2 ± 0.2 and 4.2 ± 0.2 µm for the respective thickness ratios 1:1, 3:1 and 5:1. Hence, these crack spacings are larger compared to the Al/Mo bilayers with the respective thickness ratios [15], as stated in Fig. 8.3d-f.

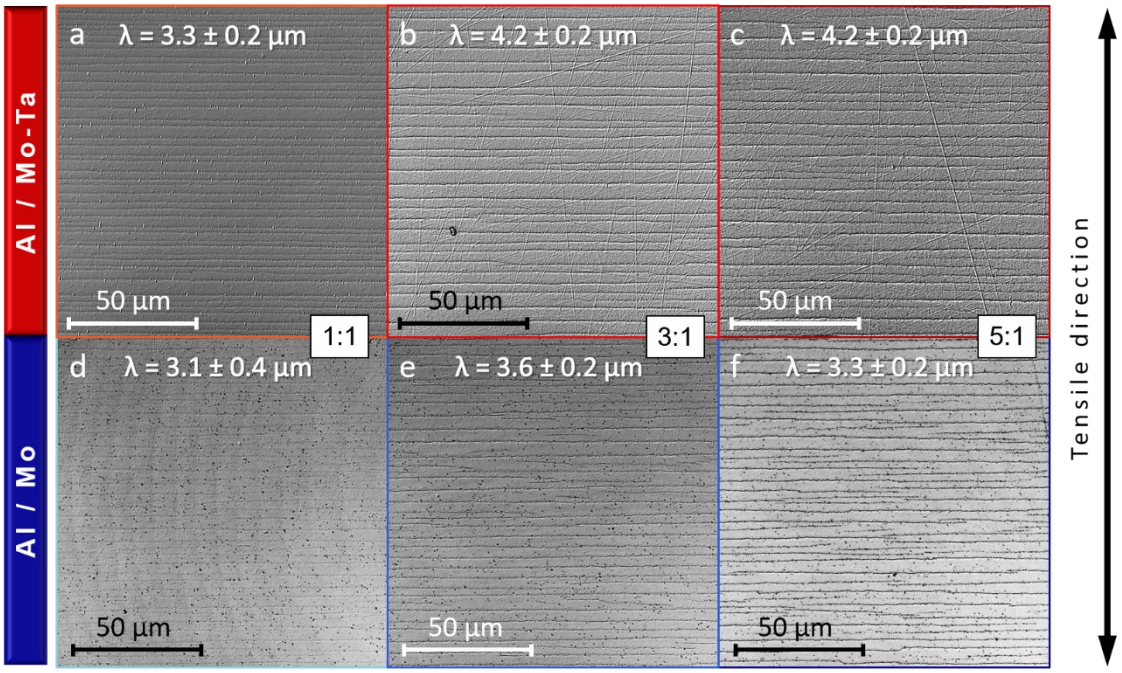

Fig. 8.3 Representative CLSM images of uniaxial tensile strained Al/Mo-Ta bilayers (a-c) and Al/Mo bilayers (d-f) [15] with different bilayer thickness ratios. The value λ at the upper edge displays the average crack spacing.

8.3.2 CYCLIC BENDING TESTS

As shown in Fig. 8.4a, the average normalized electrical resistance of the Al/Mo-Ta bilayers did not reveal much change before reaching 1 k bending cycles and then continuously increase until the end of the experiment at 50 k bending cycles. The

average R/R_0 behavior of the different Al/Mo-Ta bilayer thickness ratios in Fig. 8.4a match well with each other. During inspection of an Al/Mo-Ta 1:1 sample after 1 k cycles, an externally induced scratch was found opposite to the grip at the border of the bent area, leading to higher average R/R_0 values and error bars in Fig. 8.4a. The Al/Mo-Ta bilayers after 50 k cycles under 1.3% mixed bending strain showed average R/R_0 changes in the range of 25% and almost no detectable changes in surface damage density (Fig. 8.4).

The damage density, displayed in Fig. 8.4b, showed no statistically relevant changes after 50 k bending cycles and reached a maximum value of 0.0018 μm^{-1} for the Al/Mo-Ta 5:1 samples. The relatively high deviations are due to the low number of observable cracks. Representative CLSM images after 20 k cycles under 1.3% bending strain of the Al/Mo-Ta bilayers in Fig. 8.5a-c with additional information on the average crack spacings, λ, illustrate the absence of cracks. In Fig. 8.5b-c, random visible line patterns are caused by scratches on the substrates prior to deposition and have not been found to influence the fracture behavior of the Al/Mo-Ta bilayers.

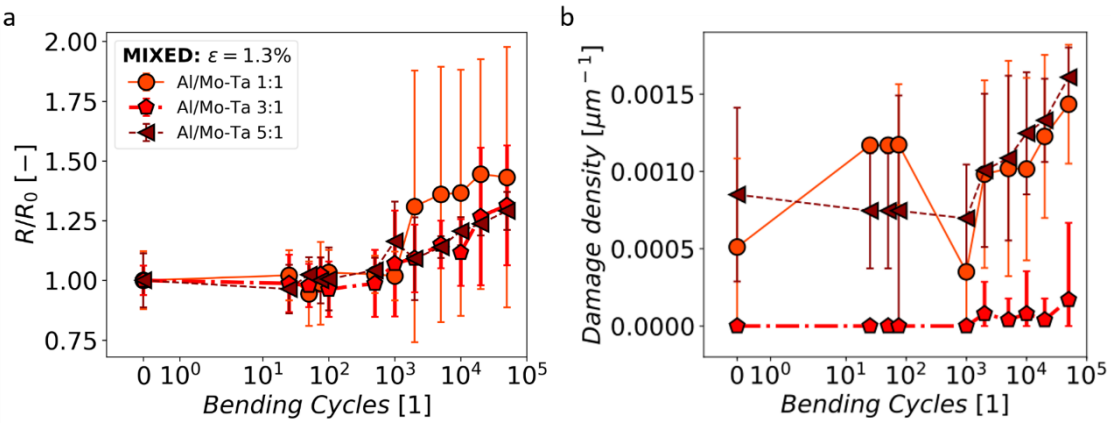

Fig. 8.4 Cyclically bent Al/Mo-Ta bilayers under 1.3% mixed bending strain: (a) average R/R_0 and (b) average damage density from 0 to 50 k cycles for three samples tested for each condition. The lines are only to guide the eyes. Note the logarithmic scale of the bending cycles.

The comparison of the surface damage of Al/Mo-Ta and the previously studied Al/Mo [17] bilayers after 20 k bending cycles under 1.3% bending strain in Fig. 8.5 clearly evidences the superior performance of the new Al/Mo-Ta bilayers over Al/Mo bilayers [17]. Previously studied Al/Mo bilayers in Fig. 8.5d-f experience 40 to 100 times higher R/R_0 ratios and numerous cracks [17], compared to the corresponding Al/Mo-Ta bilayers after 20 k cycles. Even at 50 k bending cycles under 1.3% bending strain, the Al/Mo-Ta bilayers experience little change in R/R_0 and surface damage.

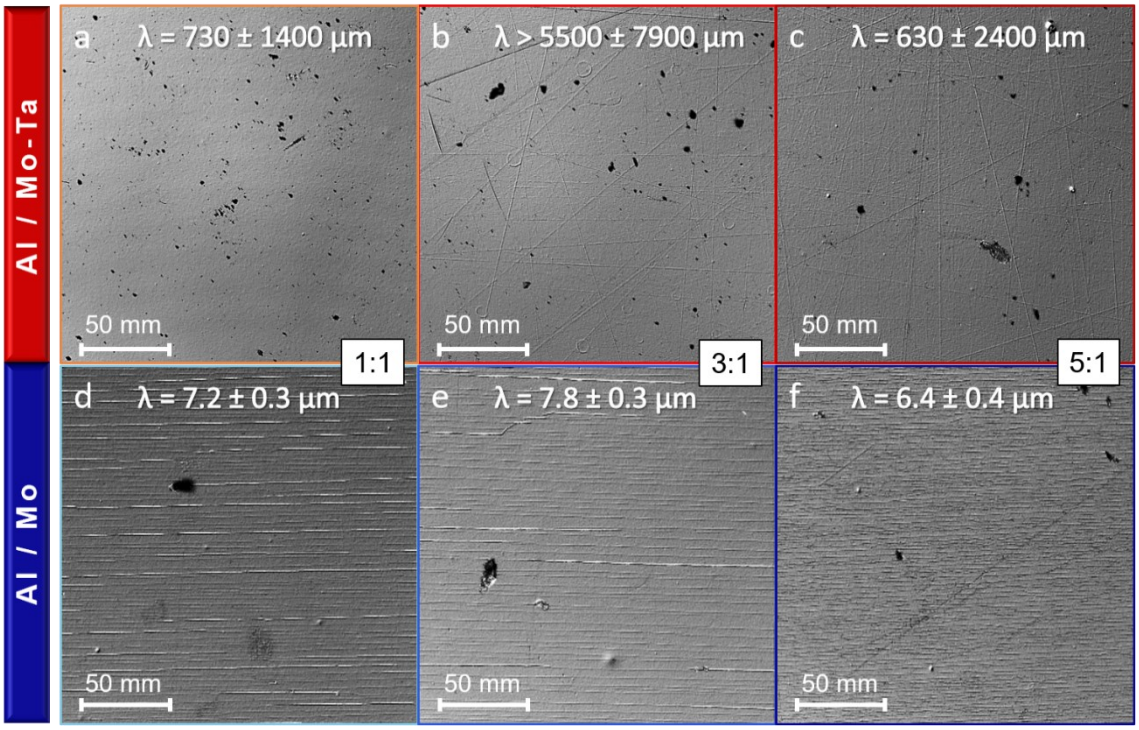

Fig. 8.5 Representative CLSM images of cyclically bent Al/Mo-Ta (a-c) and Al/Mo (d-f) [17] bilayers after 20 k cycles under 1.3% mixed bending strain. The average crack spacings, λ, of the bilayers are noted in the images.

At 3.1% bending strain, an increase of more than a factor of two compared to the 1.3% bending strain, the Al/Mo-Ta bilayers experience early electrical failure illustrated by increasing R/R_0 multiple times its original value and the formation of cracks (Fig. 8.6). The R/R_0 values were at some points during the experiments not measurable due to the limit of the digital multimeter in the range of 120 MΩ, indicating the following electrical overflow error and marked with a green cross at the last measured value in Fig. 8.6. For the 1:1 ratio two out of three, and for the 3:1 and 5:1 ratios one sample each experienced an overflow error. At 50 k bending cycles, the only measurable Al/Mo-Ta 1:1 sample reached $R/R_0 = 250$. Furthermore, the average measurable R/R_0 values for the 3:1 and 5:1 ratios at 50 k cycles are 700 and 15, respectively. Comparing the results in Fig. 8.6a-c, higher thickness ratios (equals thicker Al layers) yield lower electrical resistance and help to reduce the chances of an error of the bilayers during cyclic bending.

In contrast to the electrical measurements (Fig. 8.6a-c), the damage densities in Fig. 8.6d-f show a more uniform behavior. Samples that reached an electrical overflow error did not distinguish themselves in damage density, emphasizing the importance of accompanying electrical measurements to visual inspection for bending tests. The damage densities of the Al/Mo-Ta 5:1 thickness ratios at 3.1% bending strain start to

saturate around 10 k bending cycles (Fig. 8.6f, note the logarithmic scale of the bending cycles) and the damage densities are comparable to Al/Mo bilayers measured under similar conditions from a previous study [17]. However, the individual Al/Mo-Ta bilayer samples with 5:1 ratio show greater disparity than the other two thickness ratios. The disparity in Fig. 8.6f is caused by accumulations of relatively fine and short cracks in the range of several µms between the larger and straight cracks (Fig. 8.7c). The visibility of the fine cracks on the CLSM images was poor and led to differing results during the determination of the damage density for the Al/Mo-Ta 5:1 ratio. In Fig. 8.7, representative CLSM images of the Al/Mo-Ta bilayers show, similar to Fig. 8.3a-c, a transition from long straight to shorter and slightly wavy crack patterns. SEM micrographs of the Al/Mo-Ta bilayers revealed the aforementioned fine and short cracks between the larger cracks for the 5:1 bilayer thickness ratio (Fig. 8.7c), indicating a more ductile behavior of the bilayer. Such small crack accumulations were not found on the Al/Mo-Ta bilayers with 1:1 and 3:1 ratio. For the damage evolution in Fig. 8.6, only the CLSM images were used in order to compare all samples on the same length scale. The shorter cracks observed with SEM most likely are not TTCs, thus do not significantly influence the resistance measurements.

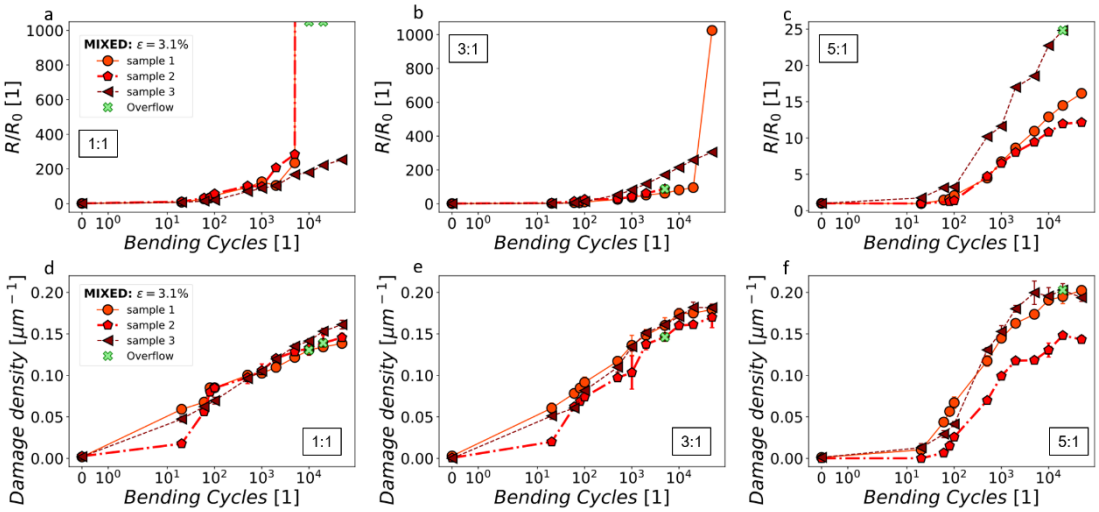

Fig. 8.6 Individual sample results for the cyclically bent Al/Mo-Ta bilayers under 3.1% mixed bending strain: (a-c) R/R_0 and (d-f) damage density from 0 to 50 k cycles for 1:1, 3:1, and 5:1 Al/Mo-Ta thickness ratios, respectively. The lines are only to guide the eyes. Note the logarithmic scale of the bending cycles.

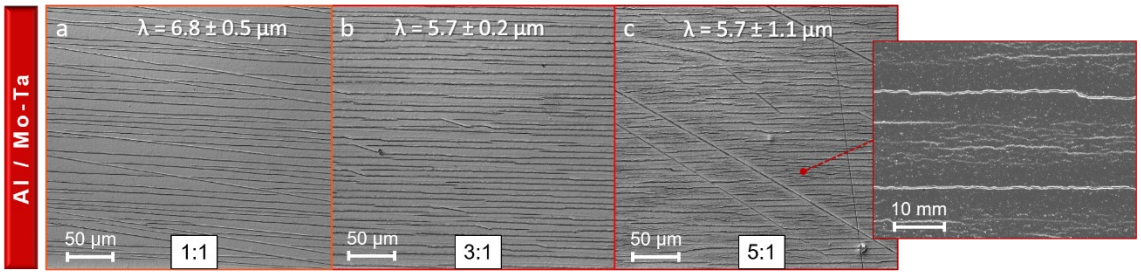

Fig. 8.7 Representative CLSM images of cyclically bent Al/Mo-Ta bilayers (a-c) with different bilayer thickness ratios after 50 k cycles under 3.1% mixed bending strain. The average crack spacings, λ, of the bilayers are noted at the top of the images. The inset SEM micrograph in (c) shows the accumulations of short wavy not TTCs between the larger through thickness straight cracks observed in CLSM images.

8.4 DISCUSSION

In our previous study [45], 50 nm thick Mo-Ta alloy films with 50 at.% Ta (COS ~ 2.4%), deposited with the same deposition parameters as 50 nm thick Mo films (COS ~ 1.1%), showed roughly a factor of two times higher COS. Within the present work, 50 nm thick Mo-Ta alloy films with 50 at.% Ta on 50 µm thick PI, deposited under the same conditions as in the Al/Mo-Ta bilayers, yielded an average COS of 2.8%. The higher COS of the Mo-Ta alloy film in the current study is caused by slightly different deposition parameters leading to higher compressive residual stresses in the Mo-Ta alloy film. A higher compressive stress ensures a higher resistance to cracking under tensile loads, as was demonstrated by Jörg et al. [42] for Mo films. The use of Mo-Ta interlayers instead of Mo interlayers shows not only better performance in crack resistance; the addition of Ta has been demonstrated to increase the interface strength [45] and to hinder diffusion [36,189] as well.

In literature, the domination of brittle layers on the fracture behavior of thin film multilayers is frequently reported for uniaxial tensile tests [15,91,92,95]. Likewise, in the current study, the dominance of the brittle Mo-Ta interlayers with 50 at.% Ta on the fracture behavior of Al/Mo-Ta bilayers was confirmed under uniaxial tensile load. Thicker Al layers are able to suppress crack formation and elevate the COS, similar to previously reported Al/Mo bilayers [15]. However, the substitution of commonly used Mo with Mo-Ta interlayers demonstrates a further improvement of the bilayer's COS and illustrates a weak point for the Mo interlayer in flexible applications (Fig. 8.2 and 8.5). Compared to Al/Mo bilayers, the Al/Mo-Ta bilayers also have a higher adhesion energy to the PI substrate [45], similar sheet resistivities [15], higher COS (Fig. 8.2), and less surface damage (Fig. 8.3). Thus, the substitution of Mo with Mo-Ta interlayers

increases the performance and lifetime of Mo/Al/Mo multilayers for stretchable and stretch-to-connect electronic devices (i.e. under uniaxial straining).

Under 1.3% mixed bending strain, the Al/Mo-Ta bilayers showed an R/R_0 increase of about 25% after 50 k cycles, which would equal 34 daily folding cycles (folding equals opening and closing) for two years, while no statistically relevant increase in surface damage was detected (Fig. 8.4). The R/R_0 increase starts around 1 k cycles and is probably caused by fatigue damage. Al/Mo-Ta bilayers stay undamaged and experience a relatively small R/R_0 increase, compared to cyclically bent Al/Mo bilayers [17] with corresponding bilayer thickness ratios and under the same mixed bending strain of 1.3%. These results emphasize the potential benefits of Mo-Ta compared to Mo interlayers in flexible display applications, such as foldable smartphones. Normally, an increase of 25% in the R/R_0 has been considered as the failure criteria [156,206,207] for cyclic tensile or bending tests. In the cited studies [156,206,207], mechanical damage (TTCs) were observed. For the Al/Mo-Ta bilayers no mechanical damage was observed indicating that mechanically no failure has occurred. Thus, there is still a necessity to clarify failure criteria for flexible material systems that use both the change in resistance as well as the amount and type of mechanical damage.

At 3.1% mixed bending strain, all Al/Mo-Ta bilayers experience fracture (Fig. 8.7). The range of the damage densities for tested Al/Mo-Ta bilayers is very similar to the previously tested Al/Mo bilayers [17] under the same conditions. It should be noted that the 3.1% applied bending strain is likely higher than the COS of the 30 nm thick Mo-Ta interlayers. For 50 nm thick Mo-Ta alloy films with 50 at.% Ta the COS was 2.8%, evaluated with uniaxial straining. This is most likely the main factor for the film fracture and electrical failure of the Al/Mo-Ta bilayers. Under 1.3% bending strain, Al/Mo-Ta bilayers are superior to Al/Mo bilayers with only a small increase in COS.

Compared to the previously studied Al/Mo bilayers [15–17], the Al/Mo-Ta bilayers subjected to 1.3% bending strain can be considered a successful improvement, while at 3.1% the Al/Mo-Ta bilayers perform worse. Delaying the formation of damage in the bent bilayers seems to eventually lead to an even harsher failure. Comparing with test conditions for foldable TFT displays in literature [27,31], where bending strains hardly exceed 1.3%, the performance of the Al/Mo-Ta bilayers can be considered very good at 1.3% bending strain and represent a step in the right direction. In addition, substitution of Mo films with Mo-Ta alloys is preferable, if the integration in the manufacturer's process chain is possible.

8.5 CONCLUSIONS

A new Mo-Ta interlayer, with compressive residual stresses, was developed to substitute Mo in Mo/Al/Mo multilayers, which are commonly used as electrodes in TFT displays [32]. Uniaxial tensile and cyclic bending tests showed that changing the material system of the interlayer enables a path to improve the performance and lifetime of flexible electronic devices. The crack onset strain of simplified Al/Mo-Ta bilayer samples increased under uniaxial tensile loads, compared with Al/Mo bilayers [15]. Under 1.3% bending strain, for 50 k bending cycles almost no surface damage was observed on the Al/Mo-Ta bilayers and the R/R_0 increased by 25%, which is relatively low compared to Al/Mo bilayers, which had 40 to 100 times higher values for R/R_0. Under 3.1% bending strain, the Al/Mo-Ta bilayers fracture and the R/R_0 reached very high values. The difference in electro-mechanical behavior warrant further study into determining failure criteria for these experimental setups that take both the mechanical damage and the electrical resistance into account rather than one or the other. The new Mo-Ta interlayers with 50 at.% Ta are more suitable for stretching and folding applications than Mo interlayers. Especially, for foldable TFT displays the Al/Mo-Ta bilayers tested at 1.3% bending strain correspond well to current industrial demands.

9 CONCLUSIONS AND OUTLOOK

Many released prototypes of portable flexible electrical devices have shown their potential in a wide range of fields, such as sports, entertainment, medicine and transportation. Often, a smart design and film architecture can alleviate the load conditions on the device, however, at some point the demands for device flexibility outstrip the limits of those measures. The improvement and modification of key components, such as the electrodes of flexible devices, is the logical next step.

Electro-mechanical testing on Al/Mo bilayer systems, a simplified version of the commonly used Mo/Al/Mo electrode stack in TFT displays, allows the determination of their limits for flexible application (stretching and bending). The utilization of the inherently brittle Mo layers is necessary to maintain adhesion and to act as a diffusion barrier layer. The combination of a thin Mo layer ($\sim$30 nm) and a thick Al layer ($>$150 nm) yield higher failure strains and higher electrical conductivity. However, the Al/Mo bilayer systems do not fulfill the requirements for current industrial demands for materials to withstand 1% or more bending strain for thousands of bending cycles and failed before reaching one thousand bending cycles.

The early fracture of the Mo layer in the electrode stacks under load turned out to be the key issue. Mo-based alloys instead of the Mo layer in TFT electrodes were tested to minimize excessive changes in the current process chains of TFT displays and to maintain the diffusion barrier and adhesion properties of the Mo layer. Mo-Ta alloys showed higher failure strains and good conductivity compared to pure Mo and the other tested alloyed films. Bending tests at 1.3% bending strain with bilayers using the Mo-Ta alloy instead of the Mo layer (Al/Mo-Ta bilayer) experienced a 25% increase of electrical resistance (for Al/Mo bilayers >2,000%), while no surface damage up to 50,000 cycles was observed.

The results obtained in this work show the potential of other material systems and opens the path to more flexible electrical devices with less design restrictions in the future. Not only the development of new material systems for TFT electrodes, also the tuning of film thicknesses, microstructure and stresses will improve the electrode stack's robustness and lifetime.

APPENDIX A

Table A: Overview of monotonic uniaxial tensile tested alloy thin films with *in situ* 4PP measurements.

Film type	R_0 [Ω]	COS [%]	ρ [μΩcm]	Alloying content [at.%]
Mo-Ta, 500 nm thickness, 50 μm PI	1.8 ± 0.2	0.27 ± 0.00	27.6 ± 2.5	0
	2.0 ± 0.0	0.36 ± 0.01	27.4 ± 0.2	10
	2.2 ± 0.1	0.51 ± 0.01	30.1 ± 0.8	20
	2.5 ± 0.0	0.71 ± 0.02	34.3 ± 0.2	30
	2.6 ± 0.1	0.88 ± 0.00	35.7 ± 0.4	40
	3.1 ± 0.0	1.14 ± 0.04	41.8 ± 0.1	50
	3.2 ± 0.1	1.10 ± 0.04	44.4 ± 0.9	60
	3.3 ± 0.1	1.32 ± 0.06	45.3 ± 1.2	70
	2.8 ± 0.1	1.54 ± 0.01	38.1 ± 0.5	80
Film type	**R_0 [Ω]**	**COS [%]**	**ρ [μΩcm]**	**Alloying content [at.%]**
Mo-Ta, 50 nm thickness, 50 μm PI	29.2 ± 0.1	1.06 ± 0.07	39.6 ± 0.1	0
	25.3 ± 1.8	1.12 ± 0.20	34.3 ± 2.2	10
	34.2 ± 0.5	1.11 ± 0.01	46.3 ± 0.7	20
	35.5 ± 0.9	1.7 ± 0.21	47.7 ± 1.1	30
	37.9 ± 0.7	2.23 ± 0.03	51.1 ± 0.8	40
	42.9 ± 0.9	2.37 ± 0.17	57.8 ± 1.4	50
	44.3 ± 0.7	2.9 ± 0.04	61.0 ± 0.3	60
	46.3 ± 0.4	2.38 ± 0.07	65.4 ± 0.9	70
	43.6 ± 0.3	2.48 ± 0.01	60.3 ± 1.0	80
	40.3 ± 0.1	3.17 ± 0.01	56.1 ± 0.6	90
Film type	**R_0 [Ω]**	**COS [%]**	**ρ [μΩcm]**	**Alloying content [at.%]**
Mo-Al, 500 nm thickness, 50 μm PI	1.8 ± 0.2	0.27 ± 0.00	27.6 ± 2.5	0
	8.6 ± 0.9	0.21 ± 0.00	112.5 ± 11.5	12
	13.4 ± 0.2	0.42 ± 0.00	171.4 ± 1.0	24
	19.9 ± 0.7	0.52 ± 0.00	225.3 ± 10.0	34
	17.9 ± 0.6	1.22 ± 0.00	238.7 ± 4.2	45
	18.2 ± 0.2	2.46 ± 0.00	241.3 ± 1.2	48
Film type	**R_0 [Ω]**	**COS [%]**	**ρ [μΩcm]**	**Alloying content [at.%]**
Mo-Al, 50 nm thickness, 50 μm PI	29.2 ± 0.1	1.06 ± 0.07	39.6 ± 0.1	0
	70.3 ± 0.6	1.1 ± 0.03	102.1 ± 0.5	10
	106.9 ± 1.7	1.37 ± 0.14	155.0 ± 4.5	20
	133.9 ± 1.2	2.12 ± 0.23	197.9 ± 1.1	30
	189.2 ± 3.8	1.34 ± 0.21	271.2 ± 3.2	40
	185.8 ± 4.3	2.33 ± 0.13	271.3 ± 6.7	50

Film type	R_0 [Ω]	COS [%]	ρ [μΩcm]	Alloying content [at.%]
Mo-Al, 500 nm thickness, 75 μm PI	29.2 ± 0.1	1.06 ± 0.07	39.6 ± 0.1	0
	81.7 ± 1.2	1.19 ± 0.11	108.6 ± 1.9	10
	127.1 ± 4.6	1.32 ± 0.01	170.6 ± 3.0	20
	151.4 ± 2.0	1.7 ± 0.37	203.9 ± 1.6	30
	175.3 ± 2.2	1.8 ± 0.03	236.1 ± 1.7	40
	206.3 ± 9.1	2.51 ± 0.16	279.0 ± 1.9	50
Film type	**R_0 [Ω]**	**COS [%]**	**ρ [μΩcm]**	**Alloying content [at.%]**
Mo-Al, 50 nm thickness, 125 μm PI	29.2 ± 0.1	1.06 ± 0.07	39.6 ± 0.1	0
	86.2 ± 4.1	0.66 ± 0.18	122.6 ± 0.3	10
	110.8 ± 7.8	1.26 ± 0.17	167.2 ± 7.7	20
	144.0 ± 1.6	0.68 ± 0.00	211.6 ± 0.9	30
	172.6 ± 4.2	0.82 ± 0.06	255.0 ± 5.0	40
	225.1 ± 3.2	2.38 ± 0.06	333.3 ± 0.0	50
Film type	**R_0 [Ω]**	**COS [%]**	**ρ [μΩcm]**	**Alloying content [at.%]**
Mo-In, 500 nm thickness, 50 μm PI	1.8 ± 0.2	0.27 ± 0.00	27.6 ± 2.5	0
	208.5 ± 97.6	0.58 ± 0.07	2857.8 ± 1325.2	10
	379.7 ± 218.1	1.34 ± 0.56	5147.0 ± 2138.3	15
	21.1 ± 0.6	0.53 ± 0.03	292.4 ± 10.1	20
	11.8 ± 0.7	0.24 ± 0.04	153.0 ± 4.8	25
	22.1 ± 0.6	1.03 ± 0.02	283.8 ± 3.2	30
	35.9 ± 3.6	0.31 ± 0.01	468.0 ± 43.3	35
Film type	**R_0 [Ω]**	**COS [%]**	**ρ [μΩcm]**	**Alloying content [at.%]**
Mo-Sn, 500 nm thick, 50 μm PI	1.8 ± 0.2	0.27 ± 0.00	27.6 ± 2.5	0
	8.5 ± 0.2	0.49 ± 0.01	110.3 ± 1.4	9
	38.3 ± 13.3	0.22 ± 0.04	522.6 ± 187.4	18
	15.1 ± 0.4	0.78 ± 0.07	212.0 ± 4.4	50
	0.3 ± 0.0	NaN ± Nan	21.8 ± 0.4	100
Film type	**R_0 [Ω]**	**COS [%]**	**ρ [μΩcm]**	**Alloying content [at.%]**
Mo-Mg, 500 nm thick, 50 μm PI	1.81 ± 0.2	0.27 ± 0.00	27.6 ± 2.5	0
	2.2 ± 0.0	0.33 ± 0.14	14.9 ± 0.3	3
	5.3 ± 0.2	0.22 ± 0.02	66.4 ± 3.2	7
	1.4 ± 0.0	0.48 ± 0.00	18.7 ± 0.0	83
	0.1 ± 0.0	0.63 ± 0.25	10.1 ± 0.7	100

Film type	R_0 [Ω]	COS [%]	ρ [μΩcm]	Alloying content [at.%]
Mo-Nb, 50 nm , 50 μm PI	29.2 ± 0.1	1.06 ± 0.07	39.6 ± 0.1	0
	44.3 ± 18.8	0.3 ± 0.03	62.0 ± 25.8	10
	38.4 ± 2.8	0.62 ± 0.04	53.3 ± 3.4	50
	43.0 ± 2.4	1.31 ± 0.01	59.6 ± 3.1	90
Film type	**R_0 [Ω]**	**COS [%]**	**ρ [μΩcm]**	**Alloying content [at.%]**
Mo 30 nm, 50 μm PI	183.7 ± 0.0	1.49 ± 0.00	25.8 ± 0.0	0

Table B: Overview of monotonic uniaxial tensile tested 50 nm thick Mo-Ta alloys with modified residual stresses on 50 μm thick PI substrates with *in situ* 4PP measurements.

Film type	R_0 [Ω]	COS [%]	ρ [μΩcm]	Alloying content [at.%]	Residual stresses [GPa]
Mo-Ta 1P - 500 nm, 50 μm PI	2.8 ± 0.0	1.05 ± 0.08	38.9 ± 0.4	47	-1.5
Mo-Ta 1P - 275 nm, 50 μm PI	5.5 ± 0.2	1.55 ± 0.00	41.5 ± 1.6	47	-1.5
Mo-Ta 1P - 50 nm, 50 μm PI	40.2 ± 0.1	2.49 ± 0.16	54.4 ± 1.4	47	-1.5
Mo-Ta 2P - 500 nm, 50 μm PI	2.7 ± 0.0	1.3 ± 0.03	36.2 ± 0.6	50	-1.9
Mo-Ta 2P - 275 nm, 50 μm PI	6.1 ± 0.1	1.57 ± 0.05	45.3 ± 0.7	50	-1.9
Mo-Ta 2P - 50 nm, 50 μm PI	38.9 ± 1.2	2.75 ± 0.07	53.4 ± 1.1	50	-1.9

Table C: Overview of monotonic uniaxial tensile tested multilayer stacks on 50 μm thick PI with *in situ* 4PP measurements. The denomination "Gr" stands for a gradient layer.

Film type	R_0 [Ω]	COS [%]	ρ [μΩcm]	Layer thicknesses [nm]
Cu/Mo - PI	0.3 ± 0.0	6.5 ± 0.9	3.6 ± 0.1	280/30
Mo/Cu/Mo - PI	0.5 ± 0.0	3.8 ± 0.3	5.5 ± 0.4	30/370/30
Mo/Gr/Cu/Gr/Mo - PI	0.3 ± 0.0	5.7 ± 1.0	2.7 ± 0.1	30/50/230/50/30
Mo/Al/Mo - PI	0.6 ± 0.0	NaN ± NaN	6.2 ± 0.1	30/300/30
Mo/Gr/Al/Gr/Mo - PI	2.0 ± 0.0	2.4 ± 0.1	12.3 ± 0.1	20/20/110/20/20
Al/Mo - PI	0.6 ± 0.0	NaN ± NaN	7.0 ± 0.1	340/30
Al/Mo - PI	1.1 ± 0.0	8.81 ± 0.66	6.0 ± 0.2	150/30
Al/Mo - PI	2.4 ± 0.1	3.6 ± 0.38	7.3 ± 0.3	75/30
Al/Mo - PI	7.8 ± 0.3	2.1 ± 0.22	13.5 ± 0.8	30/30
Mo/Al - PI	9.2 ± 0.1	2.05 ± 0.03	16.1 ± 0.4	30/30

REFERENCES

[1] H.L. Tuller, W. S.Wong, A. Salleo, Flexible Electronics : Materials and Applications (Electronic Materials : Science and Technology), 2009. doi:10.1007/978-0-387-74363-9.

[2] A. Nathan, B.R. Chalamala, Special issue on flexible electronics technology, Part 1: Systems and applications, Proc. IEEE. 93 (2005) 1235–1237. doi:10.1109/JPROC.2005.851525.

[3] A. Nathan, B.R. Chalamala, Flexible electronics technology, part II: Materials and devices, Proc. IEEE. 93 (2005) 1391–1393. doi:10.1109/JPROC.2005.851509.

[4] G.P. Crawford, ed., Flexible Flat Panel Displays, John Wiley & Sons, Ltd, Chichester, UK, 2005. doi:10.1002/0470870508.

[5] M. Kaltenbrunner, T. Sekitani, J. Reeder, T. Yokota, K. Kuribara, T. Tokuhara, M. Drack, R. Schwödiauer, I. Graz, S. Bauer-Gogonea, S. Bauer, T. Someya, An ultra-lightweight design for imperceptible plastic electronics, Nature. 499 (2013) 458–463. doi:10.1038/nature12314.

[6] T. Yokota, P. Zalar, M. Kaltenbrunner, H. Jinno, N. Matsuhisa, H. Kitanosako, Y. Tachibana, W. Yukita, M. Koizumi, T. Someya, Ultraflexible organic photonic skin, Sci. Adv. 2 (2016) e1501856–e1501856. doi:10.1126/sciadv.1501856.

[7] A. Pantelopoulos, N.G. Bourbakis, A survey on wearable sensor-based systems for health monitoring and prognosis, IEEE Trans. Syst. Man Cybern. Part C Appl. Rev. 40 (2010) 1–12. doi:10.1109/TSMCC.2009.2032660.

[8] B. Xu, A. Akhtar, Y. Liu, H. Chen, W.H. Yeo, S. Park, B. Boyce, H. Kim, J. Yu, H.Y. Lai, S. Jung, Y. Zhou, J. Kim, S. Cho, Y. Huang, T. Bretl, J.A. Rogers, An Epidermal Stimulation and Sensing Platform for Sensorimotor Prosthetic Control, Management of Lower Back Exertion, and Electrical Muscle Activation, Adv. Mater. 28 (2016) 4462–4471. doi:10.1002/adma.201504155.

[9] M. Jung, J. Kim, J. Noh, N. Lim, C. Lim, G. Lee, J. Kim, H. Kang, K. Jung, A.D. Leonard, J.M. Tour, G. Cho, All-Printed and roll-to-roll-printable 13.56-MHz-operated 1-bit RF tag on plastic foils, IEEE Trans. Electron Devices. 57 (2010) 571–580. doi:10.1109/TED.2009.2039541.

[10] A. Chirilă, S. Buecheler, F. Pianezzi, P. Bloesch, C. Gretener, A.R. Uhl, C. Fella, L. Kranz, J. Perrenoud, S. Seyrling, R. Verma, S. Nishiwaki, Y.E. Romanyuk, G. Bilger, A.N. Tiwari, Highly efficient Cu(In,Ga)Se2 solar cells grown on flexible polymer films, Nat. Mater. 10 (2011) 857–861. doi:10.1038/nmat3122.

[11] M.B. Schubert, J.H. Werner, Flexible solar cells for clothing, Mater. Today. 9 (2006) 42–50. doi:10.1016/S1369-7021(06)71542-5.

[12] LG Display, 18-inch Flexible OLED Panel, (2014). https://youtu.be/AxbHpXE4VM0%0A.

[13] PackNet, The barcode disappears! RFID mass printing technology development, (2010). http://www.packnet.co.kr/news/n_read.html?newsid=7793.

[14] Lenovo, Meet the World's First Foldable PC, (2019). https://youtu.be/_XBU_xxpsQk%0A.

[15] P. Kreiml, M. Rausch, V.L. Terziyska, H. Köstenbauer, J. Winkler, C. Mitterer, M.J.

Cordill, Electro-mechanical behavior of Al/Mo bilayers studied with in situ straining methods, Thin Solid Films. 665 (2018) 131–136. doi:10.1016/J.TSF.2018.07.054.

[16] P. Kreiml, M. Rausch, V.L. Terziyska, J. Winkler, C. Mitterer, M.J. Cordill, Compressive and tensile bending of sputter deposited Al/Mo bilayers, Scr. Mater. 162 (2019) 367–371. doi:10.1016/j.scriptamat.2018.11.048.

[17] P. Kreiml, M. Rausch, V.L. Terziyska, H. Köstenbauer, J. Winkler, C. Mitterer, M.J. Cordill, Correlation of mechanical damage and electrical behavior of Al/Mo bilayers subjected to bending, Thin Solid Films. 687 (2019) 137480. doi:10.1016/j.tsf.2019.137480.

[18] H.E. Lee, J.H. Shin, J.H. Park, S.K. Hong, S.H. Park, S.H. Lee, J.H. Lee, I. Kang, K.J. Lee, Micro Light-Emitting Diodes for Display and Flexible Biomedical Applications, Adv. Funct. Mater. 29 (2019) 1808075. doi:10.1002/adfm.201808075.

[19] S. Wagner, H. Gleskova, I.C. Cheng, J.C. Sturm, Z. Suo, Mechanics of TFT Technology on Flexible Substrates, Flex. Flat Panel Displays. 1 (2005) 263–283. doi:10.1002/0470870508.ch14.

[20] T. Xiao, G. Yu, C.-L. Shieh, J.-W. Park, F. Foong, K. Lee, J. Musolf, G. Wang, K. Ottoson, K. Yang, J. Wang, B. Berkoff, B. Nilsson, Metal Oxide TFT Turnkey Manufacturing Solution for a-Si TFT Lines, SID Symp. Dig. Tech. Pap. 47 (2016) 318–321. doi:10.1002/sdtp.10664.

[21] J.A. Cunningham, C.R. Fuller, R.C. Hooper, R.H. Wakefield, Metallization system for semiconductors, US Patent 3,654,526, 1972.

[22] B.-K. Kim, H.-S. Park, J.-H. Choung, S.-Y. Hong, L. Ji-Sun, B.-J. Lee, K.-J. Baek, T.-H. Rhee, Y.-S. Song, Etchant composition, patterning conductive layer and manufacturing flat panel, display device using the same, US Patent 7,985,982, 2011.

[23] T. Zyung, Seong Hyun Kim, Hye Yong Chu, Jung Hun Lee, Sang Chul Lim, Jeong-Ik Lee, Jiyoung Oh, Flexible Organic LED and Organic Thin-Film Transistor, Proc. IEEE. 93 (2005) 1265–1272. doi:10.1109/JPROC.2005.850303.

[24] M. Ikeda, TFT-LCD Gate and Data Bus-Line Design and Process Technologies, SID (Society Inf. Display) Int. Symp. Dig. Tech. Pap. 26 (1995) 11–14. https://ci.nii.ac.jp/naid/10006483671/#cit.

[25] H. Kitahara, E. Colgan, K. Schleupen, 48.1: Invited Paper: Technology Trend of Large Size and High Resolution Direct-View TFT-LCD, SID Symp. Dig. Tech. Pap. 31 (2000) 1108. doi:10.1889/1.1832858.

[26] T. Ueki, Requirements for large-sized high-resolution TFT-LCDs, J. Soc. Inf. Disp. 9 (2001) 151–154. doi:10.1889/1.1828780.

[27] J. Sheng, H.J. Jeong, K.L. Han, T.H. Hong, J.S. Park, Review of recent advances in flexible oxide semiconductor thin-film transistors, J. Inf. Disp. 18 (2017) 159–172. doi:10.1080/15980316.2017.1385544.

[28] D.-U. Jin, T.-W. Kim, H.-W. Koo, D. Stryakhilev, H.-S. Kim, S.-J. Seo, M.-J. Kim, H.-K. Min, H.-K. Chung, S.-S. Kim, 47.1: Invited Paper: Highly Robust Flexible AMOLED Display on Plastic Substrate with New Structure, SID Symp. Dig. Tech. Pap. 41 (2010) 703. doi:10.1889/1.3500565.

[29] S. Li, X. Liu, R. Li, Y. Su, Shear deformation dominates in the soft adhesive layers of the laminated structure of flexible electronics, Int. J. Solids Struct. 110–111

(2017) 305–314. doi:10.1016/j.ijsolstr.2016.12.006.
[30] M. Nishimura, K. Takebayashi, M. Hishinuma, H. Yamaguchi, A. Murayama, A 5.5-inch full HD foldable AMOLED display based on neutral-plane splitting concept, J. Soc. Inf. Disp. 27 (2019) 480–486. doi:10.1002/jsid.796.
[31] J. Sheng, J. Park, D. won Choi, J. Lim, J.S. Park, A Study on the Electrical Properties of Atomic Layer Deposition Grown InOx on Flexible Substrates with Respect to N2O Plasma Treatment and the Associated Thin-Film Transistor Behavior under Repetitive Mechanical Stress, ACS Appl. Mater. Interfaces. 8 (2016) 31136–31143. doi:10.1021/acsami.6b11815.
[32] K. Onisawa, S. Takayama, Y. Shigesato, T. Takahashi, Thin Film Transistors, Springer US, Boston, MA, 2004. doi:10.1007/978-1-4615-0397-2.
[33] H.T.G. Hentzell, A. Robertsson, L. Hultman, G. Shaofang, S. -E. Hörnström, P.A. Psaras, Formation of aluminum silicide between two layers of amorphous silicon, Appl. Phys. Lett. 50 (1987) 933–934. doi:10.1063/1.97984.
[34] M. Mühlbacher, G. Greczynski, B. Sartory, F. Mendez-Martin, N. Schalk, J. Lu, L. Hultman, C. Mitterer, TiN diffusion barrier failure by the formation of Cu 3 Si investigated by electron microscopy and atom probe tomography, J. Vac. Sci. Technol. B, Nanotechnol. Microelectron. Mater. Process. Meas. Phenom. 34 (2016) 022202. doi:10.1116/1.4942003.
[35] G.J. van Gurp, J.L.C. Daams, A. van Oostrom, L.J.M. Augustus, Y. Tamminga, Aluminum-silicide reactions. I. Diffusion, compound formation, and microstructure, J. Appl. Phys. 50 (1979) 6915–6922. doi:10.1063/1.325843.
[36] H. Ono, T. Nakano, T. Ohta, Diffusion barrier effects of transition metals for Cu/M/Si multilayers (M=Cr, Ti, Nb, Mo, Ta, W), Appl. Phys. Lett. 64 (1994) 1511–1513. doi:10.1063/1.111875.
[37] S. Lee, J. Shin, J. Jang, Top Interface Engineering of Flexible Oxide Thin-Film Transistors by Splitting Active Layer, Adv. Funct. Mater. 27 (2017) 1–9. doi:10.1002/adfm.201604921.
[38] S. Lee, Y. Chen, J. Kim, H. Kim, J. Jang, Highly robust oxide TFT with bulk accumulation and source/drain/active layer splitting, J. Soc. Inf. Disp. 27 (2019) 507–513. doi:10.1002/jsid.823.
[39] S. Wagner, S. Bauer, Materials for stretchable electronics, MRS Bull. 37 (2012) 207–213. doi:10.1557/mrs.2012.37.
[40] T. Li, Z. Suo, S.P. Lacour, S. Wagner, Compliant thin film patterns of stiff materials as platforms for stretchable electronics, J. Mater. Res. 20 (2005) 3274–3277. doi:10.1557/jmr.2005.0422.
[41] F. Bossuyt, T. Vervust, J. Vanfleteren, Stretchable electronics technology for large area applications: Fabrication and mechanical characterization, IEEE Trans. Components, Packag. Manuf. Technol. 3 (2013) 229–235. doi:10.1109/TCPMT.2012.2185792.
[42] T. Jörg, M.J. Cordill, R. Franz, O. Glushko, J. Winkler, C. Mitterer, The electro-mechanical behavior of sputter-deposited Mo thin films on flexible substrates, Thin Solid Films. 606 (2016) 45–50. doi:10.1016/j.tsf.2016.03.032.
[43] M.J. Cordill, T. Jörg, O. Glushko, R. Franz, C. Mitterer, Crack deflecting microstructure for improved electro-mechanical lifetimes of flexible systems, Mater. Lett. 244 (2019) 47–49. doi:10.1016/j.matlet.2019.02.039.
[44] T. Jörg, D. Music, F. Hauser, M.J. Cordill, R. Franz, H. Köstenbauer, J. Winkler,

J.M. Schneider, C. Mitterer, Deformation behavior of Re alloyed Mo thin films on flexible substrates : In situ fragmentation analysis supported by first-principles calculations, (2017) 1–10. doi:10.1038/s41598-017-07825-1.

[45] P. Kreiml, M. Rausch, V.L. Terziyska, H. Köstenbauer, J. Winkler, C. Mitterer, M.J. Cordill, Balancing the electro-mechanical and interfacial performance of Mo-based alloy films, Materialia. (2020) 100774. doi:10.1016/j.mtla.2020.100774.

[46] J.E. Greene, Tracing the 5000-year recorded history of inorganic thin films from ∼3000 BC to the early 1900s AD, Appl. Phys. Rev. 1 (2014) 041302. doi:10.1063/1.4902760.

[47] J.E. Greene, Review Article: Tracing the recorded history of thin-film sputter deposition: From the 1800s to 2017, J. Vac. Sci. Technol. A Vacuum, Surfaces, Film. 35 (2017) 05C204. doi:10.1116/1.4998940.

[48] D.M. Mattox, Handbook of Physical Vapor Deposition (PVD) Processing, Second Ed., William Andrew, 2010.

[49] P.M. Martin, Handbook of deposition technologies for films and coatings, Third Ed., Elsevier Inc., 2010.

[50] R.F. Bunshah, HANDBOOK OF DEPOSITION TECHNOLOGIES FOR FILMS AND COATINGS, Second Ed., Noyes, Mew Jersey, 1994.

[51] K. Seshan, Handbook of Thin Film Deposition Techniques Principles, Methods, Equipment and Applications, Second Editon, CRC Press, 2002. doi:10.1201/9781482269680.

[52] J.A. Venables, Introduction to Surface and Thin Film Processes, Cambridge University Press, 2000. doi:10.1017/CBO9780511755651.

[53] R.A. Powell, S. Rossnagel, PVD for Microelectronics: Sputter Deposition Applied to Semiconductor Manufacturing, Academic Press (1999).

[54] M. Ohring, Materials Science of Thin Films, Second Ed., Academic Press, 2001.

[55] W.D. Sproul, Multi-cathode unbalanced magnetron sputtering systems, Surf. Coatings Technol. 49 (1991) 284–289. doi:10.1016/0257-8972(91)90070-D.

[56] C.A. Bishop, Vacuum Deposition onto Webs, Films and Foils, Third Edit, William Andrew; Elsevier, 2015.

[57] W.P. Leroy, S. Konstantinidis, S. Mahieu, R. Snyders, D. Depla, Angular-resolved energy flux measurements of a dc- and HIPIMS-powered rotating cylindrical magnetron in reactive and non-reactive atmosphere, J. Phys. D. Appl. Phys. 44 (2011) 115201. doi:10.1088/0022-3727/44/11/115201.

[58] M. Rausch, A. Sabag, K.-H. Pichler, G.C. Gruber, J. Köstenbauer, H. Köstenbauer, P. Kreiml, M.J. Cordill, J. Winkler, C. Mitterer, The sputter performance of an industrial-scale planar Mo-target over its lifetime: Target erosion and film properties, Surf. Coatings Technol. 381 (2020) 125174. doi:10.1016/j.surfcoat.2019.125174.

[59] D. Depla, J. Haemers, G. Buyle, R. De Gryse, Hysteresis behavior during reactive magnetron sputtering of Al2O3 using a rotating cylindrical magnetron, J. Vac. Sci. Technol. A Vacuum, Surfaces, Film. 24 (2006) 934–938. doi:10.1116/1.2198870.

[60] J. Sarkar, Sputtering Materials for VLSI and Thin Film Devices, William Andrew; Elsevier, 2013.

[61] P.. Kelly, R.. Arnell, Magnetron sputtering: a review of recent developments and applications, Vacuum. 56 (2000) 159–172. doi:10.1016/S0042-207X(99)00189-X.

[62] M. Rausch, M. Pavlovič, P. Kreiml, M.J. Cordill, J. Winkler, C. Mitterer, Sputter deposition of Mo-based multicomponent thin films from rotatable targets: Experiment and simulation, Appl. Surf. Sci. 455 (2018) 1029–1036. doi:10.1016/j.apsusc.2018.06.012.
[63] K. Van Aeken, S. Mahieu, D. Depla, The metal flux from a rotating cylindrical magnetron: a Monte Carlo simulation, J. Phys. D. Appl. Phys. 41 (2008) 205307. doi:10.1088/0022-3727/41/20/205307.
[64] M. Rausch, S. Mráz, P. Kreiml, M.J. Cordill, J.M. Schneider, J. Winkler, C. Mitterer, Angular resolved mass-energy analysis of species emitted from a dc magnetron sputtered NiW-target, J. Vac. Sci. Technol. A. 38 (2020) 023401. doi:10.1116/1.5138248.
[65] M. Rausch, M. Golizadeh, P. Kreiml, M.J. Cordill, J. Winkler, C. Mitterer, Sputter deposition of NiW films from a rotatable target, Appl. Surf. Sci. 511 (2020) 145616. doi:10.1016/j.apsusc.2020.145616.
[66] Z. Zhang, M.G. Lagally, Atomistic Processes in the Early Stages of Thin-Film Growth, Science (80-.). 276 (1997) 377–383. doi:10.1126/science.276.5311.377.
[67] A. Anders, A structure zone diagram including plasma-based deposition and ion etching, Thin Solid Films. 518 (2010) 4087–4090. doi:10.1016/j.tsf.2009.10.145.
[68] B.A. Movchan, A. V Demchishin, STRUCTURE AND PROPERTIES OF THICK CONDENSATES OF NICKEL, TITANIUM, TUNGSTEN, ALUMINUM OXIDES, AND ZIRCONIUM DIOXIDE IN VACUUM., Fiz. Met. Met. 28 653-60 (Oct 1969). (1969).
[69] J.A. Thornton, High Rate Thick Film Growth., Annu. Rev. Mater. Sci. 7 (1977) 239–260. doi:10.1146/annurev.ms.07.080177.001323.
[70] R.A. Haefer, Oberflächen- und Dünnschicht-Technologie, Springer Berlin Heidelberg, Berlin, Heidelberg, 1987. doi:10.1007/978-3-642-82835-5.
[71] H. Lüth, Solid Surfaces, Interfaces and Thin Films, Springer Berlin Heidelberg, Berlin, Heidelberg, 2010. doi:10.1007/978-3-642-13592-7.
[72] E. BAUER, Phänomenologische Theorie der Kristallabscheidung an Oberflächen. II, Zeitschrift Für Krist. - Cryst. Mater. 110 (1958) 395–431. doi:10.1524/zkri.1958.110.16.395.
[73] E. BAUER, Phänomenologische Theorie der Kristallabscheidung an Oberflächen. I, Zeitschrift Für Krist. - Cryst. Mater. 110 (1958) 395–431. doi:10.1524/zkri.1958.110.16.372.
[74] M. Volmer, A. Weber, Keimbildung in übersättigten Gebilden, Zeitschrift Für Phys. Chemie. 119U (1926) 277–301. doi:10.1515/zpch-1926-11927.
[75] F.C. Frank, J.H. Van Der Merwe, One-dimensional dislocations. I. Static theory, Proc. R. Soc. London. Ser. A. Math. Phys. Sci. 198 (1949) 205–216. doi:10.1098/rspa.1949.0095.
[76] F.C. Frank, J.H. Van Der Merwe, One-dimensional dislocations. II. Misfitting monolayers and oriented overgrowth, Proc. R. Soc. London. Ser. A. Math. Phys. Sci. 198 (1949) 216–225. doi:10.1098/rspa.1949.0096.
[77] F.C. Frank, J.H. Van Der Merwe, One-dimensional dislocations - III. Influence of the second harmonic term in the potential representation, on the properties of the model, Proc. R. Soc. London. Ser. A. Math. Phys. Sci. 200 (1949) 125–134. doi:10.1098/rspa.1949.0163.
[78] I.N. Stranski, L. Krastanow, Zur Theorie der orientierten Ausscheidung von Ionenkristallen aufeinander, Monatshefte Für Chemie. 71 (1937) 351–364.

doi:10.1007/BF01798103.
[79] J.E. Greene, Nucleation, Film Growth, and Microstructural, in: R.F. Bunshah (Ed.), Handb. Depos. Technol. Film. Coatings, Second Ed., Noyes, New Jersey, 1994: pp. 707–765.
[80] I. Petrov, P.B. Barna, L. Hultman, J.E. Greene, Microstructural evolution during film growth, J. Vac. Sci. Technol. A Vacuum, Surfaces, Film. 21 (2003) S117–S128. doi:10.1116/1.1601610.
[81] J.A. Thornton, Influence of apparatus geometry and deposition conditions on the structure and topography of thick sputtered coatings, J. Vac. Sci. Technol. 11 (1974) 666–670. doi:10.1116/1.1312732.
[82] P.B. BARNA, M. ADAMIK, GROWTH MECHANISMS OF POLYCRYSTALLINE THIN FILMS, in: Sci. Technol. Thin Film., WORLD SCIENTIFIC, 1995: pp. 1–28. doi:10.1142/9789814261425_0001.
[83] P.. Barna, M. Adamik, Fundamental structure forming phenomena of polycrystalline films and the structure zone models, Thin Solid Films. 317 (1998) 27–33. doi:10.1016/S0040-6090(97)00503-8.
[84] M.J. Cordill, Flexible Film Systems: Current Understanding and Future Prospects, Jom. 62 (2010) 9–14.
[85] S. Djaziri, P.-O.O. Renault, F. Hild, E. Le Bourhis, P. Goudeau, D. Thiaudire, D. Faurie, D. Thiaudière, D. Faurie, Combined synchrotron X-ray and image-correlation analyses of biaxially deformed W/Cu nano-composite thin films on Kapton, J. Appl. Crystallogr. 44 (2011) 1071–1079. doi:10.1107/S0021889811030226.
[86] O. Glushko, M.J. Cordill, A. Klug, E.J.W. List-Kratochvil, The effect of bending loading conditions on the reliability of inkjet printed and evaporated silver metallization on polymer substrates, Microelectron. Reliab. 56 (2016) 109–113. doi:10.1016/j.microrel.2015.10.007.
[87] N. Lu, X. Wang, Z. Suo, J. Vlassak, Metal films on polymer substrates stretched beyond 50%, Appl. Phys. Lett. 91 (2007) 2–4. doi:10.1063/1.2817234.
[88] O. Glushko, M.J. Cordill, Electrical Resistance of Metal Films on Polymer Substrates Under Tension, Exp. Tech. 40 (2016) 303–310. doi:10.1007/s40799-016-0040-x.
[89] Y. Xiang, T. Li, Z. Suo, J.J. Vlassak, High ductility of a metal film adherent on a polymer substrate, Appl. Phys. Lett. 87 (2005) 161910. doi:10.1063/1.2108110.
[90] T. Li, Z.Y. Huang, Z.C. Xi, S.P. Lacour, S. Wagner, Z. Suo, Delocalizing strain in a thin metal film on a polymer substrate, Mech. Mater. 37 (2005) 261–273. doi:10.1016/j.mechmat.2004.02.002.
[91] V.M. Marx, F. Toth, A. Wiesinger, J. Berger, C. Kirchlechner, M.J. Cordill, F.D. Fischer, F.G. Rammerstorfer, G. Dehm, The influence of a brittle Cr interlayer on the deformation behavior of thin Cu films on flexible substrates: Experiment and model, Acta Mater. 89 (2015) 278–289. doi:10.1016/j.actamat.2015.01.047.
[92] B. Putz, C. May-Miller, V. Matl, B. Völker, D.M. Többens, C. Semprimoschnig, M.J. Cordill, Two-stage cracking of metallic bi-layers on polymer substrates under tension, Scr. Mater. 145 (2018) 5–8. doi:10.1016/j.scriptamat.2017.09.039.
[93] B. Putz, R.L. Schoeppner, O. Glushko, D.F. Bahr, M.J. Cordill, Improved electro-mechanical performance of gold films on polyimide without adhesion layers,

Scr. Mater. 102 (2015) 23–26. doi:10.1016/j.scriptamat.2015.02.005.
[94] M.N. Polyakov, J. Lohmiller, P.A. Gruber, A.M. Hodge, Load sharing phenomena in nanoscale Cu/Nb multilayers, Adv. Eng. Mater. 17 (2015) 810–814. doi:10.1002/adem.201400368.
[95] P.A. Gruber, E. Arzt, R. Spolenak, Brittle-to-ductile transition in ultrathin Ta/Cu film systems, J. Mater. Res. 24 (2009) 1906–1918. doi:10.1557/jmr.2009.0252.
[96] K. Wu, J.Y. Zhang, P. Zhang, Y.Q. Wang, G. Liu, G.J. Zhang, J. Sun, Fracture behavior and adhesion energy of nanostructured Cu/Mo multilayer films, Mater. Sci. Eng. A. 613 (2014) 130–135. doi:10.1016/j.msea.2014.06.083.
[97] M.A. Nicolet, DIFFUSION BARRIERS IN THIS SILMS, Thin Solid Films. 52 (1978) 415–443.
[98] M. Nicolet, M. Bartur, Diffusion barriers in layered contact structures, J. Vac. Sci. Technol. 19 (1981) 786–793. doi:10.1116/1.571149.
[99] P.A. Gruber, J. Boehm, F. Onuseit, A. Wanner, R. Spolenak, E. Arzt, Size effects on yield strength and strain hardening for ultra-thin Cu films with and without passivation: A study by synchrotron and bulge test techniques, Acta Mater. 56 (2008) 2318–2335. doi:https://doi.org/10.1016/j.actamat.2008.01.027.
[100] R.M. Niu, G. Liu, C. Wang, G. Zhang, X.D. Ding, J. Sun, Thickness dependent critical strain in submicron Cu films adherent to polymer substrate, Appl. Phys. Lett. 90 (2007) 161907. doi:10.1063/1.2722684.
[101] N. Lu, X. Wang, Z. Suo, J. Vlassak, Failure by simultaneous grain growth, strain localization, and interface debonding in metal films on polymer substrates, J. Mater. Res. 24 (2009) 379–385. doi:10.1557/jmr.2009.0048.
[102] N. Lu, Z. Suo, J.J. Vlassak, The effect of film thickness on the failure strain of polymer-supported metal films, Acta Mater. 58 (2010) 1679–1687. doi:10.1016/j.actamat.2009.11.010.
[103] T. Jörg, M.J. Cordill, R. Franz, C. Kirchlechner, D.M. Többens, J. Winkler, C. Mitterer, Thickness dependence of the electro-mechanical response of sputter-deposited Mo thin films on polyimide: Insights from in situ synchrotron diffraction tensile tests, Mater. Sci. Eng. A. 697 (2017) 17–23. doi:10.1016/j.msea.2017.04.101.
[104] Y. Leterrier, Durability of nanosized oxygen-barrier coatings on polymers, Prog. Mater. Sci. 48 (2003) 1–55. doi:10.1016/S0079-6425(02)00002-6.
[105] W. Weibull, Wide Applicability, J. Appl. Mech. (1951).
[106] J. Andersons, R. Joffe, R. Sandmark, Constrained fragmentation of composites under uniaxial loading, Mech. Compos. Mater. 31 (1995) 26–33. doi:10.1007/BF00616733.
[107] E.I. Preiß, B. Merle, M. Göken, Understanding the extremely low fracture toughness of freestanding gold thin films by in-situ bulge testing in an AFM, Mater. Sci. Eng. A. 691 (2017) 218–225. doi:10.1016/j.msea.2017.03.037.
[108] S.H. Oh, M. Legros, D. Kiener, G. Dehm, In situ observation of dislocation nucleation and escape in a submicrometre aluminium single crystal, Nat. Mater. 8 (2009) 95–100. doi:10.1038/nmat2370.
[109] M. Legros, D.S. Gianola, K.J. Hemker, In situ TEM observations of fast grain-boundary motion in stressed nanocrystalline aluminum films, Acta Mater. 56 (2008) 3380–3393. doi:10.1016/j.actamat.2008.03.032.
[110] G. Gottstein, Physikalische Grundlagen der Materialkunde, 3rd Editio, Springer

Berlin Heidelberg New York, 2007.
[111] T. Li, Z. Suo, Ductility of thin metal films on polymer substrates modulated by interfacial adhesion, Int. J. Solids Struct. 44 (2007) 1696–1705. doi:10.1016/j.ijsolstr.2006.07.022.
[112] A. Kleinbichler, M. Bartosik, B. Völker, M.J. Cordill, Thin Film Adhesion of Flexible Electronics Influenced by Interlayers, Adv. Eng. Mater. 19 (2017) 1600665. doi:10.1002/adem.201600665.
[113] D.C. Agrawal, R. Raj, Measurement of the ultimate shear strength of a metal-ceramic interface, Acta Metall. 37 (1989) 1265–1270. doi:10.1016/0001-6160(89)90120-X.
[114] P.A. Gruber, C. Solenthaler, E. Arzt, R. Spolenak, Strong single-crystalline Au films tested by a new synchrotron technique, Acta Mater. 56 (2008) 1876–1889. doi:10.1016/j.actamat.2007.12.043.
[115] T. Lacroix, B. Tilmans, R. Keunings, M. Desaeger, I. Verpoest, Modelling of critical fibre length and interfacial debonding in the fragmentation testing of polymer composites, Compos. Sci. Technol. 43 (1992) 379–387. doi:10.1016/0266-3538(92)90061-7.
[116] T. Lacroix, R. Keunings, M. Desaeger, I. Verpoest, A new data reduction scheme for the fragmentation testing of polymer composites, J. Mater. Sci. 30 (1995) 683–692. doi:10.1007/BF00356328.
[117] A.A. Taylor, M.J. Cordill, G. Dehm, On the limits of the interfacial yield model for fragmentation testing of brittle films on polymer substrates, Philos. Mag. 92 (2012) 3363–3380. doi:10.1080/14786435.2012.723145.
[118] A.A. Taylor, V. Edlmayr, M.J. Cordill, G. Dehm, The effect of film thickness variations in periodic cracking: Analysis and experiments, Surf. Coatings Technol. 206 (2011) 1830–1836. doi:10.1016/j.surfcoat.2011.07.047.
[119] M. YANAKA, Y. TSUKAHARA, N. NAKASO, M. YANAKA, Cracking phenomena of brittle films in nanostructure composites analysed by a modified shear lag model with residual strain, J. Mater. Sci. 33 (1998) 2111–2119. doi:10.1023/A:1004371203514.
[120] M.J. Cordill, F.D. Fischer, F.G. Rammerstorfer, G. Dehm, Adhesion energies of Cr thin films on polyimide determined from buckling: Experiment and model, Acta Mater. 58 (2010) 5520–5531. doi:10.1016/j.actamat.2010.06.032.
[121] Y. Leterrier, L. Boogh, J. Andersons, J.-A.E. Manson, Adhesion of silicon oxide layers on poly(ethylene terephthalate). I: Effect of substrate properties on coating's fragmentation process, J. Polym. Sci. Part B Polym. Phys. 35 (1997) 1449–1461. doi:10.1002/(SICI)1099-0488(19970715)35:9<1449::AID-POLB15>3.0.CO;2-6.
[122] M.J. Cordill, V.M. Marx, Fragmentation testing for ductile thin films on polymer substrates, Philos. Mag. Lett. 93 (2013) 618–624. doi:10.1080/09500839.2013.830792.
[123] M.J. Cordill, A. Taylor, J. Schalko, G. Dehm, Fracture and delamination of chromium thin films on polymer substrates, Metall. Mater. Trans. A Phys. Metall. Mater. Sci. 41 (2010) 870–875. doi:10.1007/s11661-009-9988-9.
[124] B. Putz, O. Glushko, V.M. Marx, C. Kirchlechner, D. Toebbens, M.J. Cordill, Electro-mechanical performance of thin gold films on polyimide, MRS Adv. 1 (2016) 773–778. doi:10.1557/adv.2016.233.

[125] Y. Leterrier, A. Mottet, N. Bouquet, D. Gilliéron, P. Dumont, A. Pinyol, L. Lalande, J.H. Waller, J.-A.E. Månson, Mechanical integrity of thin inorganic coatings on polymer substrates under quasi-static, thermal and fatigue loadings, Thin Solid Films. 519 (2010) 1729–1737. doi:10.1016/j.tsf.2010.06.003.
[126] S. Djaziri, D. Faurie, P.O. Renault, E. Le Bourhis, P. Goudeau, G. Geandier, D. Thiaudière, Yield surface of polycrystalline thin films as revealed by non-equibiaxial loadings at small deformation, Acta Mater. 61 (2013) 5067–5077. doi:10.1016/j.actamat.2013.04.031.
[127] G. Geandier, D. Faurie, P.O. Renault, D. Thiaudière, E. Le Bourhis, In situ monitoring of X-ray strain pole figures of a biaxially deformed ultra-thin film on a flexible substrate, J. Appl. Crystallogr. 47 (2014) 181–187. doi:10.1107/S1600576713030720.
[128] D. Faurie, F. Zighem, P. Godard, G. Parry, T. Sadat, D. Thiaudière, P.O. Renault, In situ x-ray diffraction analysis of 2D crack patterning in thin films, Acta Mater. 165 (2019) 177–182. doi:10.1016/j.actamat.2018.11.040.
[129] M.J. Cordill, A.A. Taylor, K. Schmidegg, Thickness Effects on the Fracture of Chromium Films on Polyethylene Terephthalate, 156 (2011) 434–437.
[130] M.J. Cordill, O. Glushko, J. Kreith, V.M. Marx, C. Kirchlechner, Measuring electro-mechanical properties of thin films on polymer substrates, Microelectron. Eng. 137 (2015) 96–100. doi:10.1016/j.mee.2014.08.002.
[131] H.-Y. Lee, S.-M. Yi, J.-H. Lee, H.-S. Lee, S. Hyun, Y.-C. Joo, Effects of bending fatigue on the electrical resistance in metallic films on flexible substrates, Met. Mater. Int. 16 (2010) 947–951. doi:10.1007/s12540-010-1213-2.
[132] M.M. Hamasha, K. Alzoubi, J.C. Switzer, S. Lu, M.D. Poliks, C.R. Westgate, Reliability of sputtered aluminum thin film on flexible substrate under high cyclic bending fatigue conditions, IEEE Trans. Components, Packag. Manuf. Technol. 2 (2012) 2007–2016. doi:10.1109/TCPMT.2012.2214034.
[133] C. Trinks, C.A. Volkert, Transition from dislocation glide to creep controlled damage in fatigued thin Cu films, J. Appl. Phys. 114 (2013). doi:10.1063/1.4819760.
[134] O. Glushko, P. Kraker, M.J. Cordill, Explicit relationship between electrical and topological degradation of polymer-supported metal films subjected to mechanical loading, Appl. Phys. Lett. 110 (2017) 1–5. doi:10.1063/1.4982802.
[135] O. Glushko, V.M. Marx, C. Kirchlechner, I. Zizak, M.J. Cordill, Recovery of electrical resistance in copper films on polyethylene terephthalate subjected to a tensile strain, Thin Solid Films. 552 (2014) 141–145. doi:10.1016/j.tsf.2013.12.055.
[136] P.J. Withers, H.K.D.H. Bhadeshia, Residual stress. Part 1 – Measurement techniques, Mater. Sci. Technol. 17 (2001) 355–365. doi:10.1179/026708301101509980.
[137] G.S. Schajer, Practical Residual Stress Measurement Methods, John Wiley & Sons, Ltd, Chichester, UK, 2013. doi:10.1002/9781118402832.
[138] I.C. Noyan, J.B. Cohen, Residual Stress: Measurement by Diffraction and Interpretation, Springer-Verlag New York, New York, 1987.
[139] Q. Luo, A.H. Jones, High-precision determination of residual stress of polycrystalline coatings using optimised XRD-sin2ψ technique, Surf. Coatings Technol. 205 (2010) 1403–1408. doi:10.1016/j.surfcoat.2010.07.108.

[140] W. Voigt, Lehrbuch der Kristallphysik, Vieweg+Teubner Verlag, Wiesbaden, 1966. doi:10.1007/978-3-663-15884-4.
[141] A. Reuss, Berechnung der Fließgrenze von Mischkristallen auf Grund der Plastizitätsbedingung für Einkristalle ., ZAMM - Zeitschrift Für Angew. Math. Und Mech. 9 (1929) 49–58. doi:10.1002/zamm.19290090104.
[142] J.D. Eshelby, The determination of the elastic field of an ellipsoidal inclusion, and related problems, Proc. R. Soc. London. Ser. A. Math. Phys. Sci. 241 (1957) 376–396. doi:10.1098/rspa.1957.0133.
[143] E. Kröner, Berechnung der elastischen Konstanten des Vielkristalls aus den Konstanten des Einkristalls, Zeitschrift Für Phys. 151 (1958) 504–518. doi:10.1007/BF01337948.
[144] R. Hill, The Elastic Behaviour of a Crystalline Aggregate, Proc. Phys. Soc. Sect. A. 65 (1952) 349–354. doi:10.1088/0370-1298/65/5/307.
[145] ASTM E1426 - 14, Standard Test Method for Determining the X-Ray Elastic Constants for Use in the Measurement of Residual Stress Using X-Ray Diffraction Techniques, (2014). doi:https://dx.doi.org/10.1520/E1426-14R19E01.
[146] O. Glushko, A. Klug, E.J.W. List-Kratochvil, M.J. Cordill, Monotonic and cyclic mechanical reliability of metallization lines on polymer substrates, J. Mater. Res. 32 (2017) 1760–1769. doi:10.1557/jmr.2017.121.
[147] Q. Ma, A four-point bending technique for studying subcritical crack growth in thin films and at interfaces, J. Mater. Res. 12 (1997) 840–845. doi:10.1557/JMR.1997.0122.
[148] A.A. Abdallah, P.C.P. Bouten, G. de With, Experimental study on buckle evolution of thin inorganic layers on a polymer substrate, Eng. Fract. Mech. 77 (2010) 2896–2905. doi:10.1016/j.engfracmech.2010.07.012.
[149] M. Yang, M.W. Chon, J.H. Kim, S.H. Lee, J. Jo, J. Yeo, S.H. Ko, S.H. Choa, Mechanical and environmental durability of roll-to-roll printed silver nanoparticle film using a rapid laser annealing process for flexible electronics, Microelectron. Reliab. 54 (2014) 2871–2880. doi:10.1016/j.microrel.2014.07.004.
[150] B. Bensaid, X. Boddaert, P. Benaben, R. Gwoziecki, R. Coppard, Reliability of OTFTs on flexible substrate: mechanical stress effect, Eur. Phys. J. Appl. Phys. 55 (2011) 23907. doi:10.1051/epjap/2011100426.
[151] S. Il Park, J.H. Ahn, X. Feng, S. Wang, Y. Huang, J.A. Rogers, Theoretical and experimental studies of bending of inorganic electronic materials on plastic substrates, Adv. Funct. Mater. 18 (2008) 2673–2684. doi:10.1002/adfm.200800306.
[152] K. Alzoubi, S. Lu, B. Sammakia, M. Poliks, Experimental and Analytical Studies on the High Cycle Fatigue of Thin Film Metal on PET Substrate for Flexible Electronics Applications, IEEE Trans. Components, Packag. Manuf. Technol. 1 (2011) 43–51. doi:10.1109/TCPMT.2010.2100911.
[153] D.A. Van Den Ende, H.J. Van De Wiel, R.H.L. Kusters, A. Sridhar, J.F.M. Schram, M. Cauwe, J. Van Den Brand, Mechanical and electrical properties of ultra-thin chips and flexible electronics assemblies during bending, Microelectron. Reliab. 54 (2014) 2860–2870. doi:10.1016/j.microrel.2014.07.125.
[154] J. Jang, S. Lee, 24.1: Invited Paper: Flexible Oxide TFTs for Bendable and flexible displays, SID Symp. Dig. Tech. Pap. 49 (2018) 248–251. doi:10.1002/sdtp.12693.

[155] S. Hong, M. Mativenga, J. Jang, Extreme bending test of IGZO TFT, in: 2014 21st Int. Work. Act. Flatpanel Displays Devices, IEEE, 2014: pp. 125–127. doi:10.1109/AM-FPD.2014.6867145.
[156] G.D. Sim, Y. Hwangbo, H.H. Kim, S.B. Lee, J.J. Vlassak, Fatigue of polymer-supported Ag thin films, Scr. Mater. 66 (2012) 915–918. doi:10.1016/j.scriptamat.2012.02.030.
[157] J. Lewis, Material challenge for flexible organic devices, Mater. Today. 9 (2006) 38–45. doi:10.1016/S1369-7021(06)71446-8.
[158] L. Romano Brandt, E. Salvati, C. Papadaki, H. Zhang, S. Ying, E. Le Bourhis, I. Dolbnya, T. Sui, A.M. Korsunsky, Probing the deformation and fracture properties of Cu/W nano-multilayers by in situ SEM and synchrotron XRD strain microscopy, Surf. Coatings Technol. 320 (2017) 158–167. doi:10.1016/j.surfcoat.2017.01.065.
[159] X.F. Zhu, B. Zhang, J. Gao, G.P. Zhang, Evaluation of the crack-initiation strain of a Cu-Ni multilayer on a flexible substrate, Scr. Mater. 60 (2009) 178–181. doi:10.1016/j.scriptamat.2008.10.004.
[160] T. Miyamura, J. Koike, The effects of Cr oxidation and polyimide degradation on interface adhesion strength in Cu/Cr/polyimide flexible films, Mater. Sci. Eng. A. 445–446 (2007) 620–624. doi:10.1016/j.msea.2006.09.097.
[161] M.J. Cordill, A.A. Taylor, J. Berger, K. Schmidegg, G. Dehm, Robust mechanical performance of chromium-coated polyethylene terephthalate over a broad range of conditions, in: Philos. Mag., 2012: pp. 3346–3362. doi:10.1080/14786435.2012.700418.
[162] Scilab Enterprises, Scilab: Free and Open Source software for numerical computation, (2012). http://www.scilab.org.
[163] A. Wyss, M. Schamel, A.S. Sologubenko, R. Denk, M. Hohage, P. Zeppenfeld, R. Spolenak, Reflectance anisotropy spectroscopy as a tool for mechanical characterization of metallic thin films, J. Phys. D. Appl. Phys. 48 (2015) 415303. doi:10.1088/0022-3727/48/41/415303.
[164] S. Kim, S. Won, G.-D. Sim, I. Park, S.-B. Lee, Tensile characteristics of metal nanoparticle films on flexible polymer substrates for printed electronics applications, Nanotechnology. 24 (2013) 085701. doi:10.1088/0957-4484/24/8/085701.
[165] G.K. Rane, S. Menzel, T. Gemming, J. Eckert, Microstructure, electrical resistivity and stresses in sputter deposited W and Mo films and the influence of the interface on bilayer properties, Thin Solid Films. 571 (2014) 1–8. doi:10.1016/j.tsf.2014.09.034.
[166] M.L. Green, R.A. Levy, R.G. Nuzzo, E. Coleman, Aluminum films prepared by metal-organic low pressure chemical vapor deposition, Thin Solid Films. 114 (1984) 367–377. doi:10.1016/0040-6090(84)90136-6.
[167] M.J. Cordill, V.M. Marx, C. Kirchlechner, Ductile film delamination from compliant substrates using hard overlayers, Thin Solid Films. 571 (2014) 302–307. doi:10.1016/j.tsf.2014.02.093.
[168] M.D. Abràmoff, P.J. Magalhães, S.J. Ram, Image processing with imageJ, Biophotonics Int. 11 (2004) 36–41. doi:10.1117/1.3589100.
[169] K. Alzoubi, S. Lu, B. Sammakia, M. Poliks, Factor Effect Study for the High Cyclic Bending Fatigue of Thin Films on PET Substrate for Flexible Displays

Applications, IEEE/OSA J. Disp. Technol. 7 (2011) 348–355. doi:10.1109/JDT.2010.2076772.
[170] O. Kraft, R. Schwaiger, P. Wellner, Fatigue in thin films: Lifetime and damage formation, Mater. Sci. Eng. A. 319–321 (2001) 919–923. doi:10.1016/S0921-5093(01)00990-X.
[171] D.R. Cairns, G.P. Crawford, Electromechanical Properties of Transparent Conducting Substrates for Flexible Electronic Displays, 93 (2005) 1451–1458.
[172] V.M. Marx, C. Kirchlechner, B. Breitbach, M.J. Cordill, D.M. T??bbens, T. Waitz, G. Dehm, Strain-induced phase transformation of a thin Co film on flexible substrates, Acta Mater. 121 (2016) 227–233. doi:10.1016/j.actamat.2016.09.015.
[173] G.P. Zhang, R. Schwaiger, C.A. Volkert, O. Kraft, Effect of film thickness and grain size on fatigue-induced dislocation structures in Cu thin films, Philos. Mag. Lett. 83 (2003) 477–483. doi:10.1080/0950083031000151383.
[174] U. Essmann, U. Gösele, H. Mughrabi, A model of extrusions and intrusions in fatigued metals I. Point-defect production and the growth of extrusions, Philos. Mag. A Phys. Condens. Matter, Struct. Defects Mech. Prop. 44 (1981) 405–426. doi:10.1080/01418618108239541.
[175] M.J. Cordill, O. Glushko, A. Kleinbichler, B. Putz, D.M. Többens, C. Kirchlechner, Microstructural influence on the cyclic electro-mechanical behaviour of ductile films on polymer substrates, Thin Solid Films. 644 (2017) 166–172. doi:10.1016/j.tsf.2017.06.067.
[176] W. Heinz, R. Pippan, G. Dehm, Investigation of the fatigue behavior of Al thin films with different microstructure, Mater. Sci. Eng. A. 527 (2010) 7757–7763. doi:10.1016/j.msea.2010.08.046.
[177] O. Glushko, M.J. Cordill, Electrical resistance decrease due to grain coarsening under cyclic deformation, Jom. 66 (2014) 598–601. doi:10.1007/s11837-014-0943-x.
[178] S.R. Forrest, The path to ubiquitous and low-cost organic electronic appliances on plastic, Nature. 428 (2004) 911–918. doi:10.1038/nature02498.
[179] K. Alzoubi, M.M. Hamasha, S. Lu, B. Sammakia, Bending fatigue study of sputtered ITO on flexible substrate, IEEE/OSA J. Disp. Technol. 7 (2011) 593–600. doi:10.1109/JDT.2011.2151830.
[180] D. Nečas, P. Klapetek, Gwyddion: An open-source software for SPM data analysis, 2012. doi:10.2478/s11534-011-0096-2.
[181] T. Spalvins, W.A. Brainard, Nodular growth in thick-sputtered metallic coatings, J. Vac. Sci. Technol. 11 (1974) 1186–1192. doi:10.1116/1.1318706.
[182] O. Glushko, A. Klug, E.J.W. List-Kratochvil, M.J. Cordill, Relationship between mechanical damage and electrical degradation in polymer-supported metal films subjected to cyclic loading, Mater. Sci. Eng. A. 662 (2016) 157–161. doi:10.1016/j.msea.2016.03.052.
[183] M.C. Martin, K.F. Welton, The change in electrical resistivity with plastic deformation of aluminum and nickel, Acta Metall. 15 (1967) 571–573. doi:10.1016/0001-6160(67)90094-6.
[184] K. Alzoubi, S. Lu, B. Sammakia, M. Poliks, Experimental Study of the High Cycle Fatigue of Thin Film Metal on Polyethylene Terephthalate for Flexible Electronics Applications, in: ASME 2009 InterPACK Conf. Vol. 1, ASME, 2009: pp.

27–32. doi:10.1115/InterPACK2009-89247.
[185] W.E. Howard, Limitations and prospects of a-Si:H TFTs, J. Soc. Inf. Disp. 3 (1995) 127. doi:10.1889/1.1984952.
[186] T. Jörg, D. Music, M.J. Cordill, R. Franz, H. Köstenbauer, C. Linke, J. Winkler, J.M. Schneider, C. Mitterer, A correlative experimental and ab initio approach to improve the fracture behavior of Mo thin films by alloying with Cu, Appl. Phys. Lett. 111 (2017) 0–4. doi:10.1063/1.4999205.
[187] P.L. Rossiter, The electrical resistivity of metals and alloys, Cambridge University Press, Cambridge, 1987. doi:10.1017/CBO9780511600289.
[188] M. Spittel, T. Spittel, Mechanical and physical properties of alloys and metals, in: Part 3 Non-Ferrous Alloy. - Heavy Met., Springer Berlin Heidelberg, Berlin, Heidelberg, 2016: pp. 87–113. doi:10.1007/978-3-642-14174-4_4.
[189] M. Mühlbacher, G. Greczynski, B. Sartory, N. Schalk, J. Lu, I. Petrov, J.E. Greene, L. Hultman, C. Mitterer, Enhanced Ti0.84Ta0.16N diffusion barriers, grown by a hybrid sputtering technique with no substrate heating, between Si(001) wafers and Cu overlayers, Sci. Rep. 8 (2018) 1–9. doi:10.1038/s41598-018-23782-9.
[190] T. Car, J. Ivkov, M. Jerčinović, N. Radić, The relaxation processes in the Al-(Nb, Mo, Ta, W) binary amorphous thin films, Vacuum. 98 (2013) 75–80. doi:10.1016/j.vacuum.2012.09.008.
[191] M.J. Cordill, A. Kleinbichler, B. Völker, P. Kraker, D.R. Economy, D. Többens, C. Kirchlechner, M.S. Kennedy, In-situ observations of the fracture and adhesion of Cu/Nb multilayers on polyimide substrates, Mater. Sci. Eng. A. 735 (2018) 456–462. doi:10.1016/j.msea.2018.08.043.
[192] V.M. Marx, C. Kirchlechner, I. Zizak, M.J. Cordill, G. Dehm, Adhesion measurement of a buried Cr interlayer on polyimide, Philos. Mag. 95 (2015) 1982–1991. doi:10.1080/14786435.2014.920543.
[193] M.J. Cordill, A.A. Taylor, Thickness effect on the fracture and delamination of titanium films, Thin Solid Films. 589 (2015) 209–214. doi:10.1016/j.tsf.2015.05.021.
[194] K. Wu, J.Y. Zhang, J. Li, Y.Q. Wang, G. Liu, J. Sun, Length-scale-dependent cracking and buckling behaviors of nanostructured Cu/Cr multilayer films on compliant substrates, Acta Mater. 100 (2015) 344–358. doi:10.1016/j.actamat.2015.08.055.
[195] J. Bass, 1.2.1 Pure metal resistivities at T = 273.2 K, in: Electr. Resist. Kondo Spin Fluct. Syst. Spin Glas. Thermopower, Springer-Verlag, Berlin/Heidelberg, n.d.: pp. 5–13. doi:10.1007/10307022_3.
[196] R. Lorenz, M. O'Sullivan, D. Sprenger, B. Lang, C. Mitterer, Chemical composition and properties of MoAl thin films deposited by sputtering from MoAl compound targets, J. Vac. Sci. Technol. A Vacuum, Surfaces, Film. 35 (2017) 041504. doi:10.1116/1.4983689.
[197] A.M. Hofer, J. Schlacher, J. Keckes, J. Winkler, C. Mitterer, Sputtered molybdenum films: Structure and property evolution with film thickness, Vacuum. 99 (2014) 149–152. doi:10.1016/j.vacuum.2013.05.018.
[198] B. Predel, Mo-Nb (Molybdenum-Niobium), in: O. Madelung (Ed.), Li-Mg – Nd-Zr, Springer-Verlag, Berlin/Heidelberg, 1997: pp. 1–2. doi:10.1007/10522884_2070.
[199] A.M. Hofer, G. Mori, A. Fian, J. Winkler, C. Mitterer, Improvement of oxidation and corrosion resistance of Mo thin films by alloying with Ta, Thin Solid Films.

599 (2016) 1–6. doi:10.1016/j.tsf.2015.12.052.
[200] ASTM International, ASTM F390-98:Sheet Resistance of Thin Metallic Films With a Collinear Four-Probe Array, ASTM Int. 98 (2003) 1–4. doi:10.1520/F0390-98R03.
[201] A. Jiang, A. Yohannan, N.O. Nnolim, T.A. Tyson, L. Axe, S.L. Lee, P. Cote, Investigation of the structure of β-tantalum, Thin Solid Films. 437 (2003) 116–122. doi:10.1016/S0040-6090(03)00702-8.
[202] T. Li, Z. Huang, Z. Suo, S.P. Lacour, S. Wagner, Stretchability of thin metal films on elastomer substrates, Appl. Phys. Lett. 85 (2004) 3435–3437. doi:10.1063/1.1806275.
[203] P. Kreiml, M. Rausch, V.L. Terziyska, H. Köstenbauer, J. Winkler, C. Mitterer, M.J. Cordill, Improved electro-mechanical reliability of flexible systems with alloyed adhesion layers, Thin Solid Film. (2020).
[204] G.C.A.M. Janssen, M.M. Abdalla, F. van Keulen, B.R. Pujada, B. van Venrooy, Celebrating the 100th anniversary of the Stoney equation for film stress: Developments from polycrystalline steel strips to single crystal silicon wafers, Thin Solid Films. 517 (2009) 1858–1867. doi:10.1016/j.tsf.2008.07.014.
[205] G.G. Stoney, C.A. Parsons, The Tension of Metallic Films Deposited by Electrolysis, Proc. R. Soc. A Math. Phys. Eng. Sci. 82 (1909) 172–175. doi:10.1098/rspa.1909.0021.
[206] G.D. Sim, S. Won, C.Y. Jin, I. Park, S.B. Lee, J.J. Vlassak, Improving the stretchability of as-deposited Ag coatings on poly-ethylene-terephthalate substrates through use of an acrylic primer, in: J. Appl. Phys., 2011: p. 073511. doi:10.1063/1.3567917.
[207] G.D. Sim, Y.S. Lee, S.B. Lee, J.J. Vlassak, Effects of stretching and cycling on the fatigue behavior of polymer-supported Ag thin films, Mater. Sci. Eng. A. 575 (2013) 86–93. doi:10.1016/j.msea.2013.03.043.

LIST OF PUBLICATIONS

C. Ganser, P. Kreiml, R. Morak, F. Weber, O. Paris, R. Schennach, C. Teichert, The effects of water uptake on mechanical properties of viscose fibers, Cellulose. 22 (2015) 2777–2786. doi:10.1007/s10570-015-0666-3.

N. Schrödl, E. Bucher, A. Egger, P. Kreiml, C. Teichert, T. Höschen, W. Sitte, Long-term stability of the IT-SOFC cathode materials $La_{0.6}Sr_{0.4}CoO_{3-\delta}$ and $La_2NiO_{4+\delta}$ against combined chromium and silicon poisoning, Solid State Ionics. 276 (2015). doi:10.1016/j.ssi.2015.03.035.

M. Rausch, M. Pavlovič, P. Kreiml, M.J. Cordill, J. Winkler, C. Mitterer, Sputter deposition of Mo-based multicomponent thin films from rotatable targets: Experiment and simulation, Appl. Surf. Sci. 455 (2018) 1029–1036. doi:10.1016/j.apsusc.2018.06.012.

P. Kreiml, M. Rausch, V.L. Terziyska, J. Winkler, C. Mitterer, M.J. Cordill, Compressive and tensile bending of sputter deposited Al/Mo bilayers, Scr. Mater. 162 (2019) 367–371. doi:10.1016/j.scriptamat.2018.11.048.

P. Kreiml, M. Rausch, V.L. Terziyska, H. Köstenbauer, J. Winkler, C. Mitterer, M.J. Cordill, Electro-mechanical behavior of Al/Mo bilayers studied with in situ straining methods, Thin Solid Films. 665 (2018) 131–136. doi:10.1016/J.TSF.2018.07.054.

P. Kreiml, M. Rausch, V.L. Terziyska, H. Köstenbauer, J. Winkler, C. Mitterer, M.J. Cordill, Correlation of mechanical damage and electrical behavior of Al/Mo bilayers subjected to bending, Thin Solid Films. 687 (2019) 137480. doi:10.1016/j.tsf.2019.137480.

M. Rausch, A. Sabag, K.-H. Pichler, G.C. Gruber, J. Köstenbauer, H. Köstenbauer, P. Kreiml, M.J. Cordill, J. Winkler, C. Mitterer, The sputter performance of an industrial-scale planar Mo-target over its lifetime: Target erosion and film properties, Surf. Coatings Technol. 381 (2020) 125174. doi:10.1016/j.surfcoat.2019.125174.

E.J. Frankberg, J. Kalikka, F. Garcia Ferré, L. Joly-Pottuz, T. Salminen, J. Hintikka, M. Hokka, S. Koneti, T. Douillard, B. Le Saint, P. Kreiml, M.J. Cordill, T. Epicier, D. Stauffer, M. Vanazzi, L. Roiban, J. Akola, F. Di Fonzo, E. Levänen, K. Masenelli-Varlot, Highly ductile amorphous oxide at room temperature and high strain rate, Science (80-.). 366 (2019) 864–869. doi:10.1126/science.aav1254.

M. Rausch, M. Golizadeh, P. Kreiml, M.J. Cordill, J. Winkler, C. Mitterer, Sputter deposition of NiW films from a rotatable target, Appl. Surf. Sci. 511 (2020) 145616. doi:10.1016/j.apsusc.2020.145616.

M. Rausch, S. Mráz, P. Kreiml, M.J. Cordill, J.M. Schneider, J. Winkler, C. Mitterer, Angular resolved mass-energy analysis of species emitted from a dc magnetron sputtered NiW-target, J. Vac. Sci. Technol. A. 38 (2020) 023401. doi:10.1116/1.5138248.

P. Kreiml, M. Rausch, V.L. Terziyska, H. Köstenbauer, J. Winkler, C. Mitterer, M.J. Cordill, Balancing the electro-mechanical and interfacial performance of Mo-based alloy films, Mater. (2020) 100774. doi:10.1016/j.mtla.2020.100774.

P. Kreiml, M. Rausch, V.L. Terziyska, H. Köstenbauer, J. Winkler, C. Mitterer, M.J. Cordill, Improved electro-mechanical reliability of flexible systems with alloyed adhesion layers, Thin Solid Film. (submitted 2020).